COMPARATIVE EVALUATION OF ISAR PROCESSING ALGORITHMS

A THESIS SUBMITTED TO
THE GRADUATE SCHOOL OF NATURAL AND APPLIED SCIENCES
OF
MIDDLE EAST TECHNICAL UNIVERSITY

BY

ALPER TUFAN

IN PARTIAL FULLFILLMENT OF THE REQUIREMENTS
FOR
THE DEGREE OF MASTER OF SCIENCE
IN
ELECTRICAL AND ELECTRONICS ENGINEERING

SEPTEMBER 2012

Approval of the thesis:

COMPARATIVE EVALUATION OF ISAR PROCESSING ALGORITHMS

submitted by **ALPER TUFAN** in partial fulfillment of the requirements for the degree of **Master of Science in Electrical and Electronics Engineering Department, Middle East Technical University** by,

Prof. Dr. Canan Özgen
Dean, Graduate School of **Natural and Applied Sciences** _____

Prof. Dr. İsmet Erkmen
Head of Department, **Electrical and Electronics Engineering** _____

Prof. Dr. Gülbin Dural
Supervisor, **Electrical and Electronics Engineering Dept., METU** _____

Prof. Dr. Seyit Sencer Koç
Co-Supervisor, **Electrical and Electronics Engineering Dept., METU** _____

Examining Committee Members:

Prof. Dr. Yalçın Tanık
Electrical and Electronics Engineering Dept., METU _____

Prof. Dr. Gülbin Dural
Electrical and Electronics Engineering Dept., METU _____

Prof. Dr. S. Sencer Koç
Electrical and Electronics Engineering Dept., METU _____

Assoc. Prof. Dr. Çağatay Candan
Electrical and Electronics Engineering Dept., METU _____

Dr. Ülkü Doyuran
ASELSAN Inc. _____

Date: **10.09.2012**

I hereby declare that all information in this document has been obtained and presented in accordance with academic rules and ethical conduct. I also declare that, as required by these rules and conduct, I have fully cited and referenced all material and results that are not original to this work.

Name, Last name : Alper Tufan

Signature :

ABSTRACT

COMPARATIVE EVALUATION OF ISAR PROCESSING ALGORITHMS

Tufan, Alper

M. Sc., Department of Electrical and Electronics Engineering
Supervisor : Prof. Dr. Gülbin Dural
Co-Supervisor : Prof. Dr. Seyit Sencer Koç

September 2012, 123 pages

In this thesis, Inverse Synthtetic Aperture Radar image reconstruction techniques, named as Range Doppler, Back Projection, Polar Formatting, Multiple Signal Classification (MUSIC) and Time Frequency techniques are analysed and compared using simulations. Time Frequency techniques investigated in this thesis are Short Time Fourier Transform, Wigner-Ville Distribution, Smoothed Wigner-Ville Distribution and Choi-Williams Distribution.

First, some fundamental concepts of ISAR, such as resolution, range profile, time dependent Doppler frequency are given. A data simulator is designed and implemented for the purpose of providing configurable input to ISAR signal processing algorithms for a given ISAR target geometry. Estimation of target rotational velocity is explained with the help of three methods, namely Grid Search, WVD Slope and Radon Wigner-Hough Transform. Then, theoretical background of image formation algorithms is discussed. MATLAB simulations for each algorithm are implemented with several configurations in order to visualize and analyse the

results. Finally, processing algorithms are compared to discuss the advantages and disadvantages.

Keywords: ISAR, Inverse Synthetic Aperture Radar, Image Reconstruction, Imaging.

ÖZ

ISAR İŞLEME ALGORİTMALARININ KARŞILAŞTIRMALI DEĞERLENDİRİLMESİ

Tufan, Alper

Yüksek Lisans, Elektrik Elektronik Mühendisligi Bölümü
Tez Yöneticisi : Prof. Dr. Gülbin Dural
Ortak Tez Yöneticisi : Prof. Dr. Seyit Sencer Koç

Eylül 2012, 123 sayfa

Bu tez kapsamında, Ters Yapay Açıklıklı Radar (ISAR) görüntü elde etme tekniklerinden Menzil-Doppler, Geri İzdüşüm, Polar Biçimlendirme, Çoklu Sinyal Sınıflandırma (MUSIC) ve Zaman Frekans teknikleri analiz edilmiş ve simulasyonlar kullanılarak karşılaştırılmıştır. Tez kapsamında araştırılan Zaman Frekans teknikleri Kısa Zaman Aralıklı Fourier Dönüşümü, Wigner-Ville Dağılımı, Düzleştirilmiş Wigner-Ville Dağılımı ve Choi-William Dağılımı'dır.

Öncelikle, çözünürlük, menzil profili, zamana bağlı Doppler frekansı gibi temel ISAR kavramları verilmiştir. Verilen bir hedef geometrisi için ISAR sinyal işleme algoritmalarına ayarlanabilir giriş verisi sağlamak amacıyla bir veri simulatörü tasarlanmış ve uygulanmıştır. Izgara Arama, WVD Eğim ve Radon Wigner-Hough Dönüşümü yaklaşımları yardımıyla hedefin dönel hız kestirimi konusu açıklanmıştır. Daha sonra ISAR görüntü oluşturma algoritmalarının teorik altyapısı tartışılmıştır. Sonuçları görselleştirmek ve analiz etmek amacıyla her algoritma farklı konfigurasyonlarla MATLAB ortamında uygulanmıştır. Son olarak işleme

algoritmalarının avantajları ve dezavantajlarını tartışmak amacıyla karşılaştırma yapılmıştır.

Anahtar Kelimeler: Ters Yapay Açıklıklı Radar, Görüntü Oluşturma, Görüntüleme.

to

My parents and sister

and

Burcu

ACKNOWLEDGEMENTS

I would like to express my deepest gratitude to my supervisor Prof. Dr. Gülbin Dural and my co-supervisor Prof. Dr. Sencer Koç for their encouragements, guidance, advice, criticism and insight throughout the research.

I would like to thank ASELSAN Inc. for facilities provided for the competition of this thesis.

I would like to forward my appreciation to all my friends and colleagues who contributed to my thesis with their continuous encouragement.

I would also like to convey thanks to jury members for their valuable comments on this thesis.

Last, but mostly, I would like to express my endless gratitude to my parents, Ayhan and Ünzile Tufan and my sister, Ayça Tufan for their love, continuous support and encouragements throughout all my life. Also I have to send my special thanks to my lovely wife, Burcu Tufan who made me smile with her existence. I would not have been able to complete this work without her support and endless love. This thesis is dedicated to my great family that means everything to me.

TABLE OF CONTENTS

LIST OF TABLES

TABLES

LIST OF FIGURES

FIGURES

LIST OF ABBREVIATIONS

AR	: Auto Regressive
BP	: Back Projection
CWD	: Choi-Williams Distribution
DFT	: Discrete Fourier Transform
FFT	: Fast Fourier Transform
ISAR	: Inverse Synthetic Aperture Radar
SAR	: Synthetic Aperture Radar
JTFA	: Joint Time-Frequency Algorithm
LFM	: Linear Frequency Modulation
LOS	: Line Of Sigth
MUSIC	: Multiple Signal Classification
PR	: Polar Reformatting
PRI	: Pulse Repetition Interval
STFT	: Short Time Fourier Transform
RD	: Range-Doppler
SFW	: Stepped-Frequency Waveform
SNR	: Signal-to-Noise Ratio
SWVD	: Smoothed Wigner-Ville Distribution
WHT	: Wigner-Hough Transform
WVD	: Wigner-Ville Distribution

CHAPTER 1

INTRODUCTION

1.1 Radar Target Imaging

Radar is an acronym based on the phrase “radio detection and ranging”. Radar is a strong technology that provides all-weather, day/night capability to detect and locate the targets. In addition, it is possible to make a visual representation of an area or target by properly illuminating it with radar waves. Radar can work in all weather conditions since electromagnetic waves propogate through clouds and rain with only a limited attenuation. Radars are used for various applications such as imaging, guidance, global positioning and remote sensing.

A radar system consists of a transmitter, a receiver, an antenna, a signal processing unit and display unit. Radar transmits consecutive pulses or bursts regularly spaced in time and illuminate the area within the antenna beam [1]. Scattered signals from the target scatterers are received to extract the desired information about it.

One of the most important radar applications is imaging. Radar receives scattered waves from a target as the summation of returned signals from the scatterers of that target. Since the integration of scatterer returns can be measured by the radar, distribution of reflectivity belonging to the target can be reconstructed by processing the received data [2]. The distribution of reflectivities directly gives the radar image of the target. Generally radar images are mapped onto range and cross-range planes. Range is the dimension along the radar’s line of sight and cross-range is the dimension which is orthogonal to the line of sight direction.

The image qualities of radar applications are related to the minimum distance which can be resolved between two scatterers. This minimum distance is called image resolution. Range resolution of the radar depends on the transmitted bandwidth, while cross-range resolution increases with larger antenna aperture. In most applications instead of using a physically large antenna, a synthetic aperture is formed with the help of target or radar motion. In this case, cross-range resolution increases with longer observation time on target. Synthetic array radar processing coherently integrates signals taken from sequences of small apertures to emulate the outputs from a large aperture [2].

By simply changing the reference system one can look at synthetic aperture concept from Synthetic Aperture Radar (SAR) or Inverse Synthetic Aperture Radar (ISAR) point of view [3]. If radar is moving and the target is stationary the scenario is called a SAR system. The scenario that radar is stationary and target is moving refers to the ISAR system.

ISAR is an effective system which acquires high resolution images of targets such as aircrafts and ships. ISAR technology utilizes the movement of the target rather than the emitter to form the synthetic aperture. For ISAR, synthetic aperture is formed by coherently combining the target returns from small aspect angles while target is rotating. ISAR images are produced by using the rotation of targets and processing the resultant Doppler variations in slow time signal. Differential Doppler shift of adjacent scatterers can be used to measure distribution of target reflectivity [2]. Generally, most important and challenging issue in ISAR processing is time dependent Doppler frequency contents of received signal. ISAR target imaging methods aims to retrieve the time varying Doppler information of scatterers in the target.

1.2 Developments in ISAR Imaging

In the literature ISAR image reconstruction algorithm deal with so many difficulties. Rotational rate estimation, motion compensation and 2D-image reconstruction are the most challenging issues of ISAR signal processing.

Because of the complicated motions of the targets reconstructed 2D-ISAR images may be blurred. Source of the blurring may be translational or rotational motions of the targets. ISAR systems should deal with these two types of motion compensation. In the literature translational motion compensation techniques can be found in [4] and [5]. In this thesis, translational compensation is assumed to be done previously.

Two dimensional Fast Fourier Transform (2D-FFT) technique is a well-known technique and works in the small angle approximation which will be explained in CHAPTER 5. All alternatives of ISAR signal processing try to improve the limited resolution of 2D-FFT.

Some modern spectral estimation algorithms such as 2D-Multiple Signal Classification (2D-MUSIC), 2D-Capon, Auto Regressive (AR) methods have been proposed in [6], [7], [8] to achieve superresolution. These algorithms require the stationarity of the received signal, i.e., the range cell migration and the quadratic higher terms in the phase definition can be ignored. Spectral estimation methods increase the resolution for short observation angles. But in this case maximum acceptable rotation rate is limited. More details about the advantages and disadvantages of using spectral estimation based algorithms can be found in the papers mentioned above.

Rotational motion of targets causes range cell migration and creates a time varying Doppler frequency shift. There are many algorithms in the literature in order to eliminate range cell migration and estimate time varying frequency behaviors. Polar reformatting algorithm in [1] deals with range cell migration and compensates the rotational motion of target with the assumption of known target rotation rate. Also

back-projection algorithm in [3] can be adapted for the ISAR image processing with the same assumption.

In real applications estimation of target rotation parameters is another important topic for ISAR imaging. ISAR cross-range signal model can be modeled as superposition of linear chirp-signals with unknown parameters related to rotational motion. [9] and [10] proposes dominant scatterer algorithms for the estimation of target rotational velocity. Investigating chirp signal parameter estimation procedures in [11], [12] and [13] can be useful for the estimation of unknown parameters of cross-range response.

Applications of time-frequency analysis for ISAR imaging have become very popular in recent years. In [2] and [14], the time-frequency transforms are discussed in detail. It is possible to apply these techniques to cross-range signals of ISAR targets. Time-frequency based image formation doesn't use any assumption and gives history of target images at different time samples. Time resolution problem for Short Time Frequency Transform (STFT) and cross-term problem of Wigner-Ville Distribution (WVD) are the main issues of time-frequency algorithms. Combining smoothing methods with WVD creates new algorithms to remove the cross-terms [15].

Beside these methods some parametric time-frequency methods are also considered in [16] and [17] where the ISAR cross-range signal is adaptively decomposed and written as the summation of some basis functions. So that time-frequency characteristics of ISAR signal can be obtained accurately.

In addition, an algorithm which is called Matching Pursuit is proposed in [18]. The ISAR echo is decomposed into many subsignals that are generated by discretizing spatial domain and synthesizing the ISAR data for every discretized spatial position. The coefficients of subsignals that contribute the ISAR signal are obtained to get very high resolution images.

1.3 Motivation

ISAR is a target identification system which uses target returns for the purpose of image formation. Although there are many algorithms developed for ISAR processing, improvements on the ISAR imaging methods are still going on. Generally, ISAR algorithms in the literature can not handle all the difficulties of real applications. Most of the algorithms have a disadvantage or are based on some assumptions beside its advantages. It is not so easy to decide which algorithm will be choosen for real applications. Then we need to analyse difficulties of target identification and talk about the possible application areas of ISAR processing algorithms. Discussing the advantages, disadvantages of ISAR algorithms individually and comparing their performances would be useful. Implementations of many ISAR image reconstruction techniques will help us to see the differences between the alternative ways. The main purpose of this thesis is to investigate different ISAR image reconstruction techniques and compare them in terms of their performances. Performances of several ISAR algorithms will be examined utilizing the simulated data with different configurations.

1.4 Scope of the Thesis

CHAPTER 1 is an introduction to radar target imaging. It gives a brief information about synthetic aperture radar concept and explains how to form synthetic apertures to increase the cross-range resolutions in Section 1.1. In Section 1.2, a literature survey about ISAR processing algorithms is given and different problems of ISAR signal processing are discussed. Recent developments of ISAR imaging techniques are also summarized.

CHAPTER 1 also discusses the motivation of the thesis and the benefits of investigations about the ISAR in Section 1.3.

CHAPTER 2 provides of fundamental terminology for ISAR imaging and gives the theoretical background. These fundamental concepts are required to understand the

following chapters. In this chapter, ISAR geometry is also shown in order to make a visual representation. Basic properties of radar such as resolution and Doppler frequency are combined with the ISAR theory. Range profile, time history, straddle loss are some other subjects which will be talken about.

CHAPTER 3 is about generating simulator input data for the implementation of algorithms discussed in Chapters 4 and 5. It also classsifies transmitted waveforms as stepped frequency and linear frequency modulation (LFM). ISAR data simulator can generate both of these types of waveforms which will also be explained in this chapter.

CHAPTER 4 deals with the estimation of unknown rotational velocity of targets. Received cross-range signal is modeled as summation of linear chirps and examples of chirp parameter estimation methods are given to solve this problem. Since the main topic of this thesis is the evaluation of different image reconstruction algorithms, this subject is not discussed in detail. Three different techniques to solve this problem are explained. Additionally, some simulations about these rotational rate estimation techniques are given in this chapter.

CHAPTER 5 is the main chapter that gives all details about the ISAR signal processing algorithms. Theories of Range-Doppler, Filtered-Back Projection, Polar Reformatting (PR) and 2D-MUSIC (alternative to 2D-FFT) algorithms are given here. These algorithms are simulated to analyze the results of applications. In the simulations of these algorithms it is assumed that rotational velocity of the target is known. PR and Back Projection (BP) algorithms are based on removing blurring effects due to the rotational motion and try to increase cross-range resolution. 2D-MUSIC algorithm can be thought as an alternative to conventional 2D-FFT to get the final image. This algorithm works on the interpolated rectangular data like 2D-FFT. Time-frequency techniques STFT, WVD, Smoothed Wigner-Ville Distribution (SWVD) and Choi-Williams Distribution (CWD) are investigated in the following parts and simulated to visualize the theory. In contrast to first algorithm family, these methods do not need apriori information on the rotational

velocity. In this chapter advantages and disadvantages of all algorithms are discussed. Also a comparison based on resolution, SNR and computational load is done.

CHAPTER 6 is the conclusion part which also includes a discussion on the possible future works.

CHAPTER 2

FUNDAMENTALS OF ISAR

In this chapter, fundamental concepts of ISAR are presented. ISAR target geometry and received signal model is constructed. Basic ISAR terms such as range-cross range resolution, Doppler frequency, range profile, time history and straddle loss are explained.

2.1 ISAR Geometry and Signal Modelling

Basic ISAR imaging geometry is given in Figure 2-1.The target is composed of point scatterers and ISAR received signal is a superposition of each return from the individual scatterers.

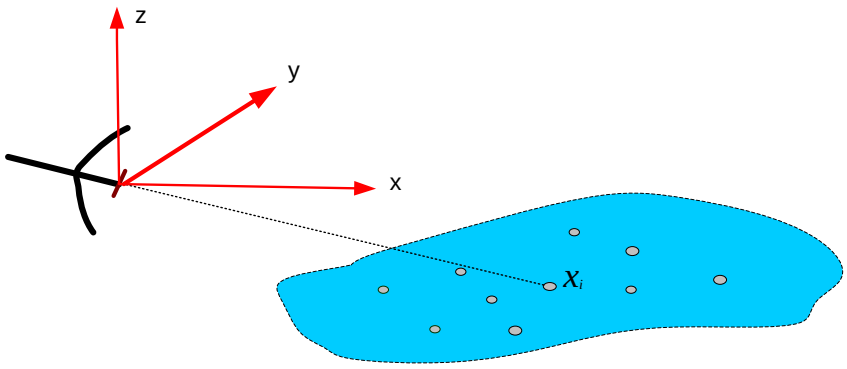

Figure 2-1: ISAR Geometry

Target return from k^{th} pulse can be written as

$$s_R(t,k) = \sum_{i=1}^{M} a_i s(t - kT - \tau_i) \tag{2.1}$$

where M is number of point scatterers, a_i is the complex amplitude and τ_i is the time delay corresponding to range of that scatterer. General expression of time delay is

$$\tau_i = \frac{2R(t,x_i)}{c} \tag{2.2}$$

where R is range, x_i is i^{th} scatterer and c is the velocity of light. Taking the Fourier transform of time domain signal, frequency behaviour of target return can be obtained as

$$S(f,k) = S(f) \sum_{i=1}^{M} a_i e^{-j2\pi(kfT + \frac{2R(t,x_i)}{c})} \tag{2.3}$$

Phase component corresponding to the range of scatterers is the most important parameter for ISAR image reconstruction. Target motion indicates the range formulation of the ISAR system.

The inverse synthetic aperture is achieved when there is a variation of target-radar aspect angle [3]. ISAR system geometry includes a fixed or moving radar and a target which has a combination of rotational and translational motions, as shown in Figure 2-2.

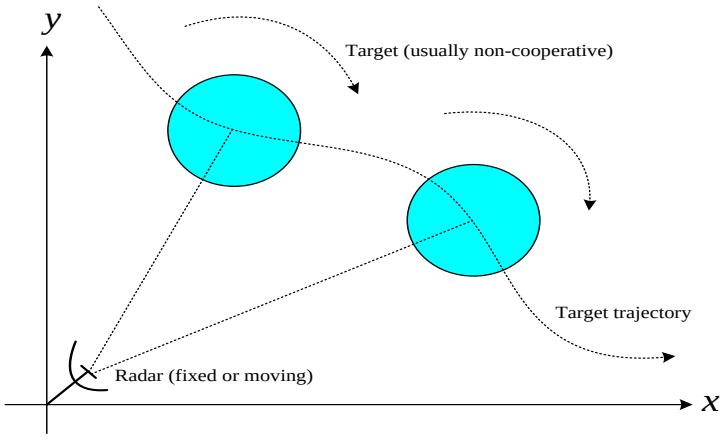

Figure 2-2: An Example of Target with Rotational and Translational Motion

The range of scatterer can be approximated with the projection of range vector onto the line of sight vector of that scatterer, when the distance from radar is much larger than the distance from any scatterer location to the center of object. Figure 2-3 visualizes the far field range approximation of target scatterer.

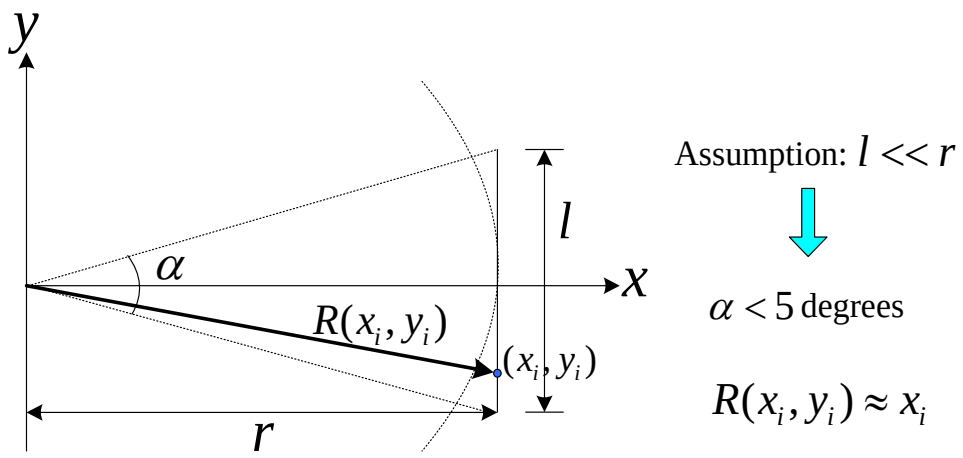

Figure 2-3: Range Approximation of Point Scatterer in Far Field

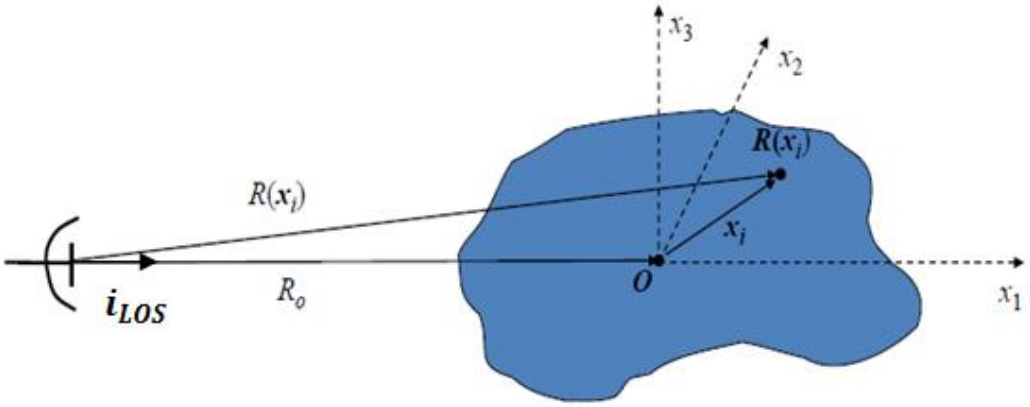

Figure 2-4: Vector Representation of ISAR Geometry

Assuming that at initial time $t = t_0$ distance between radar and the center of target is R_0, range of a simple scatterer can be represented as follows:

$$R(x_i, y_i) \cong R_0 + x_i . i_{LOS} \tag{2.4}$$

where i_{LOS} is the unit line of sight vector between radar and the center of target as shown in Figure 2-4. Then the received signal from target can be written as

$$S_R(f,k) = S(f) e^{-j2\pi(kfT + \frac{2R_0}{c})} \sum_{i=1}^{M} a_i e^{-j\frac{4\pi}{c}(x_i . i_{LOS})} \tag{2.5}$$

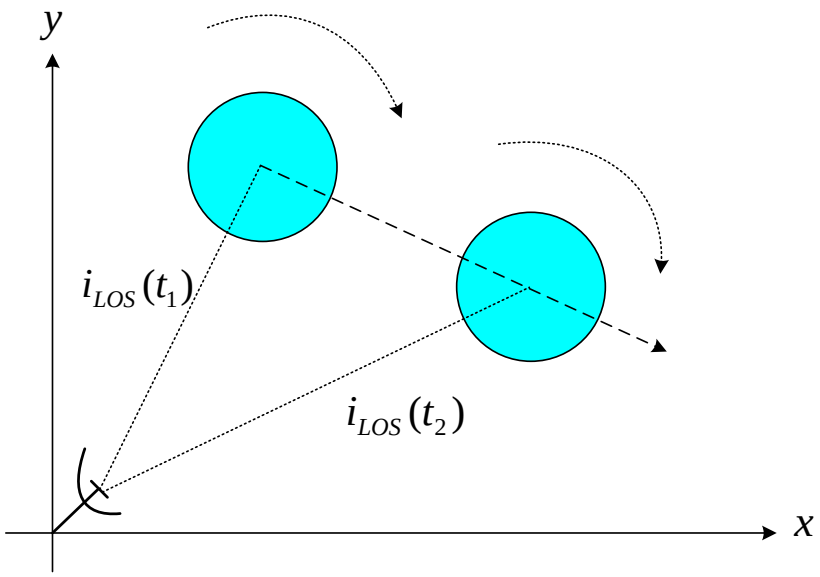

Figure 2-5: Time Dependent Line of Sight Vector

Figure 2-5 shows that while the target is moving along a given trajectory, the aspect angle changes. Therefore the i_{LOS} changes as well [3]. During the motion of the target this vector becomes a function of time. This is the dynamic target model and received signal is written as

$$S_R(f,k) = S(f) e^{-j2\pi(kfT + \frac{2R_0(kT)}{c})} \sum_{i=1}^{M} a_i e^{-j\frac{4\pi}{c}(x_i . i_{LOS}(kT))} \tag{2.6}$$

To find the range of target, rotation of the plane should be considered. In Figure 2-6, x-plane is reference system embedded on the target and y-plane rotates along the LOS. Also, $\Omega(kT)$ is rotation vector and $\theta(kT)$ is rotated angle at k^{th} pulse.

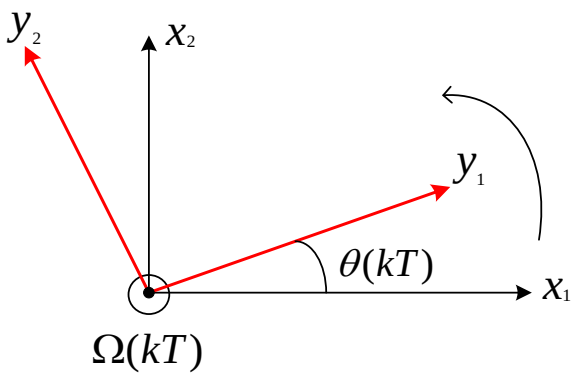

Figure 2-6: Coordinate Transformation of Rotated Target

Target image plane consists of range and cross-range dimensions. When the aspect angle of target changes, coordinate transformation should be done to find new $i_{LOS}(t)$ corresponding to that time instant.

Coordinate transformation equation can be expressed as:

$$\begin{bmatrix} y_1 \\ y_2 \end{bmatrix} = \begin{bmatrix} \cos\theta(t) & -sin\theta(t) \\ sin\theta(t) & \cos\theta(t) \end{bmatrix} \begin{bmatrix} x_1 \\ x_2 \end{bmatrix} \tag{2.7}$$

$i_{LOS}(t)$ is equivalent to the coordinate (0,1). Therefore obtained line of sight vector representation becomes [3] :

$$i_{LOS}(t) = \begin{bmatrix} sin\theta(t) \\ \cos\theta(t) \end{bmatrix} \tag{2.8}$$

When the object has both translational and rotational motion, range of one scatterer can be expressed as

$$R(t) = R_0 + v_R t + x_0 \sin(\Omega t) + y_0 \cos(\Omega t) \tag{2.9}$$

2.2 Time Dependent Doppler Frequency Shift

To find the instantenaous frequency of a signal, time-derivative of phase is taken. Then the Doppler frequency shift which target motion creates is calculated as follows

$$\Phi_r\,(R_t) = \ 2\pi f\,\frac{2R(t)}{c} = 2\pi f\,\frac{2(R_0 + v_R t + \ x_0\sin(\Omega t) + y_0\cos(\Omega t))}{c} \quad (2.10)$$

$$f_D = \frac{1}{2\pi}\frac{d}{dt}\,R(t) = \frac{2f}{c}\,v_R + \frac{2f}{c}(x_0\Omega - y_0\Omega^2 t) = \ f_{D_{trans}} + f_{D_{rot}} \quad (2.11)$$

where $\Phi_r\,(R_t)$ is phase, f_D is Doppler frequency and Ω is rotational velocity of the scatterer. Doppler frequency shift is the sum of translational motion Doppler and rotational motion Doppler. In the applications only rotational motion will be emphasized. Rotational Doppler frequency has linear and quadratic parts. ISAR algorithms consider time varying Doppler frequency information to resolve the scatterers. Equation (2.11) shows that rotational Doppler frequency is directly related to the geometric location of scatterer in the object plane.

2.3 Slant Range Resolution

Range resolution (Δr_s) is expressed as

$$\Delta r_s = \frac{c}{2\beta} \quad (2.12)$$

Where β is the bandwidth of the signal waveform. High resolution radars need large bandwidth. Both LFM and stepped frequency waveforms use this expression. For the stepped frequency waveform equation can be expressed as

$$\Delta r_s = \frac{c}{2N\Delta f} \quad (2.13)$$

Where Δf is the increasing frequency step of succesive pulses and N is the number of pulses in each burst.

2.4 Cross Range Resolution

Basically, Doppler frequency shift (f_D) produced by a small angle rotation is [19]

$$f_D = \frac{2}{c}\omega r_c f \tag{2.14}$$

Where *f* is the carrier frequency, ω is the angular rotation rate and r_c is cross range of the scatterer. If the Doppler frequency is assumed to be constant during the integration time (PRI), it is possible to calculate the rotational Doppler frequency change and derive cross-range resolution expression.

If two scatterers are seperated only in cross-range, the scatterer which has larger radius gives a larger Doppler frequency shift. Source of the Doppler difference for two scatterers is radial velocity, which is expressed as

$$V = wr_c \tag{2.15}$$

Doppler frequency change is generally written as

$$\Delta f_D = \frac{2\Delta V}{\lambda} = \frac{2\, w\Delta r_c}{\lambda} \tag{2.16}$$

Doppler resolution is directly related to the coherent integration time ($NPRI$)

$$\Delta f_D = \frac{1}{NPRI} \tag{2.17}$$

If we equate both equations cross-range resolution can be obtained as

$$\Delta r_c = \lambda \frac{\Delta f_D}{2} w = \frac{\lambda}{2wNT} = \frac{\lambda}{2\Delta\theta} \tag{2.18}$$

ISAR cross-range resolution is directly related to the azimuth integration angle. High PRI can be used to increase the cross-range resolution. But there will be some disadvantages of increasing PRI, as a trade off, which will be seen in the following sections.

2.5 Range Profile-Time History

Range profile seperates the slant-range peaks of the target. In other words, it is the projection of returning signal onto the line of sight dimension. The scatterers that are in the same range cell but in different cross-range cells can not be seen from the range profiles. A visual representation of range profiles is given in Figure 2-7.

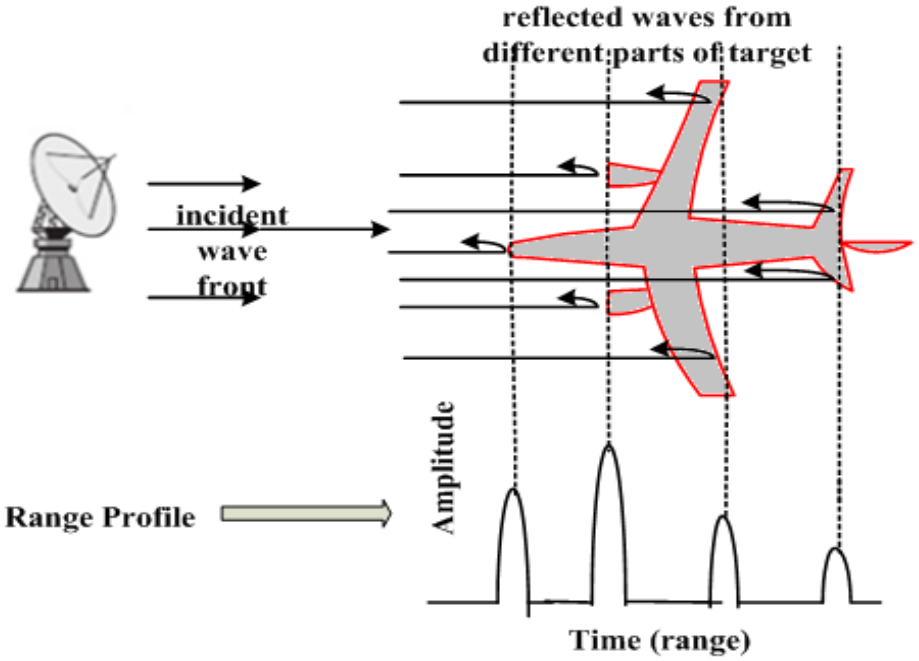

Figure 2-7: Range Profiles of Target

Linear FM radar collects N range profiles for N transmitted pulses. Since stepped frequency radar collects data in the frequency domain, inverse FFT of rows represents range profiles. Series of range profiles is the input matrix of ISAR. Phase of each range cell in this matrix differs from one burst to another. Discrete time samples which are taken during coherent pulse interval are called time history of range cells. Range profiles that have time history make possible to resolve both range and cross range of scatterers leading to ISAR image reconstruction.

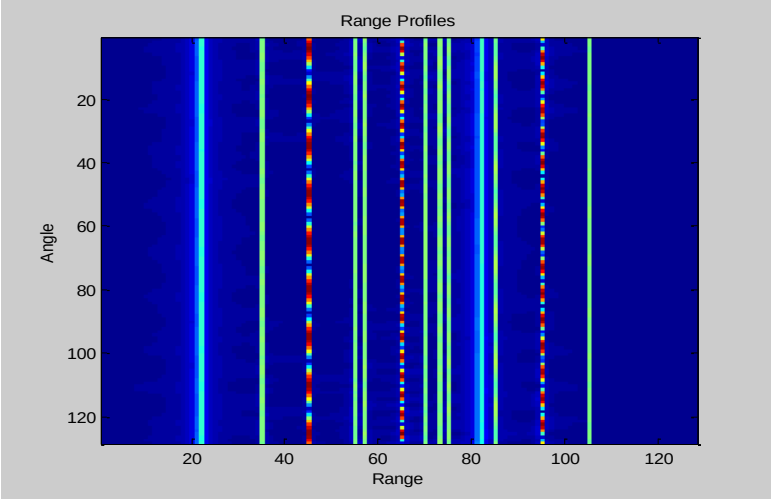

Figure 2-8: Range Profile Generation Example

An example of range profile generation is shown in Figure 2-8. IFFT in one dimension gives the range profiles of target for all angle samples. All columns of this figure can be thougth as time histories of different range cells.

2.6 Straddle Loss

In ISAR analysis it is a fact that taking FFT of the signal may result in frequency estimation errors. In other words, if the frequency changes can not exactly be discretized in the FFT domain cross-range value can not be recovered perfectly. FFT is a sampled version of the discrete time Fourier transform. The exact location of the peak values may be found only if Doppler frequency coincides exactly with one the discrete FFT frequencies [21]. Otherwise peak amplitudes of target returns may be reduced and this may cause ISAR images to be blurred. This type of FFT amplitude loss is called straddle loss.

To overcome straddle loss, an interpolation technique can be used to estimate the exact value of Doppler. To analyse the straddle loss frequency resolution can be adjusted to increase or decrease. Straddle loss in both FFT dimensions can be observed in Figure 2-9 and Figure 2-10.

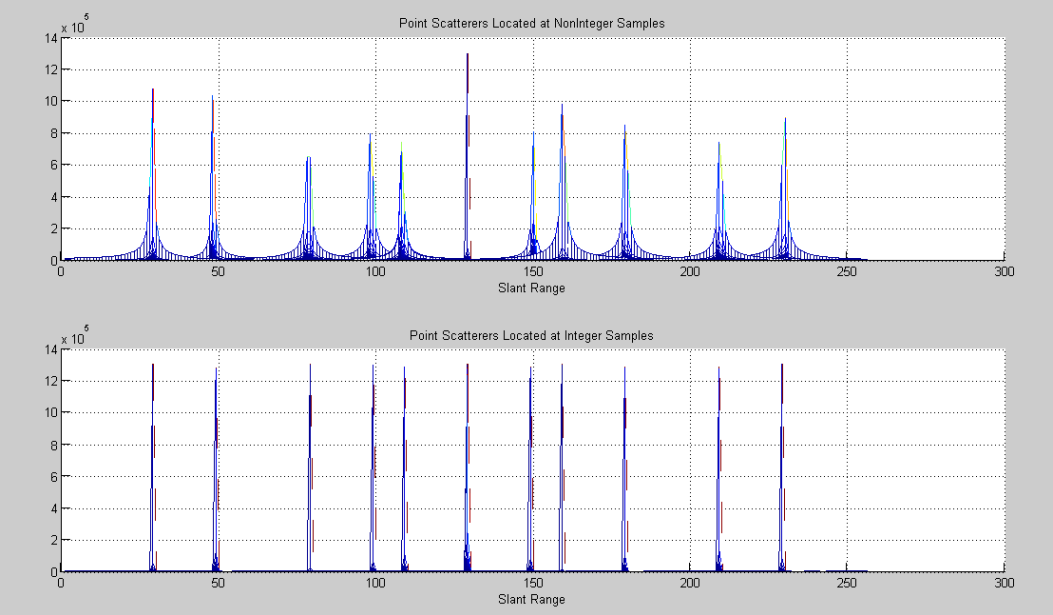

Figure 2-9: Straddle Loss Due on Range Profiles

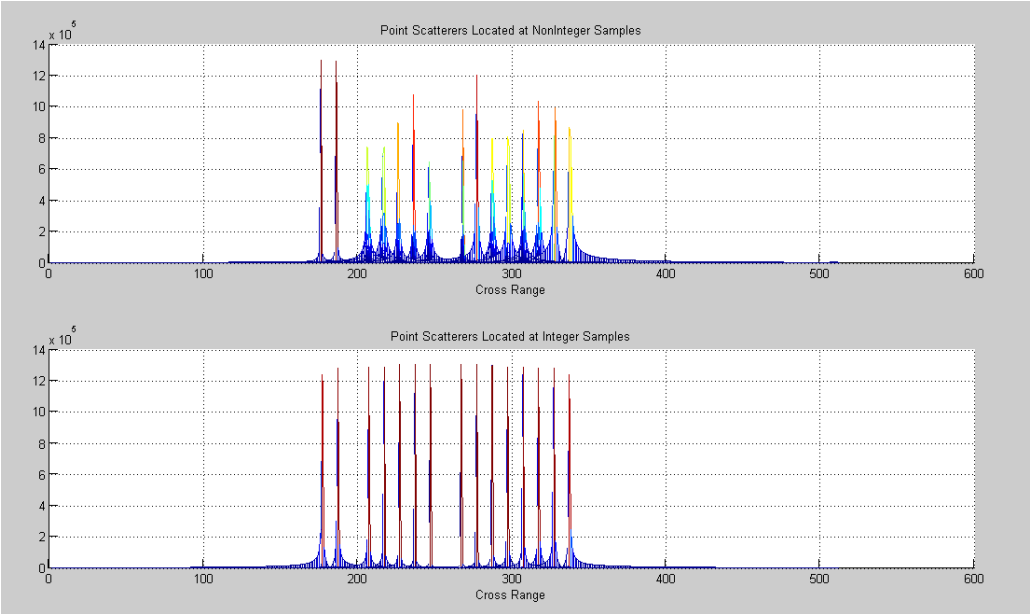

Figure 2-10: Straddle Loss on Cross Range Profiles

As it is seen from Figure 2-9 and Figure 2-10, the equal amplitudes of scatterers can vary in the reconstructed ISAR image if they locate at noninteger frequency samples.

CHAPTER 3

ISAR DATA SIMULATOR DESIGN

As a part of the thesis work, a simulator is designed for the purpose of generating input data. Running this simulator with different input parameters, it is possible to analyse ISAR image formation algorithms. All algorithms in this thesis process the data generated by this simulator. In this section the input data simulator is described by using theoretical background of radar waveforms.

ISAR simulator has two alternative radar waveforms which are stepped frequency waveform and linear FM (chirp) signal. Transmitted radar pulses are returned by a different time delay for each scatterer and received returns are sampled in time domain. When the stepped frequency modulated pulses are used it is easy to represent the received signal samples in frequency domain. Both modulation types increase the range resolution by using large bandwidth.

Locations and the reflectivities of the scatterers are the inputs of ISAR data. 2D matrix is created from the target returns $(M \times N)$. Dimensions of the matrix become slant-cross range of the scatterers at the end of image reconstruction.

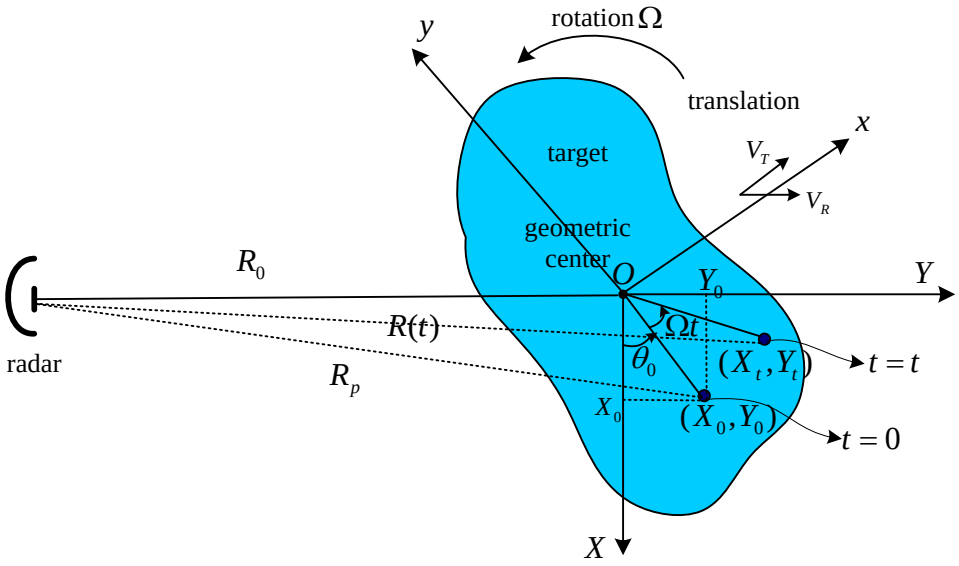

Figure 3-1: General ISAR Geometry [20]

General ISAR geometry is given in Figure 3-1. The distance between the radar and the target needs to be calculated when the target is rotated. ISAR simulator calculates the range of each target and gives a phase shift corresponding to time delay of target return. ISAR data uses the complex envelope of signal, which means ISAR simulator data becomes suitable for the baseband operation. Complex envelope of the received signal can be written as

$$s_R(t) = p(x_0, y_0)e^{j2\pi f 2R(t)/c} = p(x_0, y_0)e^{j\Phi(\mathrm{R_t})} \tag{3.1}$$

where $p(x_0, y_0)$ is the reflectivity of a point target. $R(t)$, which is the range of target can be expressed by

$$R(t) = R_p + x_0 \sin(\Omega t) + y_0 \cos(\Omega t) \tag{3.2}$$

Then the total returned signal can be represented as the summation of the individual scatterers in the main target

$$s_T(t) = \sum_{k=1}^{K} \left(p(x_k, y_k) e^{j2\pi f 2R_k(t)/c} \right) \tag{3.3}$$

where *K* is the number of point scatterers.

3.1 Linear FM Waveform

To increase the resolution of simple pulse time duration (τ) should be decreased. On the other hand detection performance of the radar depends on the pulse energy. Pulse energy is directly related to the time duration of the pulse. If the resolution of a simple pulse is improved then the detection performance is degraded.

LFM waveform gives a chance to increase resolution without affecting the detection performance. It is a pulse compression waveform and has a bandwidth such that $\beta \gg 1/\tau$.

This type of waveform has a time-bandwidth product which is greater than one.

LFM waveform is expressed by the below equation.

$$x(t) = e^{j\pi\beta t^2/\tau} \tag{3.4}$$

This equation sweeps the bandwidth of the signal linearly. Instantaneous frequency of LFM signal is related with the derivative of the phase term [21].

$$F_i(t) = \frac{1}{2\pi} \frac{d\theta(t)}{dt} = \frac{\beta}{\tau} t \tag{3.5}$$

If the LFM signals are transmitted, the received signal is match-filtered with the reference signal $x(t)$ to extract the range information of target scatterers. As the BT (time-bandwidth product) increases frequency spectrum of the reference signal has a more rectangular shape. It means that match filtering operation with the reference signal gives an output whose energy is more concantrated in a main lobe of $1/\beta$ time duration.

Matched filter output frequency response is the product of two rectangle shape which is also a rectangle ($|X(f)|^2$), where $X(f)$ is the frequency spectrum of the

transmitted LFM waveform with a Rayleigh resolution of $1/\beta$ [21]. Time and frequency behaviours of LFM signal can be observed in Figure 3-2.

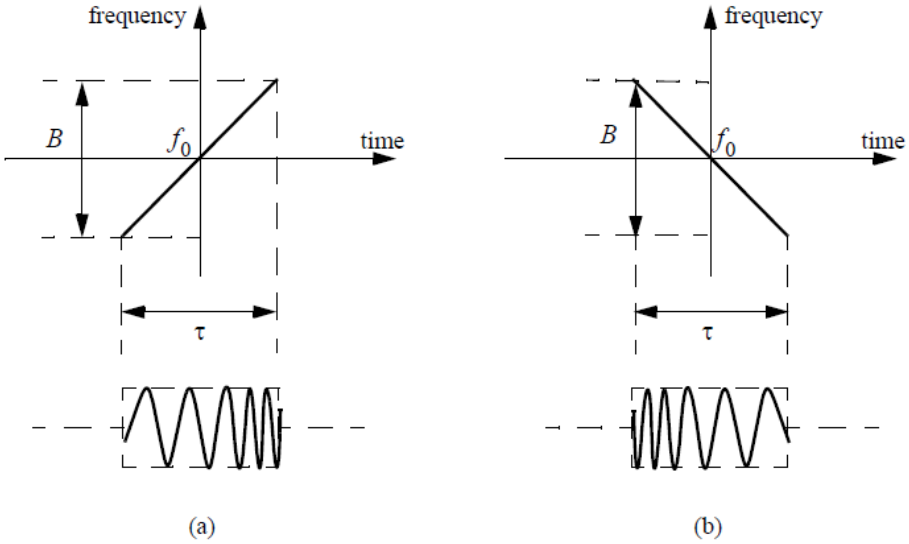

Figure 3-2: Frequency Sweeping of Linear FM Waveform

3.2 Generation of LFM Data

LFM data generator uses a sampling gate around the main target. The *k*th scatterer has a pulse return with a time delay of $2R_{km}$/c for the pulse number $m = 1 \ldots M$. Sum of these signal returns is sampled on baseband. There are two terms of simulated data:

Term 1: Complex envelope of each return has a phase shift which is a function of distance between the scatterer and the radar ($e^{j2\pi f_0 2R_{km}/c}$).

Term 2: Transmitted frequency modulated signal is received in the same manner with a shifted version only ($e^{j\pi\beta(t-2R_{km}/c)^2/\tau}$) where $|t - 2R_{km}/c| < \tau/2$ and zero elsewhere.

($t = nT_s$) for $n = 1 \ldots N$ are the discrete sampling times.

Received baseband signal is simulated as the multiplication of these two terms for each scatterer. Index *m* is the row number of the data matrix and represents the pulse number. Index *n* is the column number and represents sampling times of received signal. Total matrix is the summation of all scatterer returns.

As a result final simulator data can be expressed as

$$s(m,n) = \sum_{k=1}^{K} s_k(m,n) \tag{3.6}$$

$$s_k(m,n) = \begin{cases} e^{j2\pi f_0 2R_{km}/c} e^{j\pi\beta(nT_s - 2R_{km}/c)^2/\tau}, & |nT_s - 2R_{km}/c| < \tau/2 \\ 0 & , |nT_s - 2R_{km}/c| > \tau/2 \end{cases} \tag{3.7}$$

3.3 Stepped Frequency Waveform

Stepped frequency waveform can be used for high range resolution radar applications. This type of radars covers a wide bandwidth by transmitting frequency-stepped pulses. A schematic diagram of stepped frequency radar system is presented in Figure 3-3. As it is seen from the figure, since stepped-frequency radar needs only an instantenous receiver bandwidth it reduces the system complexity [22].

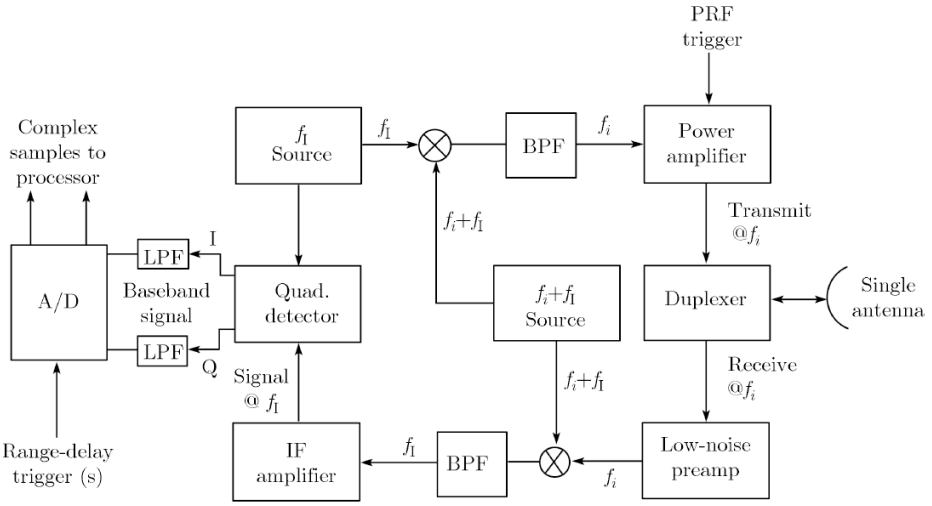

Figure 3-3: Schematic Representation of Stepped-Frequency Radar System [22]

SF data generator uses stepped-frequency waveforms to obtain target's reflectivity sampled in the frequency domain [19]. This simulator generates N stepped-frequency bursts. Each burst includes n pulses and each succesive pulse has a frequency difference of a constant step. Suppose the radar is stationary, and an stationary target is located at a range corresponding to a delay $t_l + \delta t$, where δt represents an incremental delay around the nominal t_l. Individual pulses are processed through the simple pulse matced filter as before, producting the output waveforms

$$y_m(t) = s_p{}^*[t - (t_l + \delta t) - mT]e^{j2\pi m\Delta F[t-(t_l+\delta t)-mT]} \tag{3.8}$$

This output is then sampled at t = $(t_l + mT)$ (that is, t_l seconds after the current pulse was transmitted), corresponding to range $R_l = \frac{ct_l}{2}$. The resulting sample becomes the l^{th} range bin sample for the current pulse [21]

$$y[l,m] = y_m(t_l + mT) = s_p{}^*(-\delta t)\, e^{-j2\pi m\Delta F\delta t} \tag{3.9}$$

From Equation (3.9) it can be seen that slow time sequence for a fixed range bin, when using a linearly stepped frequency waveform, is a discrete time sinusoid [21].

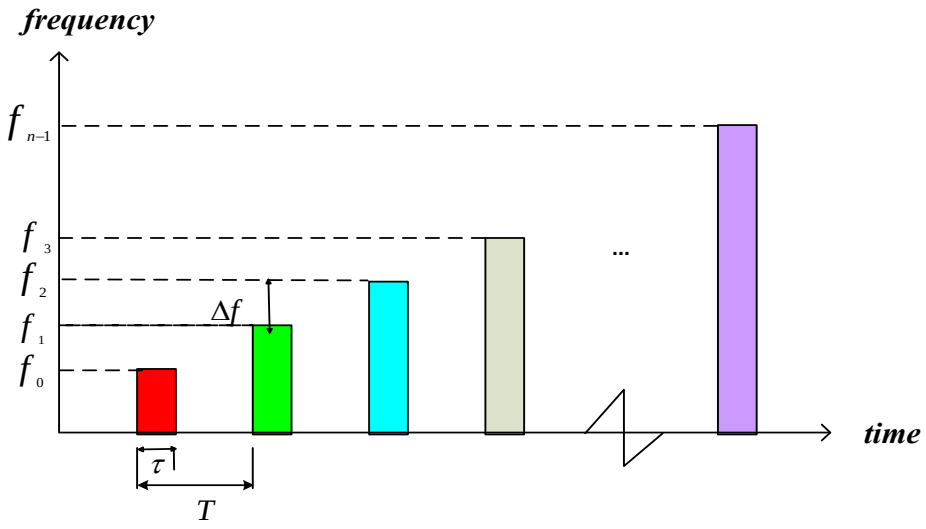

Figure 3-4: Stepped Frequency Waveform

Lets consider an example of stepped-frequency waveform with the pulse repetition interval T, a pulse duration τ, a starting point of frequencies f_0, frequency step Δf and number of pulses in a single burst N as shown in Figure 3-4. Then the reference transmitted signal can be written as [22]

$$x(t) = \sum_{i=0}^{N-1} rect(\frac{t - iT - \tau/2}{\tau}) e^{-j2\pi(f_0 + i\Delta f)t} \tag{3.10}$$

which is the expression of superposition of N consecutive stepped-frequency pulses. When the signal is stationary received signal formulation can be constructed after multiplication and low pass filtering operations (quadrature detector output).

$$y(t) = \sum_{i=0}^{N-1} rect(\frac{t - iT - \frac{\tau}{2} - \frac{2R_0}{c}}{\tau}) e^{-j2\pi(f_0 + i\Delta f)\frac{2R_0}{c}} \tag{3.11}$$

The well-known signal processing technique to find the range profiles of stepped-frequency waveform is Discrete Fourier Transform (DFT) processing. Quadrature detector output which is sampled and transformed using DFT can be expressed as

$$Y(k) = \sum_{i=0}^{N-1} e^{-j2\pi(f_0 + i\Delta f)\frac{2R_0}{c}} e^{-j\frac{2\pi ik}{N}} \tag{3.12}$$

The samples from one range cell can be defined as a Chirp signal with pulse duration NT, sampling interval is T and signal bandwidth $N\Delta f$. Then the slope of stepped-frequency can be given as $k = \frac{N\Delta f}{NT} = \frac{\Delta f}{T}$. Dechirp processing for linear fm waveform corresponds to DFT processing for stepped-frequency waveform.

Stepped-frequency input data (vector) for one burst involves different frequency components related to scatterer ranges. So DFT processing finds the peaks at these frequency locations that are directly related to range profiles.

3.4 Generation of Stepped Frequency Waveform (SFW) Data

ISAR data model that is used is a 2D matrix and it is generated by collecting N different frequency sampled signals for M different aspect angles of target. In other words radar data collection is done in frequency domain.

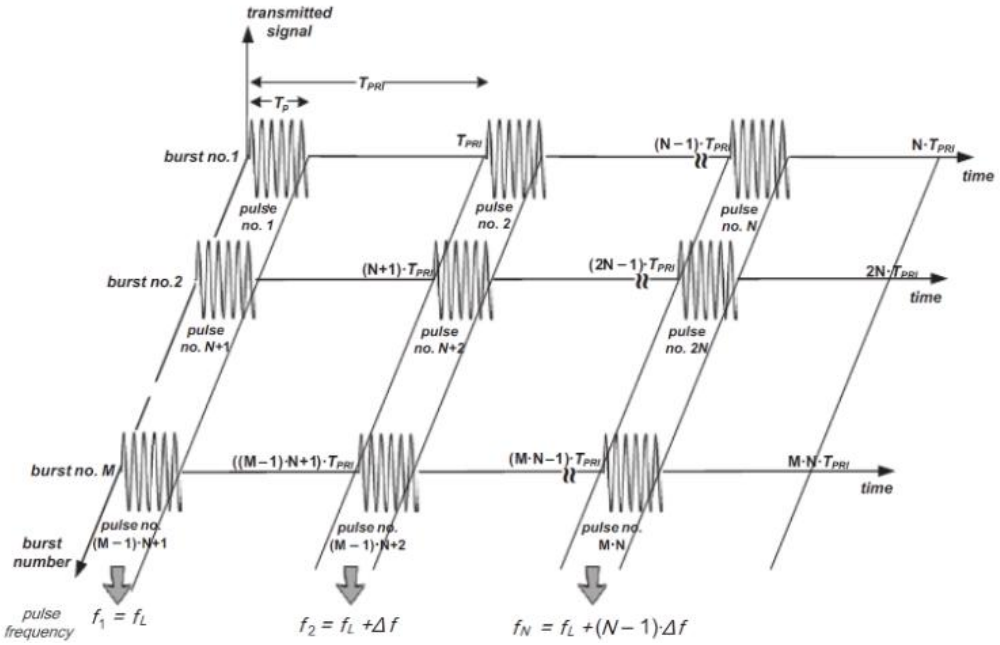

Figure 3-5: Collection of Stepped Frequency Radar Data [23]

Stepped-frequency data simulator has some assumptions: [24]

Assumption 1: For each angular position of target a sequence of pulses at carrier frequencies $f_n = f_L + n\Delta f$ for $n = 0,1,2, \dots N-1$. are transmitted by the radar.

Assumption 2: Target takes angular positions $\theta_m = m\Delta\theta$ for $m = 0,1,2, \dots M-1$.

By using the assumptions ISAR stepped-frequency discrete simulation data can be generated.

$$s(n,m) = \sum_{k=1}^{K} p(x_k, y_k)\, e^{j2\pi f_n 2(R_0 + x_k \sin\theta_m + y_k \cos\theta_m)/c} \tag{3.13}$$

R_0 is the distance between radar and the center of main target. Equation (3.13) assumes that there is no translational motion and the rotational velocity of target is known. ($\Delta\theta = \omega T$, *T: pulse repetition interval*) Aspect angle change between succesive slow-time samples are the function of rotational velocity of target.

After determining target model (point scatterer locations, rotational velocity etc.) transmission waveform (LFM or SFW), radar simulation parameters (carrier frequency, bandwidth, sampling rate, PRI etc.) and data size, ISAR input data matris is generated as it is expressed in Equation (3.6) or (3.13).

CHAPTER 4

ESTIMATION OF ROTATIONAL VELOCITY

In ISAR applications rotational velocity of the target is required to be known in order to reconstruct the image. If the rotational velocity is constant, scatterers on the cross-range axis are resolved according to their radial velocity as a result of rotational motion. Doppler effect of the scatterers lying on the upper part of the axis is stronger than the others. As a result, cross-range information can be extracted.

For the ISAR image system rotational parameters are the key elements of cross-range scaling. For instance typical range-Doppler algorithm requires these parameters at the end of the FFT operations to complete cross-range scaling of the image.

The sequence of samples which are taken at each pulse repetition interval is named as slow time signal. Estimation of the rotational velocity is equivalent to the problem of estimating chirp rate of the slow time signal for one range bin. Because slow-time data for one range cell that includes scatterers can be modelled as the summation of linear FM signals with unknown parameters.

In this thesis main problem is the ISAR image reconstruction. Detailed information about the rotation rate estimation is not given in the thesis. But some approaches and implementations about the estimation problem are given.

In the classical ISAR formulation phase components φ_x and φ_y are given

$$\varphi_x = \frac{4\pi f}{c} x \sin(\omega t) \tag{4.1}$$

$$\varphi_y = \frac{4\pi f}{c} y \cos(\omega t) \tag{4.2}$$

Under the assumption of constant rotation rate, ω, by Taylor series expansion of Equation (4.1) we obtain : [25]

$$\varphi_x \cong \frac{4\pi f}{c} x(\omega t - \frac{\omega^3 t^3}{6} + \cdots) \tag{4.3}$$

and by Taylor expansion of Equation (4.2):

$$\varphi_y \cong \frac{4\pi f}{c} y(1 - \frac{\omega^2 t^2}{2} + \cdots) \tag{4.4}$$

ISAR angle variation is assumed to be small and the range cell of the point scatterer doesn't have a large variation from one PRI to the next. After translational motion compensation is done, cross range slow-time received signal for k^{th} scatterer can be written as [11]

$$s_k(t_m) = \sigma_k e^{-j\frac{4\pi}{\lambda}R_0} e^{j2\pi(f_k t_m + \frac{1}{2}\gamma_k {t_m}^2)} \tag{4.5}$$

First term is not important and it has no effect on ISAR imaging. As it can be seen that for any scatterer in one slant-range cell, slow-time sequence can be modeled as a LFM (chirp) signal. Then total received signal $s(t_m)$ from a range cell can be expressed as the summation of them

$$s(t_m) = \sum_{k=1}^{K} s_k(t_m) \tag{4.6}$$

$$s(t_m) = \sum_{k=1}^{K} \sigma_k e^{j2\pi(f_k t_m + \frac{1}{2}\gamma_k {t_m}^2)} \tag{4.7}$$

where *K* is the number of scatterers in that range cell. Every scatterer has its own center frequency and chirp rate. Theoretically, cross-range received signal has 2*K* unknown LFM signal parameters to be estimated.

$$f_k = \frac{2f_0}{c}\omega x_k \text{ (center frequency)} \tag{4.8}$$

$$\gamma_k = \frac{2f_0}{c}\omega^2 y_k \text{ (chirp rate)} \tag{4.9}$$

As a result, estimation of rotation angle requires the estimation of multi component LFM signals. To make the problem easier, sometimes it is assumed that there is only one scatterer in one range cell and the phase terms of the received signal are considered.

There exist different techniques to estimate the rotational velocity of target. In this thesis, the problem will be investigated with three different types of these approaches:

4.1 Grid Search Approach

This method is the basic parameter estimation method. We express the estimation of velocity as a minimization problem and search a rectangular grid to find the optimum values.

Step 1: Find the range information *y* by using match filter or IFFT approaches and assume that R_0 is known.

Step 2: Express the slow time sequence as the function of two unknown parameter by using Taylor series expansions.

$$s(n) = e^{j\frac{4\pi f_0}{c}(R_0+y+a_1 n+a_2 n^2)} \tag{4.10}$$

Where $a_1 = \omega x T$ and $a_2 = -\frac{y}{2}\omega^2 T^2$

Step 3: Construct estimated signal represantation and solve the maximization problem. In order to solve the problem try all possible values on the grid and choose the pair that gives maximum value

$$\widehat{a_1}, \widehat{a_2} = \arg\max_{a_1,a_2} \left| s(n) e^{-j\frac{4\pi f_0}{c}(R_0+y+a_1 n+a_2 n^2)} \right| \tag{4.11}$$

$$\widehat{a_1}, \widehat{a_2} = \arg\max_{a_1,a_2} \sum_{n=1}^{N} s(n) e^{-j\frac{4\pi f_0}{c}(R_0+y+a_1 n+a_2 n^2)} \tag{4.12}$$

where N is the length of the slow time sequence.

Step 4: After finding the estimates $\widehat{a_1}, \widehat{a_2}$, rotational velocity and the cross range *x* can easily be obtained as:

$$\widehat{\omega} = \sqrt{\frac{-2\widehat{a_2}}{yT^2}} \tag{4.13}$$

$$\widehat{x} = \frac{\widehat{a_1}}{\widehat{\omega}T} \tag{4.14}$$

As a result, grid search procedure uses classical maximization approach to find the chirp rate of cross-range signal which is directly related to the rotational rate of target.

Simulations:

Figure 4-1 is an example of output error function of 200×200 grid points where there are three scatterers in one range bin. As it is seen that plotting error function at 40000 sample points gives three peak locations that are directly related to three scatterers. This simulation is done for a target that is rotated with 0.6553rad/s and finally common y-locations(velocity) of these three peaks in 2-dimensional grid give the estimated velocity as 0.6558rad/s in the case of input SNR=20 dB.

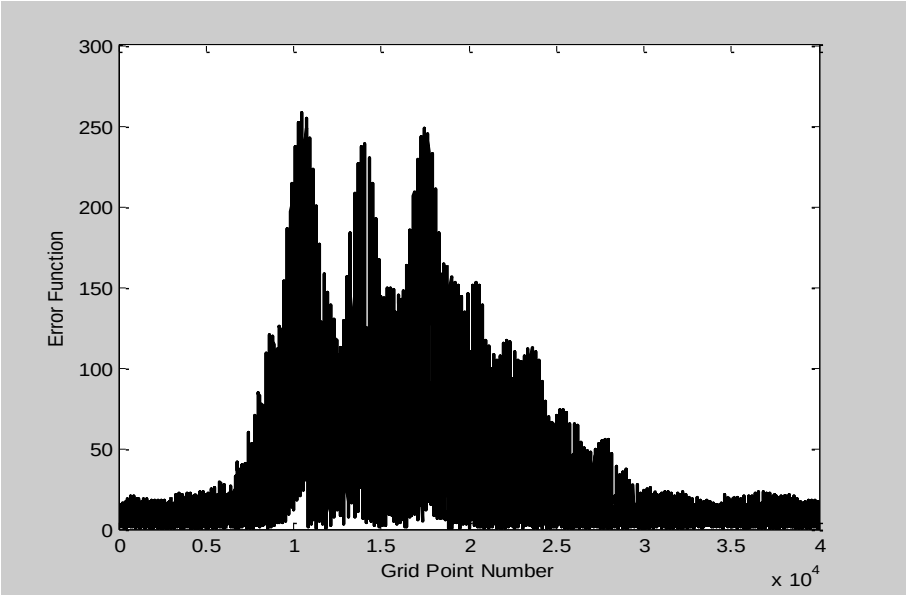

Figure 4-1: Error Function of the 200x200 Grid for 3 Scatterers in One Range Bin

The same procedure is repeated for different true velocity values in Figure 4-2. Here the estimated and actual velocities are plotted in the same figure. So that the estimation performance with input SNR 20 dB can be visualized.

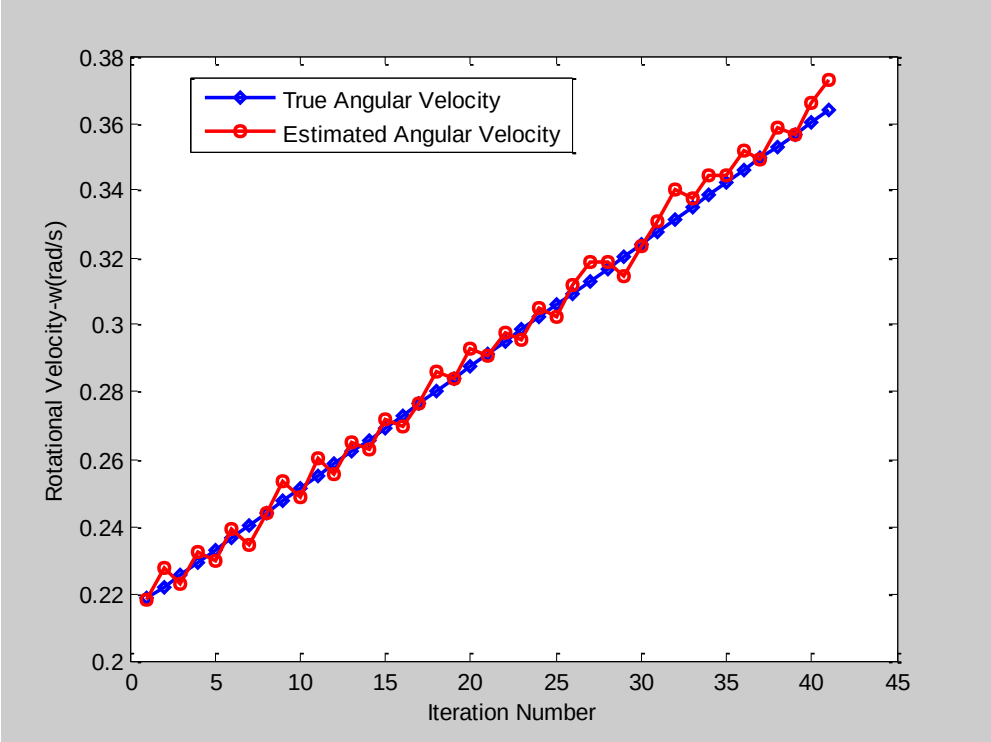

Figure 4-2: Estimated Values of Rotational Velocity Using Grid Search

4.2 WVD Slope Approach

The instantenous azimuth ISAR image can be obtained by using time-frequency analysis methods as will be shown in Section 5.5. If one range bin is considered then instantenous frequency of cross-range signal becomes related to the rotational rate of the target. Time variation of Doppler frequency can be viewed using time-frequency analysis methods. WVD slope approach is a time-frequency technique to estimate the rotational velocity of target.

One can apply time-frequency analysis to one range bin after range compression operation.

WVD is very suitable for the analysis of multiple component LFM signal [11]. Although it has a cross-term interference effect, the WVD spectrum is enough to give velocity information.

For one range cell, by taking WVD transform of slow time sequence one can extract the multiple LFM components. Slow-time WVD spectrum is concentrated on several lines in the time-frequency plane with different slopes and starting points [11]. Each line represents one different cross-range scatterer and linear representation of this line directly estimates the unknown linear fm signal parameters.

An algorithm can be constructed to find the rotational velocity by using WVD transform analysis. In the simulations it is assumed that there is only one scatterer in a specific range cell and the rotational velocity of target is constant.

Step 1: Find the multiplication of cross signals $s_k(t_m + \frac{\tau}{2}) s_k{}^*(t_m - \frac{\tau}{2})$ for the time instant $t_m = mT$ where $m = 1 \dots M$.

$$s_k\left(t_m + \frac{\tau}{2}\right) s_k{}^*\left(t_m - \frac{\tau}{2}\right) = e^{j2\pi[f_k(t_m - \frac{\tau}{2}) + \frac{1}{2}\gamma_k(t_m - \frac{\tau}{2})^2]} e^{-j2\pi[f_k(t_m + \frac{\tau}{2}) + \frac{1}{2}\gamma_k(t_m + \frac{\tau}{2})^2]}$$

$$= e^{j2\pi(f_k + \gamma_k t_n)\tau} \tag{4.15}$$

Step 2: Take the Fourier transform of the signal and find the one row of the WVD transform time-frequency plane [11].

$$WVD_k(t_m, f) = \int_{-T_a/2}^{+T_a/2} s_k\left(t_m + \frac{\tau}{2}\right) s_k{}^*\left(t_m - \frac{\tau}{2}\right) e^{-j2\pi f\tau} d\tau$$

$$= \int_{-T_a/2}^{+T_a/2} e^{j2\pi(f_k + \gamma_k t_n)\tau} e^{-j2\pi f\tau} d\tau$$

$$= T_a sinc[\pi T_a(f - (f_k + \gamma_k t_m))] \tag{4.16}$$

where T_a is the coherent pulse interval and f_k, γ_k are the center frequency and chirp rate corresponding to that scatterer. From Equation (4.16), it can be seen that WVD transform of cross-range signal is a line that locates on the time-frequency plane. Intercept of the line gives centre frequency information. Slope of the line is related to the chirp rate.

Step 3: Since every time instant has a peak location on the plane find the maximum location of each row of WVD plane and see the line on time-frequency plane.

Step 4: Find a linear approximated expression for the line (ax+b).

Step 5: Use the slope of that line to find the chirp rate and obtain rotational velocity directly.

$$\hat{\omega} = \sqrt{\frac{slope * PRF^2 * \lambda}{M * y}} \tag{4.17}$$

Step 6: Find the intercept of the line to get the center frequency which is related to cross range *x* and ω. Finally cross-range can be found by using the expression:

$$\hat{x} = \frac{\lambda(\frac{M}{2} - intercept)}{2MT\hat{\omega}} \tag{4.18}$$

Simulations:

In the simulations single point scatterer in one range cell is investigated and the time-frequency plane which concentrates on one line is analysed. For multiple cross-range scatterers number of lines increases and by extracting multiple lines from the time-frequency plane it is possible to resolve multiple frequency components of LFM signal. Basically, the procedure of estimating the LFM components and meaning of line parameters is the same as single scatterer case.

Table 4.1: Simulation Parameters for WVD Line of Two Scatterers with Different Velocities

Parameter Name	**Scatterer 1**	**Scatterer 2**
ω: Angular Velocity(rad/s)	0.043	0.174
x: Cross-range(m)	10	10
y: Range(m)	30	30
WVD-plane line $ax + b$	$0.0015x + 307.45$	$0.0248x + 377.67$

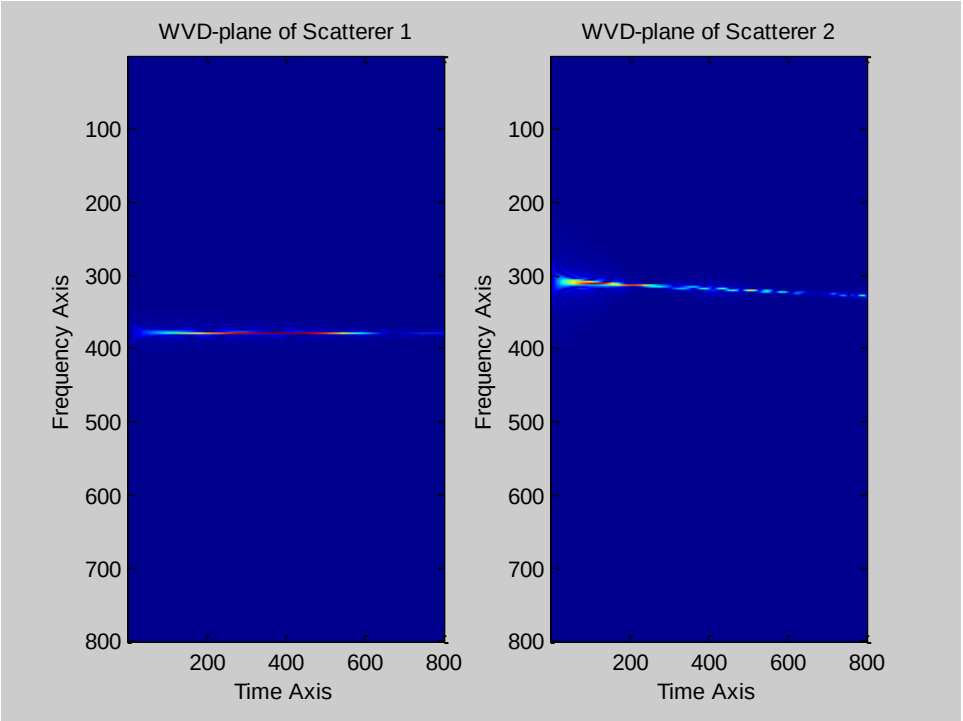

Figure 4-3: Concentrated Lines in WVD Planes for Two Different Scatterers

Simulation parameters for WVD line approach are given in Table 4.1. In this simulation it is observed that WVD plane of cross-range signal is concentrated on a line and slope of that line is proportional to the square of ω. Since $\omega_2 = 4\omega_1$, slope of the line for Scatterer 2 becomes 16 times as the Scatterer 1 $\left(\frac{0.0248}{0.0015} \approx 16\right)$. Similarly there exists a linear relationship between intercept points corresponding to angular velocity ratio $\frac{\omega_2}{\omega_1}$ which is $\frac{(400-377.67)}{(400-307.45)} \approx 4$ in Figure 4-3.

We can observe how to make an approximation of line in WVD-plane from Figure 4-4. Here there is a point scatterer that rotates with an angular velocity of $8.76^{\circ}/s$. After the line approximation estimated angular velocity is calculated as $8.85^{\circ}/s$ by using the slope of line.

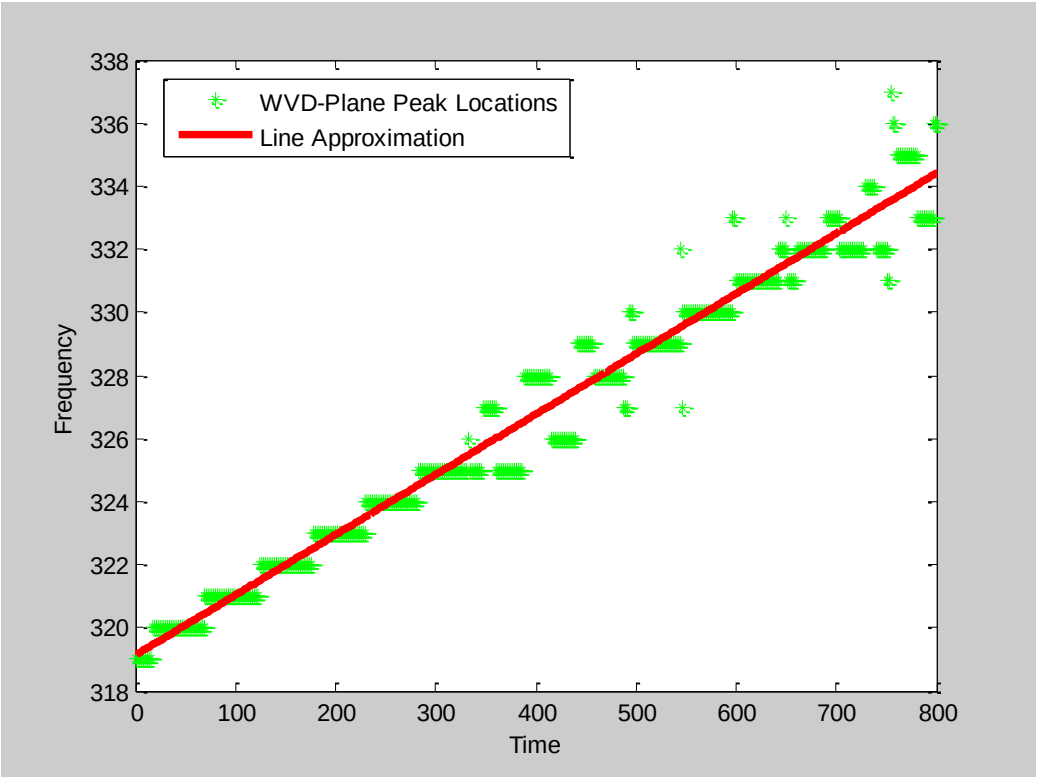

Figure 4-4: Line Approximation for WVD Spectrum of Cross-Range Response of One Range Cell

Repeating the WVD-approach for different true velocity values constructs the Figure 4-5. Here the estimated and actual velocities are plotted in the same figure and the estimation performance of WVD approach with input Signal to Noise Ratio (SNR) being 20dB is visualized.

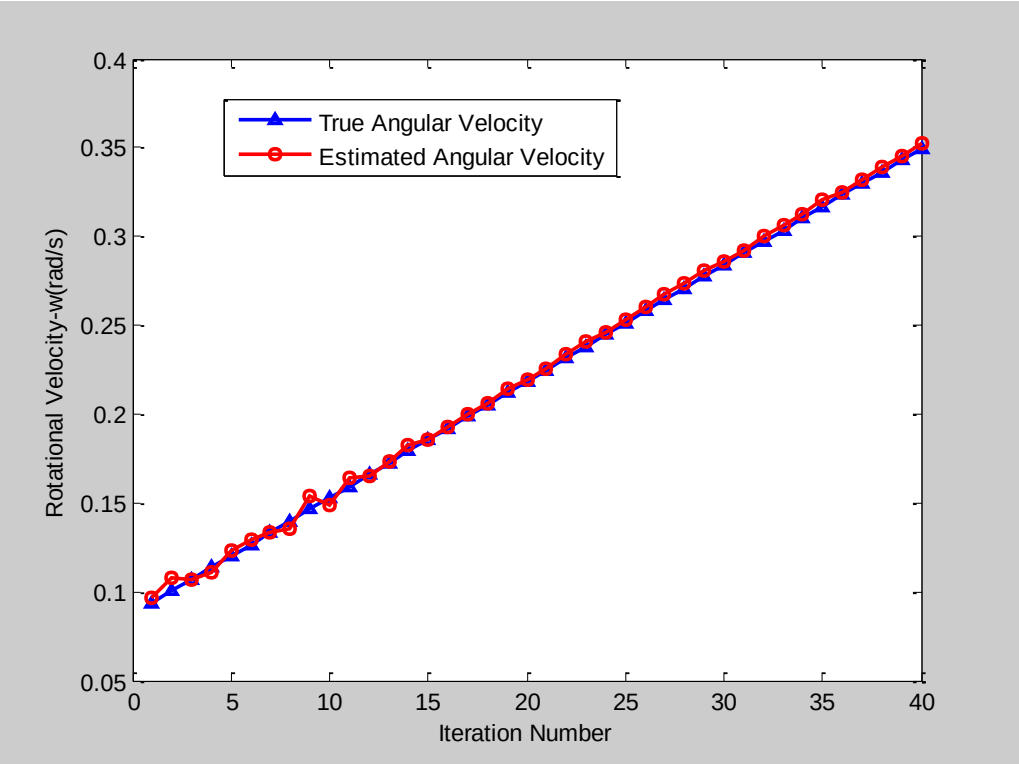

Figure 4-5: Estimated Values of Rotational Velocity Using WVD-Approach

4.3 Radon Wigner-Hough Transform Approach

This is an approach to analyse multi-component LFM signals, based on Hough transform of WVD which has similarities with the previous approach, because main purpose of this approach is to find optimum line on time-frequency plane that corresponds to cross-range signal. In order to find unknown parameters, a line integral over WVD of signal is used.

The evaluation of all the line integrals over the time-frequency plane can be performed by the the Hough Transform (HT) [12]. Since there is an integration over

WVD lines, one can degrade cross-term interference effects by applying Hough transform.

This approach projects the time-frequency plane to a parameter plane on which we will search the LFM components. In other words, the HT performs integrations along lines on the time-frequency plane, and the value of each integral is affected to the point (f, g) corresponding to the parameters of the line [13]. Locations of the peaks of Wigner-Hough transform (WHT) are directly related to rotation rate and cross-range distance.

Given the received signal $s(t)$ one can express the WHT as the mapping from WVD plane to the line parameter plane $(f \times g)$ by constructing the following line integral [12].

$$WH_s(f,g) = \int_{-\infty}^{+\infty}\int_{-\infty}^{+\infty} s(t+\tau/2)s^*(t-\tau/2)e^{-j2\pi(f+gt)\tau}\,d\tau dt \tag{4.19}$$

This equation can be interpreted as the line integral of WVD:

$$\begin{aligned} WH_s(f,g) &= \int_{-\infty}^{+\infty}\int_{-\infty}^{+\infty} W_s(t,v)\delta(v-f-gt)\,dtdv \\ &= \int_{-\infty}^{+\infty} W_s(t,f+gt)\,dt \end{aligned} \tag{4.20}$$

Also it is equal to the Fourier Transform of the slices of the Ambiguity function, intersecting the origin of time-frequency plane,

$$WH_s(f,g) = \int_{-\infty}^{+\infty} A_s(\tau, g\tau)e^{-j2\pi f\tau}\,d\tau \tag{4.21}$$

where WVD and the Ambiguity function are defined as [12]

$$W_s(t,f) = \int_{-\infty}^{+\infty} s(t+\tau/2)s^*(t-\tau/2)e^{-j2\pi f\tau}d\tau \tag{4.22}$$

$$A_s(\tau,f) = \int_{-\infty}^{+\infty} s(t+\tau/2)s^*(t-\tau/2)e^{-j2\pi ft}dt \tag{4.23}$$

It can be easily seen that two equations are similar expressions and the implementation can be done by choosing any of them. In this thesis the simulations

are based on the line integral method. To apply this technique to the finite length signal, first, the formulation should be discretized. Then given the discrete slow time sequence *s(n), n=0,1,2…N-1*, discrete Wigner-Hough Transform is constructed as:

$$W_s(n,k) = \sum_{n=0}^{N-1}\sum_{k=0}^{N-1} s(n+k)s^*(n-k)\, e^{-j4\pi k(f+gn)} \tag{4.24}$$

Where $s(n+k) = 0\ if\ n+k > N-1$ and $s^*(n-k) = 0\ if\ n-k < 0$. The simulations show that locations of the peaks areof WHT are the LFM parameters we try to find. Unlike the WVD approach, interference terms between two signals degrade, because integration over lines produces gain energy ratio between auto terms and cross terms [12].

Simulations:

Here are the scatterers that are in the same range bin and rotating with the same velocity for one simulation. In three simulations, rotational velocities and cross ranges of targets are estimated by using Wigner-Hough transform. Simulation parameters are given in Table 4.2.

Assuming that output parameter plane has dimensions of *a* and *b* that are related to intercept and slope of line $ax + b$, the change of the estimated peak locations can be visualized for three simulations. Since there are 3 scatterers in one range bin, output spectrum has 3 peaks with different *a*, but same *b*. If the rotational velocity (ω) is changed, locations of peaks are shifted in both dimensions. Because one dimension points to ωx and second dimension points to the rotational velocity ω^2, assuming that y is known, where x is cross-range and y is slant range. Figure 4-6, Figure 4-7 and Figure 4-8 are 3-dimensional view of the outputs. From Figure 4-9 and Figure 4-10, 2D cross-sections of the outputs for all simulations can be seen.

Table 4.2: Simulation Parameters for WHT of Cross-Range Signal Including Three Scatterers

Rotational Velocity	**Parameter Name**	**Scatterer 1**	**Scatterer 2**	**Scatterer 3**
Simulation1 $\boldsymbol{\omega_1 = 0.175}$ **rad/s**	x: Cross-range(m)	-10	-16	18
	y: Range(m)	30	30	30
Simulation2 $\boldsymbol{\omega_2 = 0.263}$ **rad/s**	x: Cross-range(m)	-10	-16	18
	y: Range(m)	30	30	30
Simulation3 $\boldsymbol{\omega_3 = 0.350}$ **rad/s**	x: Cross-range(m)	-10	-16	18
	y: Range(m)	30	30	30

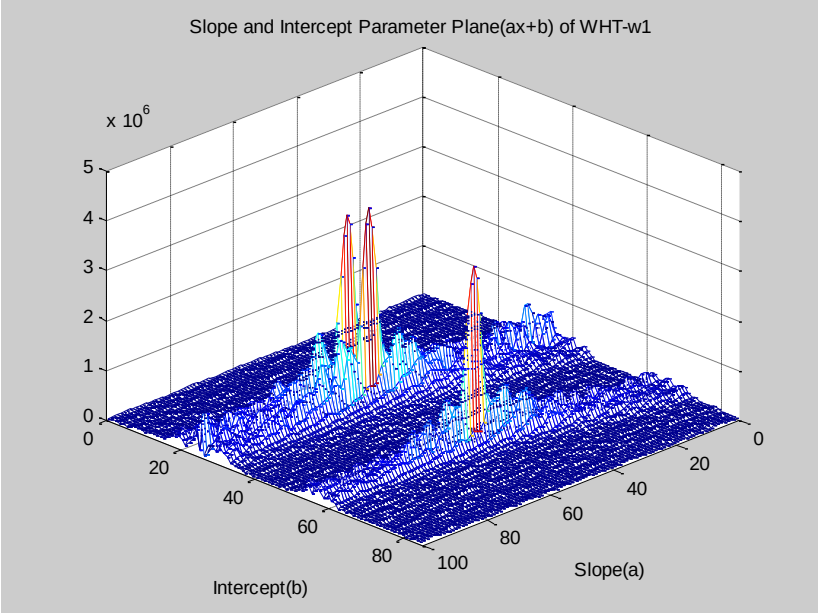

Figure 4-6: Output WHT Plane of the Simulation-1

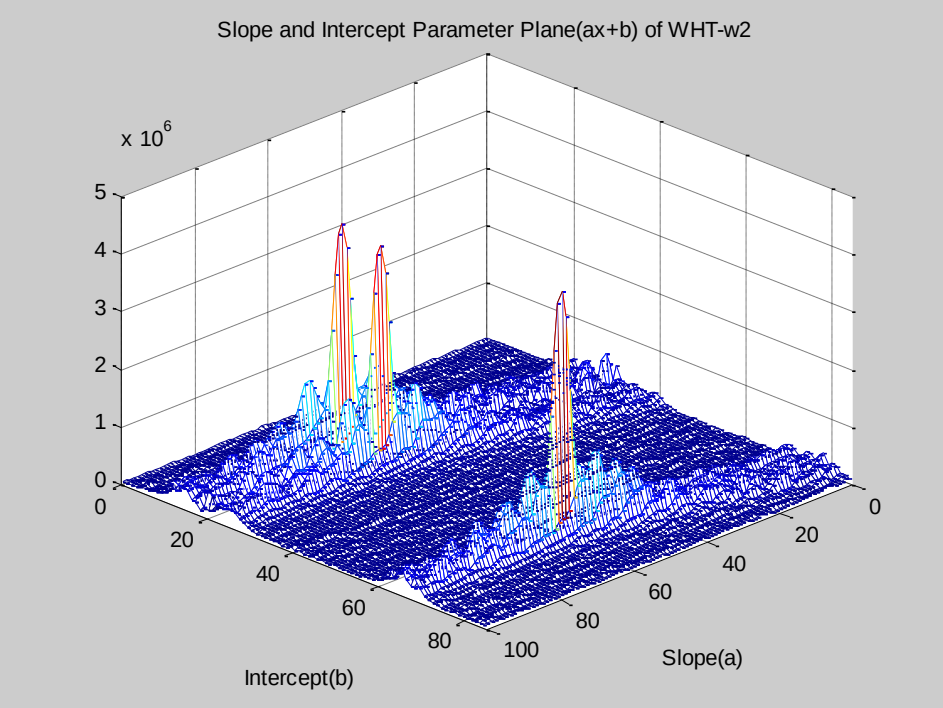

Figure 4-7: Output WHT Plane of the Simulation-2

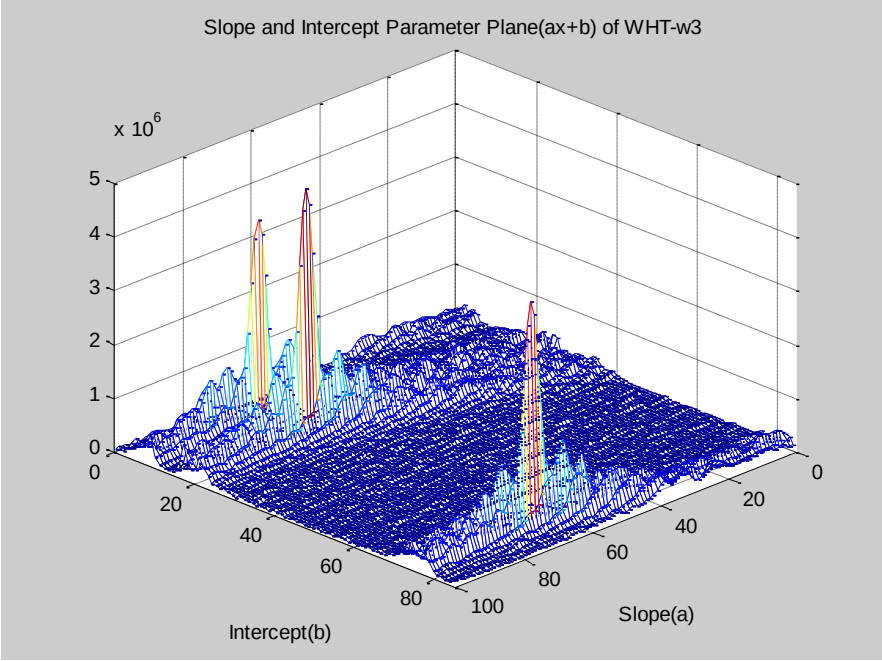

Figure 4-8: Output WHT Plane of the Simulation-3

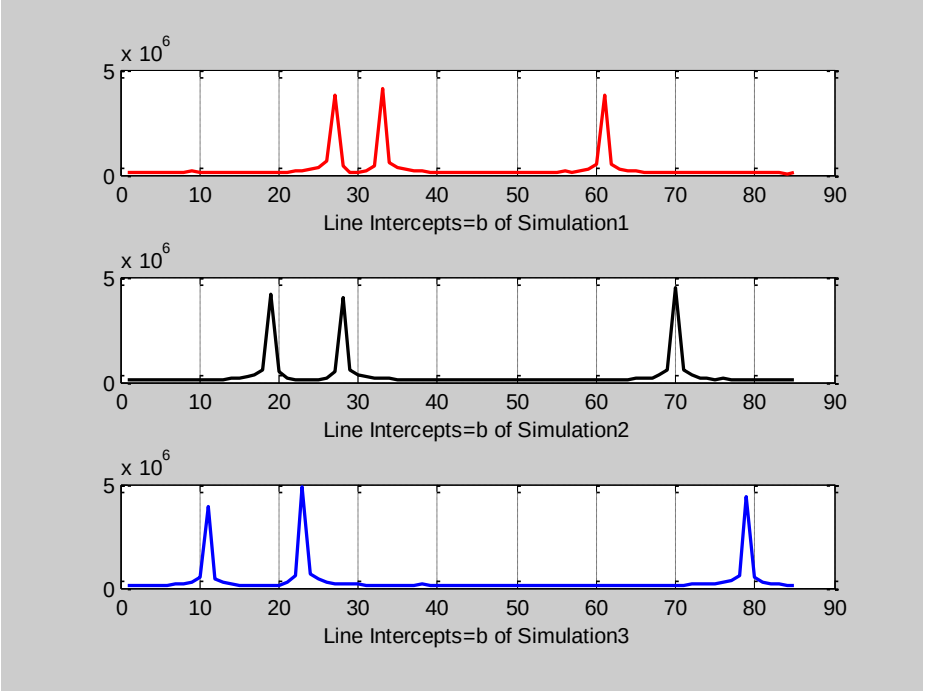

Figure 4-9: Line Intercepts Estimations of Simulations

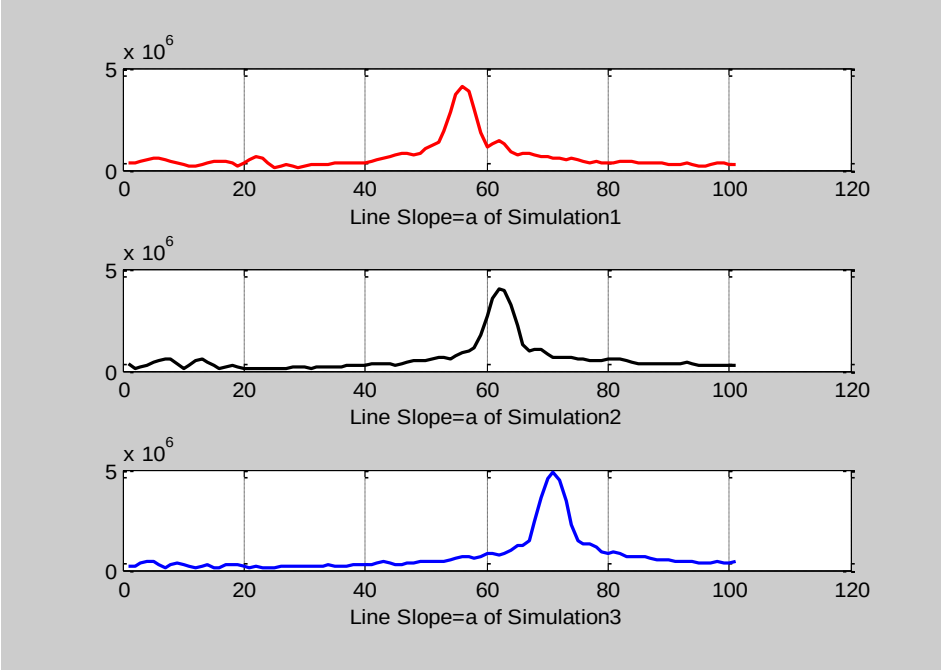

Figure 4-10: Line Slope Estimations of Simulations

CHAPTER 5

IMAGE RECONSTRUCTION ALGORITHMS

In this chapter ISAR image reconstruction algorithms will be discussed and applied to some radar targets.

5.1 Range-Doppler Algorithm

In ISAR applications, wide signal bandwidths and synthetic aperture which is the result of rotational motion of target are used to achieve high resolution. Range of the scatterers is found by using the pulse compression or inverse FFT methods.

As the object is rotated, scattering centers crossing through the range cells cause signals corresponding to that cell to vary. During the rotation, scatterers that are far away from the rotation center create larger Doppler changes in the signal. This difference in a specific range cell can be processed to obtain cross-range of scatterers [26].

To apply range-Doppler algorithm complex target response is received for a fixed aspect angle as a function of frequency. This return collection is repeated for a number of discrete angles. Fourier samples for each viewing angle are processed by using inverse FFT operation, so that range profiles of target can be created. The returns for each range cell which is a function of rotation angle are processed by FFT to find the cross-range of the scatterers [26].

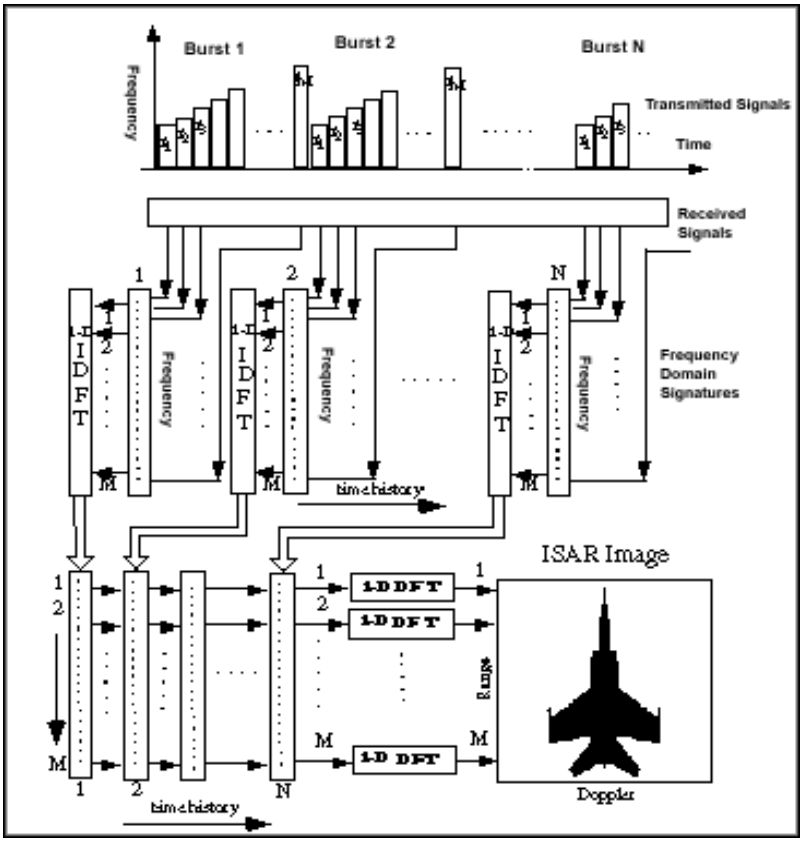

Figure 5-1: Range-Doppler Algorithm for ISAR Image Reconstruction [2]

Final data needs to be scaled in order to know the exact locations of scatterers. In this stage some cross-range scaling methods can be used or rotational velocity is assumed to be known. In previous chapter estimation of rotational velocity was shown, so we will assume that this parameter is known.

Range-Doppler algorithm is based on some assumptions [24] listed below.

Assumption 1: Reflection coefficient of each scatterer in target plane is constant.

Assumption 2: Distance between the center of target and the radar is known to extract the phase component due to this distance can be suppressed from the frequency response.

Assumption 3: Total angular change during the observation time is small.

Assumption 4: Frequency bandwidth of the pulses is much smaller than the carrier frequency.

Assumption 5: Rotational velocity is a known constant parameter

Mathematical expression of total received signal after deconvolution and translational motion processes becomes

$$S_R(f,\theta) = \iint g(x,y)e^{-j2\pi(xX+yY)}dx\,dy \tag{5.1}$$

where X and Y are called spatial domain frequency components.

$$X = \frac{2f}{c}\sin[\theta(t)] \tag{5.2}$$

$$Y = \frac{2f}{c}\cos[\theta(t)] \tag{5.3}$$

Total reflectivity function in the Fourier domain is limited by total angle variation $\Delta\theta$ and total signal bandwidth β [3]. Larger bandwidth and angle variation increases the range and cross-range resolution.

In the applications Fourier domain samples are discrete and they locate on a grid on the spatial frequency domain. The frequncies are the radius and aspect angles are the angle component of the polar grid. Assumption of constant rotation vector provides a uniformly spaced polar grid which may not be true for more complicated motions.

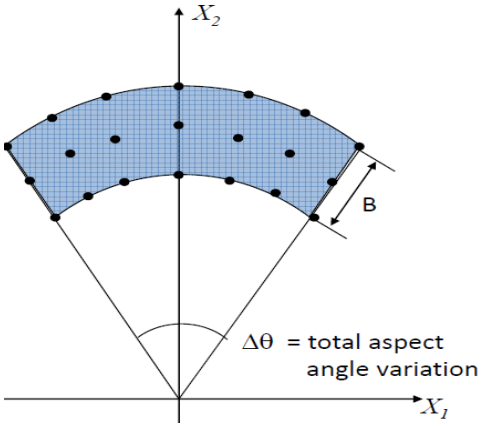

Figure 5-2: Polar Domain Samples of Received ISAR Signal

For 2D-FFT calculation to give accurate results frequency samples should be evenly spaced and grid sould have a rectangular shape.

Range-Doppler technique can be directly implemented when the angle variation is small enough (< 5). Because in this condition, frequency domain can be approximated by means of a rectangular grid. Constant rotational velocity provides a grid that is evenly spaced. Figure 5-3 shows the rectangular approximation of frequency domain for small angular rotations.

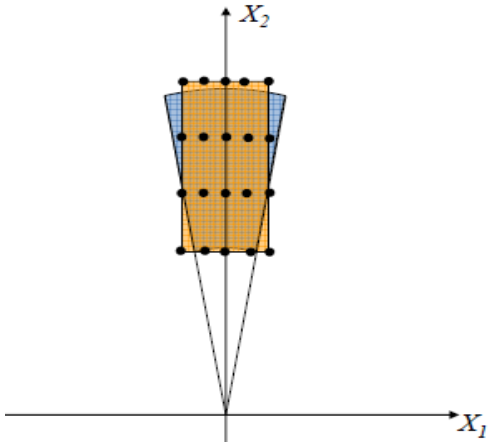

Figure 5-3: Rectangular Approximation of Small Angle Fourier Domain Data

The discrete reconstruction formula and mathematical assumptions related to these rectangular approximations are written as

$$S_R(f,k) = \sum_{i=1}^{M} a_i exp\{-j2\pi[Xx(i) + Yy(i)]\} \tag{5.4}$$

$$X = \frac{2f}{c}\sin[\theta(kT)] \approx \frac{2fk\Delta\theta}{c} \approx \frac{2f_0 k\Delta\theta}{c} \tag{5.5}$$

$$Y = \frac{2f}{c}\cos[\theta(kT)] \approx \frac{2f}{c} \tag{5.6}$$

where f_0 is the central frequency and frequency steps are small compared to the f_0. (Assumption 4)

Under the assumptions, frequency spectrum of received signal can be defined as

$$S_R(f,k) = \sum_{i=1}^{M} a_i exp\left\{-j2\pi\left[\frac{2f_0 k\Delta\theta}{c}x(i) + \frac{2f}{c}y(i)\right]\right\} \quad (5.7)$$

Now 2D-FFT operation through the range-Doppler matrix can be implemented to reconstruct the target reflectivity function.

$$a_i(x,y) = \sum_f \sum_\theta S_R(f,k) e^{j2\pi[f_x x(i) + f_y y(i)]} \quad (5.8)$$

After finding the reflectivities, locations of peaks in spatial frequency domain should be mapped onto phsyical target $x-y$ plane (scaling). Range-Doppler algorithm steps can be seen in Figure 5-4.

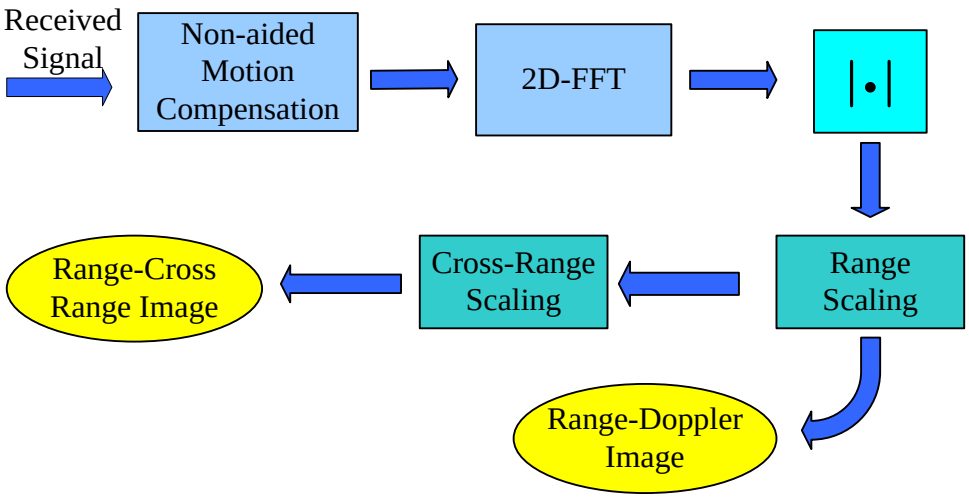

Figure 5-4: Conventional Range-Doppler ISAR Image Reconstruction Algorithm

5.1.1 Range-Cross Range Scaling

After the application of Range-Doppler algorithm, ISAR image is scaled in fast and slow time domain [3]. In order to represent the image points in both range and cross-range domain, scaling parameters should be multiplicated with ISAR image.

At this stage we assume that rotation vector of target is known. The effective rotation vector depends on the relative motion of the target with respect to the radar

[3]. In real applications it is usually an unknown parameter and it should be estimated by using techniques discussed in CHAPTER 4. If the rotation velocity is not estimated then only the target shape with unknown length can be observed.

Assuming that point coordinates in range-Doppler plane are l_1 and l_2, final range and cross-range distances can be obtained by using following two equations.

$$r = \frac{c(l_1 - M/2)}{\Delta f} \tag{5.9}$$

$$cr = \frac{c(l_2 - N/2)}{f_0 \omega N T} \tag{5.10}$$

5.1.2 Simulations

Target model which is used in RD simulations is shown in Figure 5-5 and simulation parameters are given in Table 5.2.

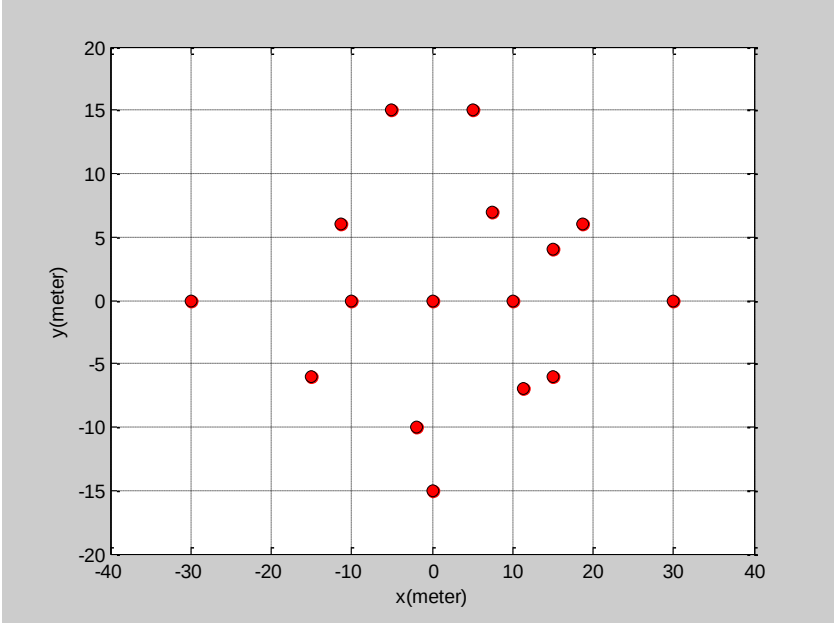

Figure 5-5: Target Model for RD Simulations

Table 5.1: RD-ISAR Simulation-1 Parameters

Symbol	Name	Value
N	Number of Bursts	256
M	Number of Frequency Samples	500
f_c	Carrier Frequency	10 GHz
T	Pulse Repetition Interval	1 ms
B	Signal Bandwidth	400 MHz
Δf	Frequency Step Size	800 KHz
ω	Angular Velocity	0.171 rad/s
$\Delta\theta = \omega NT$	Total angle variation	2.5°

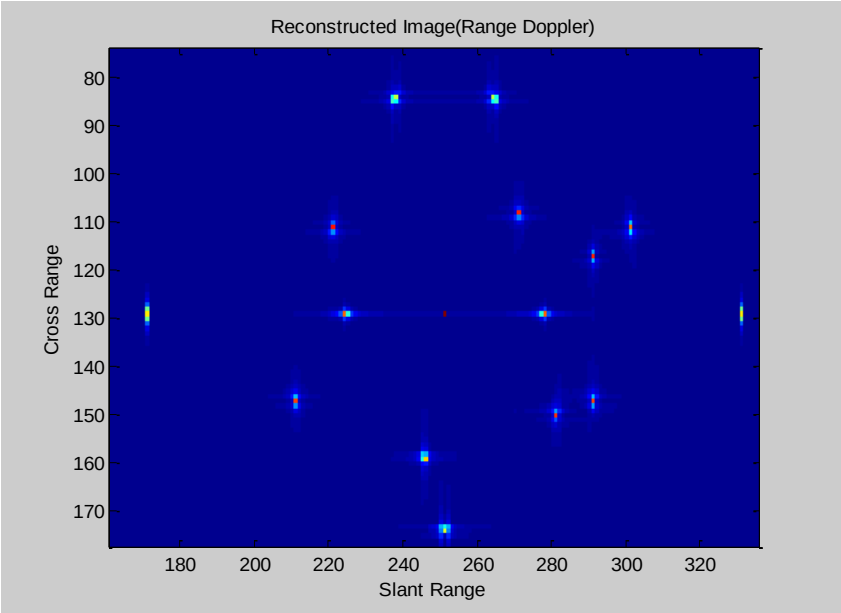

Figure 5-6: Range-Doppler ISAR Image for $\Delta\theta$ =2.5°

Table 5.2: RD-ISAR Simulation-2 Parameters

Symbol	Name	Value
N	Number of Bursts	512
M	Number of Frequency Samples	500
f_c	Carrier Frequency	10 GHz
T	Pulse Repetition Interval	1 ms
B	Signal Bandwidth	400 MHz
Δf	Frequency Step Size	800 KHz
ω	Angular Velocity	0.171 rad/s
$\Delta\theta = \omega NT$	Total angle variation	5°

Two more simulations are carried out for $\Delta\theta$ =5° and $\Delta\theta$ =12°. Simulation parameters are given in Table 5.2 and Table 5.3, and corresponding output images are shown in Figure 5-7 and Figure 5-8.

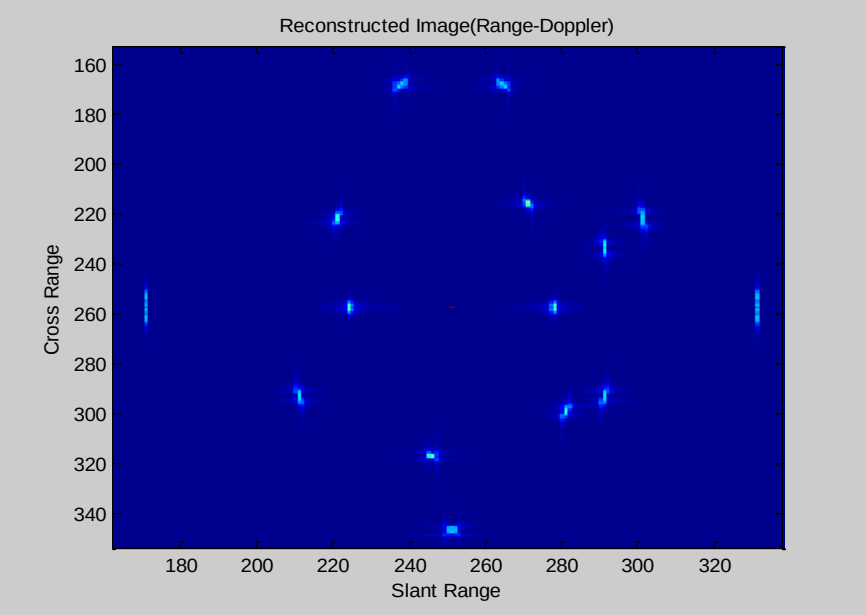

Figure 5-7: Range-Doppler ISAR Image for $\Delta\theta$ =5°

Table 5.3: RD-ISAR Simulation-3 Parameters

Symbol	**Name**	**Value**
N	Number of Bursts	1024
M	Number of Frequency Samples	500
f_c	Carrier Frequency	10 GHz
T	Pulse Repetition Interval	1 ms
B	Signal Bandwidth	400 MHz
Δf	Frequency Step Size	800 KHz
ω	Angular Velocity	0.2047 rad/s
$\Delta\theta = \omega NT$	Total angle variation	12°

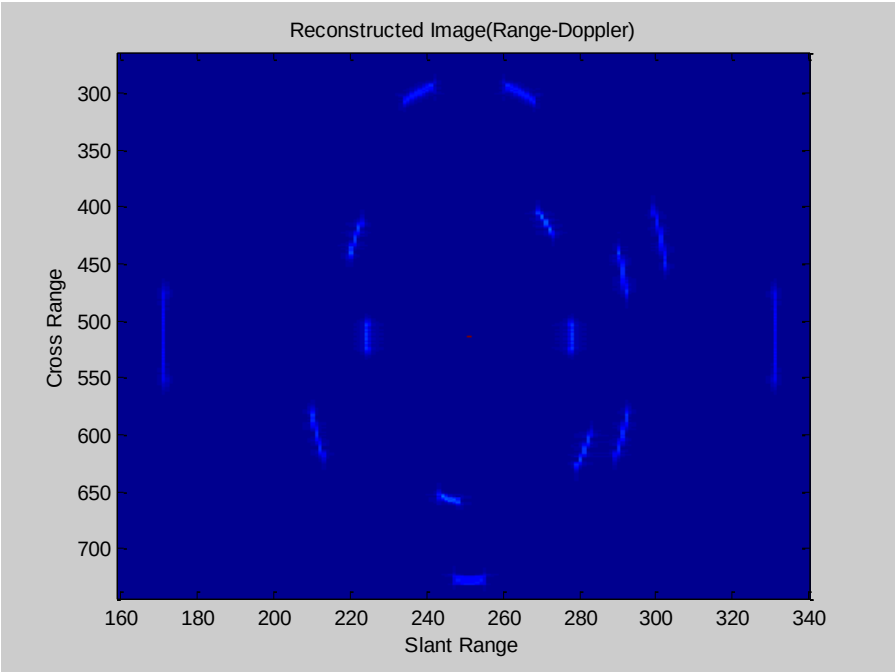

Figure 5-8: Range-Doppler ISAR Image for $\Delta\theta = 12°$

In the simulation shown in Figure 5-8, Range-Doppler algorithm rectangular assumptions don't work. When the total aspect angle is too large, spatial frequency domain data is not in its rectangular shape anymore. In this case 2D-FFT algorithm gives unsatisfactory results as it is seen from Figure 5-8.

5.2 2D-MUSIC Algorithm

The conventional 2D-FFT algorithm for ISAR imaging can be limited by observation angle and bandwidth, because higher resolution images require large observation angle and bandwidth. Some spectral estimation based ISAR algorithms such as MUSIC, ESPRIT can overcome these limitations to improve the image quality [6]. 2D-MUSIC algorithm is based on the estimation of 2-dimensional frequency locations.

As we know that received signal from radar target can be represent as the summation of each scatterer response. If the received signal is collected over a small angular sector then the rectangular approximation ($\sin\theta \approx \theta \; and \;\; \cos\theta \approx 1$) can be used, otherwise frequency-angle domain data should be interpolated to Cartesian coordinates [6].

Rectangular assumption based formulation of ISAR received signal can be written as

$$x(m,n) = \sum_{i=1}^{K} s_k e^{[-j\frac{4\pi}{c}(f_m{}^x x_k + f_n^y y_k)]} + u(m,n) \tag{5.11}$$

where $f^x = f\cos\theta \;\; and \; f^y = f\sin\theta$. The received signal model consists of rectangular samples with equal increments in both x and y dimension [6]. So that classical 2D-FFT can be implemented to generate the range-Doppler image.

Using vector notations Equation (5.11) can be written as follows

$$X = AS + U \tag{5.12}$$

$$X = [x_{00}x_{10} \dots x_{M-10}x_{01} \dots x_{M-1N-1}] \tag{5.13}$$

$$S = [s_1 s_2 \dots s_K]^T \tag{5.14}$$

$$U = [u_{00}u_{10} \dots u_{M-10}u_{01} \dots u_{M-1N-1}] \tag{5.15}$$

$$A = [a(x_1, y_1)\; a(x_2, y_2) \dots a(x_K, y_K)] \tag{5.16}$$

$a(x_1, y_1)$ is called mode vector and for each scatterer it can be constructed as

$$a(x_k, y_k) = \begin{bmatrix} e^{-j\frac{4\pi}{c}({f_0}^x x_k + f_0^y y_k)} & e^{-j\frac{4\pi}{c}({f_1}^x x_k + f_0^y y_k)} & \dots \\ e^{-j\frac{4\pi}{c}({f_{M-1}}^x x_k + f_0^y y_k)} & e^{-j\frac{4\pi}{c}({f_0}^x x_k + f_1^y y_k)} & \dots \\ \dots & e^{-j\frac{4\pi}{c}({f_{M-1}}^x x_k + f_{N-1}^y y_k)} & \end{bmatrix}^T \tag{5.17}$$

where T denotes the transpose operation.

This algorithm considers the autocorrelation matrix of radar echo data. Auto correlation matrix of input data sequence can be expressed as

$$R_x = E\{XX^H\} \tag{5.18}$$

where $E\{\}$ denotes the ensemble average of the data. 2D-MUSIC algorithm needs the estimation of auto correlation matrix from the received data. Actually the estimated correlation matrix is an average of the different snapshots, but in radar imaging applications only one snapshot of the received data is available [29]. To estimate the correlation matrix radar input matrix is divided into subarrays and for each subarray one autocorrelation matrix is calculated. Figure 5-9 shows how the subarrays of radar echo data matrix are created [29].

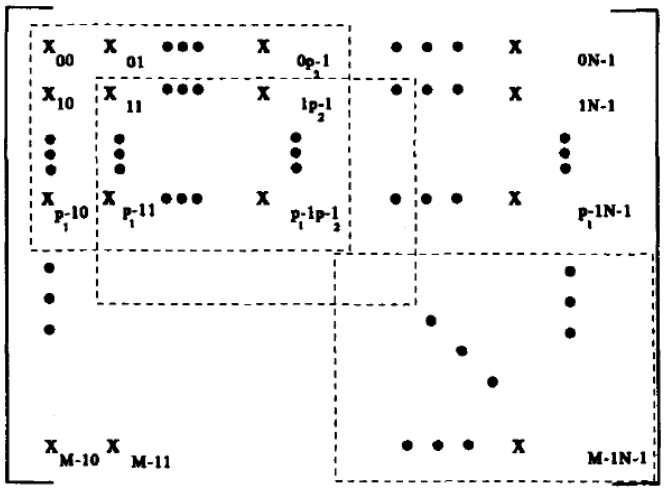

Figure 5-9: Autocorrelation Matrix Estimation by Using Subarrays of Radar Echo Data

From the Figure 5-9 a set of subarrays with dimensions $p_1 \times p_2$ can be seen. If one subarray is reshaped into a column ordered vector then individual autocorrelation matrix x_l corresponding to the l^{th} subarray can be written as

$$\widehat{R_l} = x_l {x_l}^H \tag{5.19}$$

Number of the subarrays in total matrix is $L = (M + 1 - p_1)(N - 1 - p_2)$. Then it is possible to estimate the total autocorrelation matrix by using the below equation [29].

$$\widehat{R_x} = \frac{1}{2L} \sum_{l=1}^{L} \widehat{R_l} + J\, \widehat{R_l}^{*} J \tag{5.20}$$

Where $*$ denotes the conjugate operation and the matrix J, an exchange matrix with dimension $(p_1 p_2)$x$(p_1 p_2)$ can be constructed as

$$J = \begin{bmatrix} 0 & \cdots & 0 & 1 \\ 0 & \ldots & 1 & 0 \\ \vdots & \ddots & \vdots & \vdots \\ 1 & 0 & \ldots & 0 \end{bmatrix} \tag{5.21}$$

Estimated autocorrelation matrix has the dimensions of $(p_1 p_2) \times (p_1 p_2)$. After the estimation of autocorrelation matrix, eigenvectors are divided into noise and signal subspaces. Since the radar echos involves K scatterer's exponential information inside the matrix there are $(p_1 p_2 - K)$ eigenvectors corresponding to noise subspace. Let's define the matrix $O_{p_1 p_2}$ as a $p_1 p_2 \times (p_1 p_2 - K)$ matrix, whose columns are the noise subspace eigenvectors of $\widehat{R_x}$ [6]. It is possible to find the K times nonzero eigenvalues of estimated autocorrelation matrix and take the other eigenvectors corresponding to zero eigenvalues.

Next step is to construct the column ordered vector approximation $\bar{a}(x, y)$ with a length of $p_1 p_2$. It can be defined as [6]

$$\bar{a}(x,y) = \begin{bmatrix} e^{-j\frac{4\pi}{c}({f_0}^x x + f_0^y y)} & e^{-j\frac{4\pi}{c}({f_1}^x x + f_0^y y)} & \dots \\ e^{-j\frac{4\pi}{c}({f_{p_1-1}}^x x_k + f_0^y y_k)} & e^{-j\frac{4\pi}{c}({f_0}^x x_k + f_1^y y_k)} & \dots \\ e^{-j\frac{4\pi}{c}\left({f_0}^x x_k + f_{p_2-1}^y y_k\right)} & \dots & e^{-j\frac{4\pi}{c}\left({f_{p_1-1}}^x x_k + f_{p_2-1}^y y_k\right)} \end{bmatrix}^T \tag{5.22}$$

Finally 2D-MUSIC formulation can be used to find the locations of scatterers.

$$P_{p_1p_2}(x,y) = \frac{\bar{a}(x,y)^H \bar{a}(x,y)}{\bar{a}(x,y)^H O_{p_1p_2} {O_{p_1p_2}}^H \bar{a}(x,y)} \tag{5.23}$$

In ISAR imaging, we calculate $P_{p_1p_2}(x,y)$ for each point (x,y) of chosen input grid and search the peaks of this function. Final spectrum gives the scatterer coordinates information at the peak locations. Much more detailed information about the theory of 2D-MUSIC radar imaging can be found in [6] and [29].

5.2.1 Simulations

Table 5.4: Locations of Scatterers in RD and 2D-MUSIC ISAR Simulation

Scatterer #	**1**	**2**	**3**	**4**	**5**	**6**	**7**	**8**
X	20	4	7	-10	10	-20	16	-16
Y	-4	10	10	0	20	10	-16	18

In this simulation target scatterers in Table 5.4 are used for image reconstruction. Output ISAR images of both algorithms are compared in Figure 5-10. Although conventional 2D-FFT method can not resolve the scatterers #2 and #3, 2D-MUSIC algorithm can extract the locations of these scatterers.

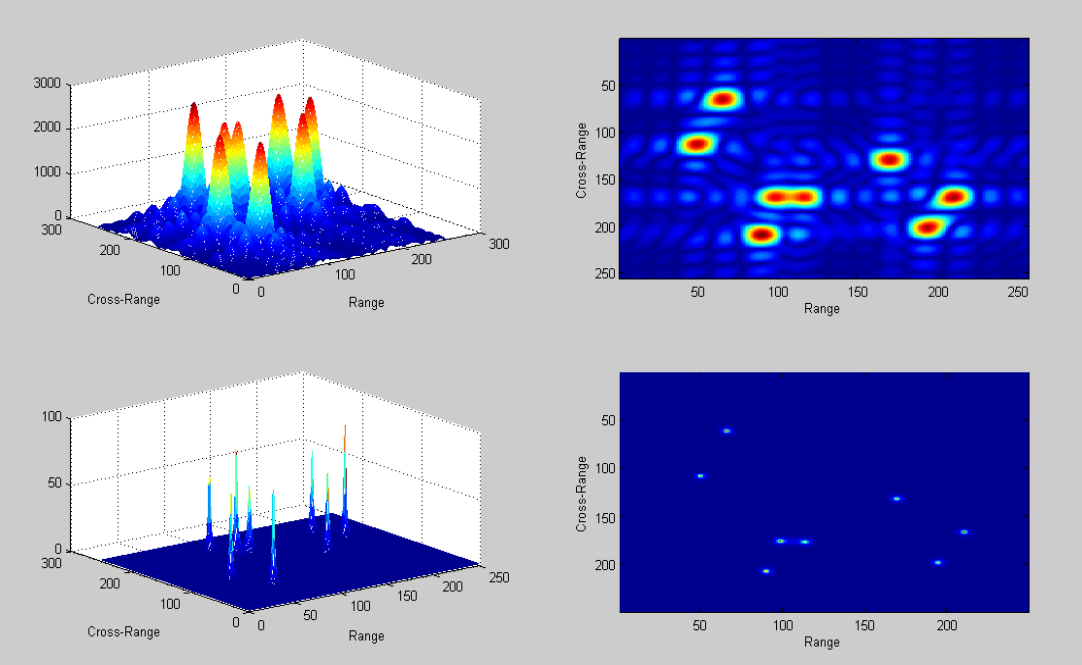

Figure 5-10: Comparison of Reconstructed Images Using 2D-FFT and 2D-MUSIC

5.3 Polar Reformatting

ISAR geometry generally uses narrow angular widths while collecting the returns from the target. Because small angle variations during the observation time provides major assumptions in image formation. Classical Fourier technique assumes that range bin of the target doesn't change between succesive pulses. When the total angle variation is small, direct Fourier transformation procedure can be efficiently employed in reconstructing the ISAR image.

Range-Doppler technique is not applicable in wide angle systems because the assumption of nearly rectangular window is not satisfied. Polar reformatting technique is applied to large-angle input data. Collecting received data over a large angular variation provides high resolution image formation.

Main procedure of polar reformatting is to make the input data in spatial domain suitable for fast Fourier transformation. FFT procedure can extract the ISAR image

only if input data locations in spatial frequency domain form a uniform rectangular grid. Polar reformatting algorithm transforms the polar domain into a rectangular domain.

The collection of radar input data samples represent a 2-dimensional, discrete time signal which requires interpolation onto uniform rectangular grid [1]. Then FFT operation can be applied to obtain the image of target. ISAR image processor divides polar reformatting into two seperate operations of range interpolation and angle interpolation. Therefore, only 1-dimensional filters are considered to resample the ISAR input data.

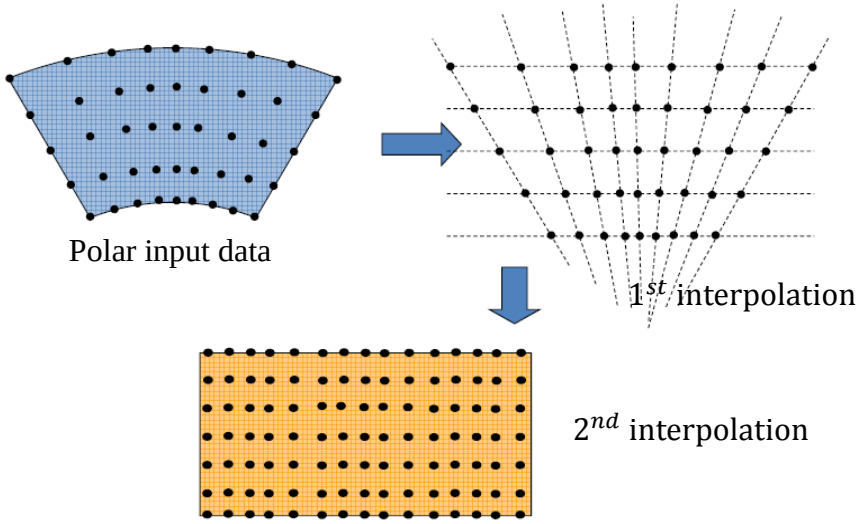

Figure 5-11: Steps of Polar-to-Rectangular Interpolation

Polar-to-rectangular interpolation has two steps of resampling procedures as shown in Figure 5-11.

Step 1: First interpolation is performed along the coordinate f. This step is to resample for uniform spacing in the frequency-space dimension along the central viewing angle. This type of interpolation is a resampling operation from uniform input locations to uniform output locations [1].

Step 2: Second interpolation is performed along the coordinate X. In this step the data along the discrete polar angles are resampled in the direction normal to the central viewing angle. This type of interpolation is a resampling operation from nonuniform input locations to uniform output locations [1].

There are some interpolation techniques to minimize the polar formatting errors. In the applications sinc reconstruction formula is used for resampling procedure. With this formula it is claimed that a continous time band-limited signal can be recovered from its discrete samples by convolving with a $sinc$ function [1]. Resampling expression is given by

$$x_c(t) = \sum_{k=-\infty}^{+\infty} x(k) sinc(\frac{t - kT}{T}) \tag{5.24}$$

In the applications of this thesis a limitation of summation exists since finite-length signals are used. Both interpolation operations use a number of left and rigth neighbours of desired output location.

While doing polar-to-rectangular conversion, value of output sample on the uniform locations is obtained from a sinc weigthed neighborhood of input samples [1]. In this algorithm, first, placing the input and output data samples on the spatial frequency plane must be done. Then interpolation is done step-by-step.

Discrete expression of range-angle interpolation is given by

$$\begin{aligned} y[n] = x_c\left(\frac{M}{L}T\right) &= \sum_{k=C-K}^{k=C+K} x[k] sinc(\frac{\frac{M}{L}T - kT}{T}) \\ &= \sum_{k=C-K}^{k=C+K} x[k] sinc(\frac{M}{L} - k) \end{aligned} \tag{5.25}$$

where C is the input center of the $sinc$ filter and K is the number of neigbours from the center. M/L ratio is directly related to output noninteger sample location. In this expression k will always be an integer value and $(\frac{M}{L} - k)$ will give a noninteger value which represents distance between the output and the neigbour input k

divided by distance between any two adjacent input samples. Center of $sinc$ filter is chosen as the floor of desired output location.

For example, for the finite signal $x[k]$ where $k = 1,2, \dots K$ the signal sample at non integer time instant $x[8.4]$ can be calculated by means of a sinc filter with a length of 6.

$$x[8.4] = x[6]sinc(8.4-6) + x[7]sinc(8.4-7) + x[8]sinc(8.4-8) + x[9]sinc(8.4-9) + x[10]sinc(8.4-10) + x[11]sinc(8.4-11) \quad (5.26)$$

As it is easily shown that center of $sinc$ filter is obtained as $floor(8.4) = 8$. Weigthing the neigbours of center with a $sinc$ function gives the desired output sample which locates at the noninteger value. Increasing the filter length gives more accurate results. But since the $sinc$ function is concentrated around the center there will be no need to use large values of filter length.

5.3.1 Resolution for Polar Reformatting

Since polar reformatting change the frequency sample locations, it also affects the cross-range resolution. Although cross-range resolution equation changes, range resolution remains constant. Because 1D interpolation in range dimension only scales the frequency locations and distance between succesive points in vertical dimension is still Δf which is the original step size. Then range resolution of new rectangular domain can be written as

$$\Delta r_p = \frac{c}{2M\Delta f_y} = \frac{c}{2B_y} = \frac{c}{2B} \quad (5.27)$$

Cross-range resolution can be calculated using the geometry of polar to rectangular transformation. Let Δf_x be the frequency steps on the horizontal axis which is obtained as

$$\Delta f_x = 2f_{M/2}\tan\left(\frac{\Delta\theta}{2}\right) \quad (5.28)$$

where $\Delta\theta$ is total angle variation and $f_{M/2}$ is the frequency sample in the middle. Then it can be expressed as a function of horizontal bandwidth B_x.

$$\Delta cr_p = \frac{c}{2M\Delta f_x} = \frac{c}{2B_x} = \frac{c}{4Mf_{M/2}\tan\left(\frac{\Delta\theta}{2}\right)} \tag{5.29}$$

5.3.2 Simulations

In the PR simulations, target model shown in Figure 5-5 is used. Three simulations are carried out with the simulation parameters given in Table 5.5, Table 5.6 and Table 5.7. The corresponding output images for simulation-1 and simulation-2 are presented in Figure 5-12 and Figure 5-13. Figure 5-14 shows the resolution improvement of Polar Reformatting algorithm for $\Delta\theta = 15°$.

Table 5.5: PR-ISAR Simulation-1 Parameters

Symbol	Name	Value
N	Number of Bursts	512
M	Number of Frequency Samples	500
f_c	Carrier Frequency	10 GHz
T	Pulse Repetition Interval	1 ms
B	Signal Bandwidth	400 MHz
Δf	Frequency Step Size	800 KHz
ω	Angular Velocity	0.171 rad/s
$\Delta\theta = \omega NT$	Total angle variation	5°

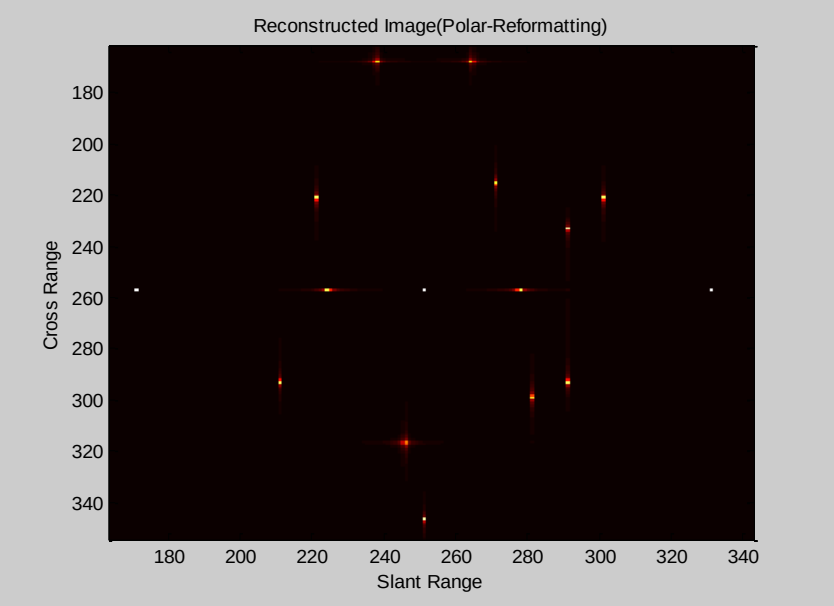

Figure 5-12: Polar Reformatting ISAR Image For $\Delta\theta = 5°$

Table 5.6: PR-ISAR Simulation-2 Parameters

Symbol	**Name**	**Value**
N	Number of Bursts	1024
M	Number of Frequency Samples	500
f_c	Carrier Frequency	10 GHz
T	Pulse Repetition Interval	1 ms
B	Signal Bandwidth	400 MHz
Δf	Frequency Step Size	800 KHz
ω	Angular Velocity	0.2047 rad/s
$\Delta\theta = \omega NT$	Total angle variation	12°

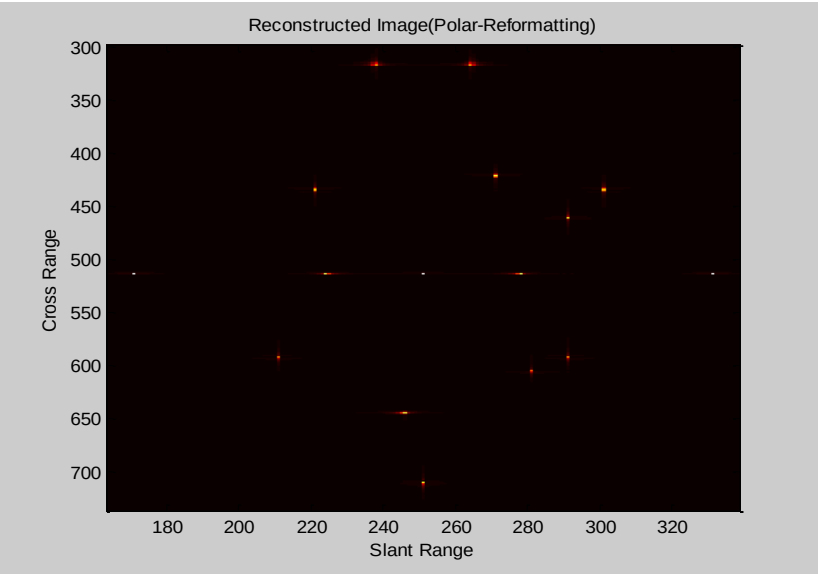

Figure 5-13: Polar Reformatting ISAR Image For $\Delta\theta = 12°$

Table 5.7: PR and RD ISAR Simulation-3 Parameters

Symbol	**Name**	**Value**
N	Number of Bursts	800
M	Number of Frequency Samples	500
f_c	Carrier Frequency	10 GHz
T	Pulse Repetition Interval	1 ms
B	Signal Bandwidth	400 MHz
Δf	Frequency Step Size	800 KHz
ω	Angular Velocity	0.3277 rad/s
$\Delta\theta = \omega NT$	Total angle variation	15°

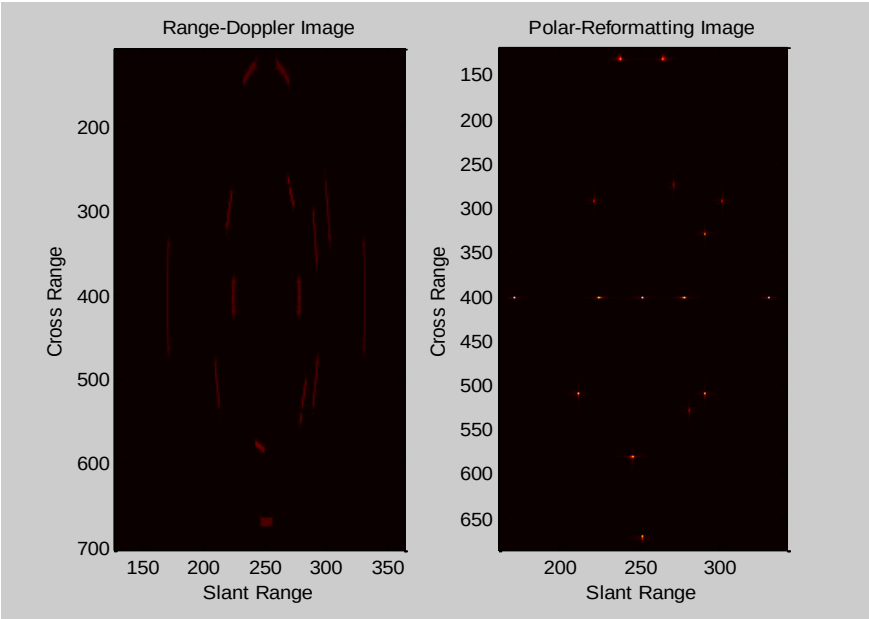

Figure 5-14: Resolution Improvement of Polar Reformatting for $\Delta\theta = 15°$

5.4 Back Filtered Projection

The analytical formulation of the medical problem and the reconstruction of the ISAR images are similar. So ISAR can be thougth as an application of computer tomography.

Tomographic approach reconstructs the images from object's projections. These projections are obtained at the increments of the viewing angle of target. Tomography provides a different property that is the reconstruction of two dimensional images by using one dimensional projections from a series of angles.

Tomographic approach can be applied to the radar systems if range and cross-range returns of target are defined as the projections. ISAR geometry has angular diversity so that tomogrhapic technique can be used for target image reconstruction. By using the rotation of target object, a sufficient 1-dimensional data can be collected to reconstruct 2-dimensional image.

5.4.1 Projection Slice Theorem

Projection slice theorem states that each piece of projection data at some angle is the same as the Fourier transform of the multidimensional object at that angle. In other words taking 1D Fourier transform of projection at a viewing angle is equivalent to the taking 2D Fourier transform and getting the slice of 2D plane at that angle.

Assuming a signal $\xi(\mathrm{x},\mathrm{y})$ and an orientation angle of ϑ. Projection function along the angle can be written as

$$p_{\vartheta}(r) = \iint \xi(x,y)\delta(x\cos\vartheta + y\sin\vartheta - r)dxdy \tag{5.30}$$

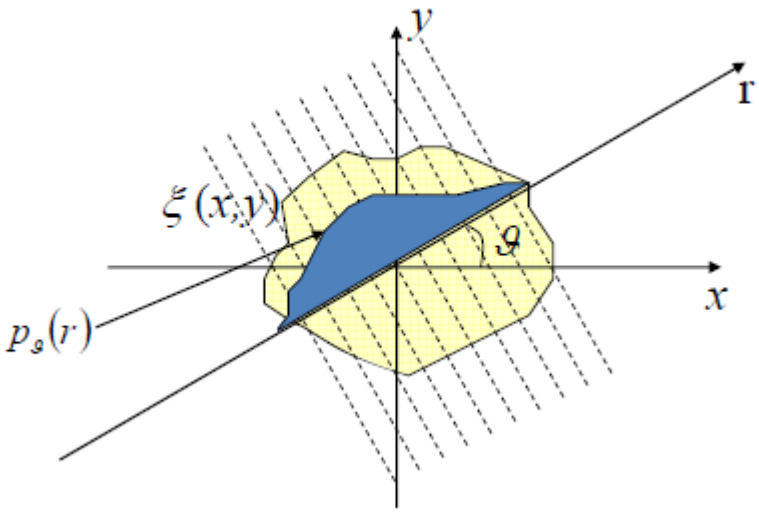

Figure 5-15: Projection Function of Signal Along the Angle ϑ

A projection corresponding to the angle ϑ is a line integral formulation and a 1D function of the single variable r. For each angle ϑ there is a unique projection function of variable r. An example of projection function is presented in Figure 5-15.

ISAR systems collect k target projections, relative to k different aspect angles and try to reconstruct the target reflectivity function.

Fourier representation of the projection function can be directly written as

$$P_\vartheta(R) = \int_{-\infty}^{+\infty} p_\vartheta(r) e^{-j2\pi Rr} dr$$

$$= \int_r \int_x \int_y \xi(x,y)\, \delta(x\cos\vartheta + y\sin\vartheta - r) dx dy e^{-j2\pi Rr} dr$$

$$= \int_x \int_y \xi(x,y) e^{-j2\pi(x\cos\vartheta + y\sin\vartheta)R} dx dy = \Theta(X,Y)\big|_{\substack{X=R\cos\vartheta \\ Y=R\sin\vartheta}}$$

(5.31)

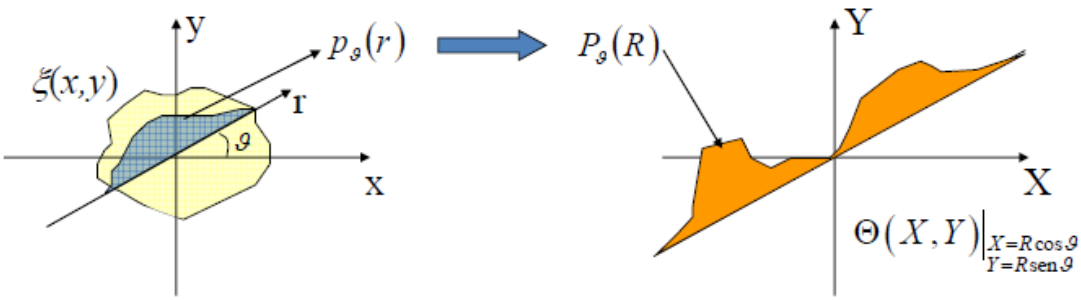

Figure 5-16: Fourier Domain Representation of Projection Function

From Figure 5-16 phsyical meaning of the projection slice theorem can be seen. Fourier transform of the projection at the angle ϑ is a slice of 2-dimensional Fourier transform of $\xi(x,y)$ oriented at the same angle [27]. Then by taking Fourier transforms of N projections, Fourier domain of target reflectivity function can be constructed.

5.4.2 Image Reconstruction with Back Projection

The relationships between Fourier transform and cartesian to polar coordinate transformation can be summarized in four equations.

$$\xi(x,y) = \iint \Theta(X,Y) e^{j2\pi(xX+yY)} dXdY \qquad \Theta_P(R,\Phi)|_{\Phi=\vartheta} = P_\vartheta(R)$$
$$\xi_p(r) = \iint \Theta_P(R,\Phi) e^{j2\pi Rrcos(\Phi-\varphi)} RdRd\,\Phi \qquad \Theta_P(R,\Phi+\pi)|_{\Phi=\vartheta} = P_\vartheta(-R) \tag{5.32}$$

By using these relationships target reflectivity function can be defined in polar coordinates and reconverted.

$$\xi(x,y) = \xi_p(r,\varphi)|_{\substack{r=\sqrt{x^2+y^2} \\ \varphi=arctan(y/x)}} = \int_0^{\infty}\int_0^{2\pi} R\Theta_P(R,\Phi)\, e^{j2\pi R(xcos\Phi+ysin\Phi)} dRd\Phi$$

$$\xi(x,y) = \int_0^{\pi}\int_{-\infty}^{+\infty} |R|\,\{P_\vartheta(R)\}_{\vartheta=\Phi} e^{j2\pi R(xcos\Phi+ysin\Phi)} dRd\Phi \tag{5.33}$$

Expression is the inverse Fourier transform of product of two functions calculated at $xcos\Phi + ysin\Phi$. Then one can write the definition in terms of Fourier transformation.

$$\xi(x,y) = \int_0^{\pi} \left[FT^{-1}\{|R|\{P_\vartheta(R)\}_{\vartheta=\Phi}\}_{xcos\Phi+ysin\Phi}\right] d\Phi \tag{5.34}$$

The component in the integral is equivalent to the convolution of projection function evaluated at $xcos\Phi + ysin\Phi$ with $FT^{-1}\{|R|\}$.

$$\left[FT^{-1}\{|R|\{P_\vartheta(R)\}_{\vartheta=\Phi}\}_{xcos\Phi+ysin\Phi}\right] = FT^{-1}\{|R|\} \otimes p_\Phi(x\cos\Phi + y\sin\Phi) \tag{5.35}$$

Let $q_{\vartheta=\Phi}(x\cos\Phi + y\sin\Phi)$ be the filtered back projection term. Then desired target reflectivity function $\xi(x,y)$ can be reconstructed from its projections. This property can be expressed as

$$\xi(x,y) = \int_0^{\pi} q_{\vartheta=\Phi}(x\cos\Phi + y\sin\Phi) d\,\Phi \tag{5.36}$$

In real applications, number of projection angles is limited and by replacing the integral with a discrete summation, implementation can be done as in Equation (5.37)

$$\hat{\xi}(x,y) = \sum_{i=1}^{N} q_{\vartheta_i}(x\cos\vartheta_i + y\sin\vartheta_i) \tag{5.37}$$

where $\hat{\xi}(x,y)$ is the estimation of reconstructed target reflectivity function and N is the number of available projection angles. Steps of filtered-back projection algorithm can be summarized in Figure 5-17.

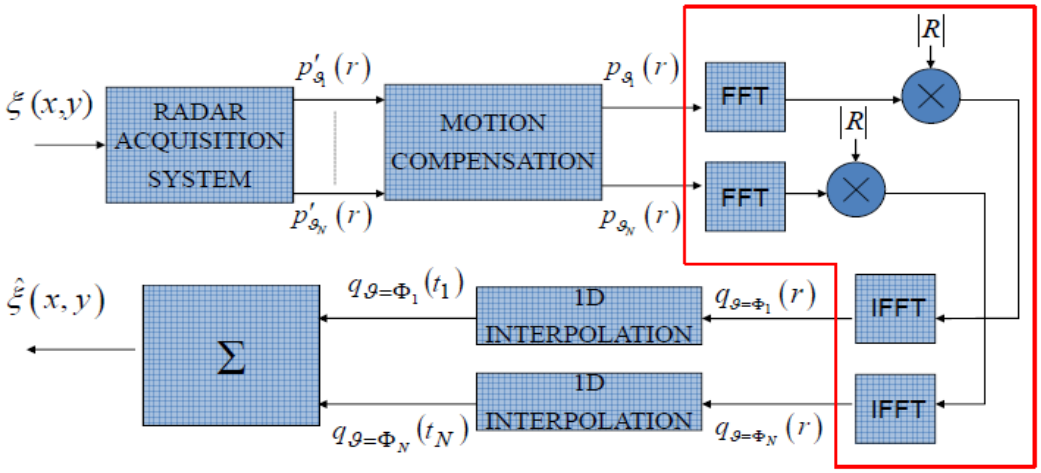

Figure 5-17: Filtered-Back Projection Algorithm

ISAR systems can obtain projections in the form of range profiles of the target scatterers [26]. Projections in ISAR applications can be thougth as target returns from different aspect angles. In the applications, synthetic imaging is used and the measurements of projections are taken in Fourier domain [26]. The word of *filtered* in the algorithm name comes from the $|R|$ component in the main equation. Production of Fourier samples with frequencies is equivalent to a highpass filtering operation. This filtering term is the result of cartesian-to-polar coordinate transformation.

Back-projection algorithm can be applied to ISAR problem in two ways:

5.4.3 IFFT Approach

For ISAR back-projection application to become faster, IFFT is applied to each row of the input data matrix. This transformation doesn't interpolate the scatterer point into the exact frequency location since it gives results at discrete samples. For each aspect angle sample n, ith the scatterer has a range of $r_{in} = x_i \sin\theta_n + y_i \cos\theta_n$. After applying IFFT operation, peak which is related to r_{in} can be obtained.
Assuming a grid in which we will search the reflectivities of points is constructed, algorithm steps become as follows:
Step 1: Apply 1D IFFT to each row of the input matrix.

$$q_n = IFFT(row_n) \tag{5.38}$$

Step 2: For ith scatterer in the grid, calculate the $r_{in} = x_i \sin\theta_n + \cos\theta_n$ and find the corresponding sample index s_{in} on the IFFT output rows for $n = 1, 2, \ldots N$ where N is the number of angle samples.

$$s_{in} = round\left(\frac{r_{in} + \frac{c}{2\Delta f}}{\frac{c}{2B}} + 1\right) \tag{5.39}$$

Step 3: Integrate every IFFT output value at the index s_{in} to get the reflectivity of scatterer.

$$g(x_i, y_i) = \sum_{n=1}^{N} q_n(s_{in}) \tag{5.40}$$

Step 4: Repeat the steps 2 and 3 for all points in the grid and construct the final ISAR image.

5.4.3.1 Simulations

In the simulations, target model shown in Figure 5-18 is used.

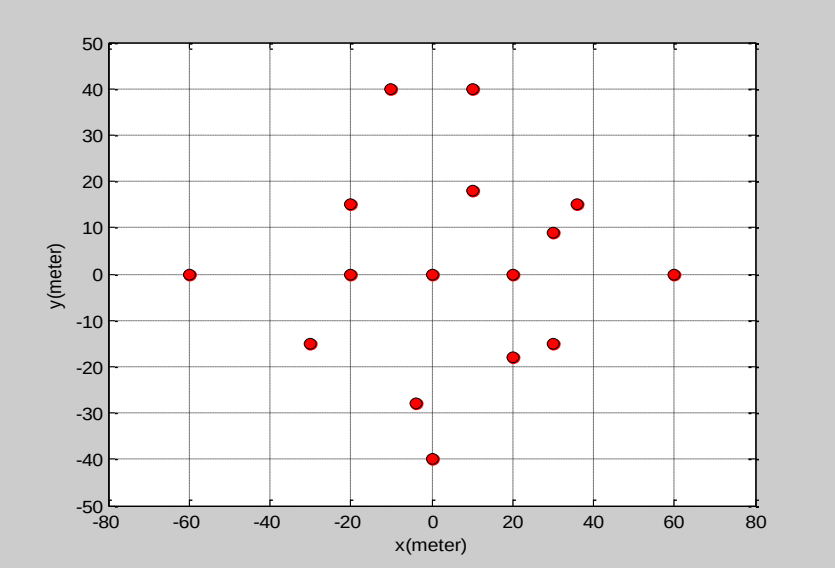

Figure 5-18: Target Model for IFFT Based BP Simulations

Table 5.8: IFFT Based BP ISAR Simulation Parameters

Symbol	**Name**	**Value**
N	Number of Bursts	800
M	Number of Frequency Samples	800
f_c	Carrier Frequency	10 GHz
B	Signal Bandwidth	400 MHz
Δf	Frequency Step Size	800 KHz

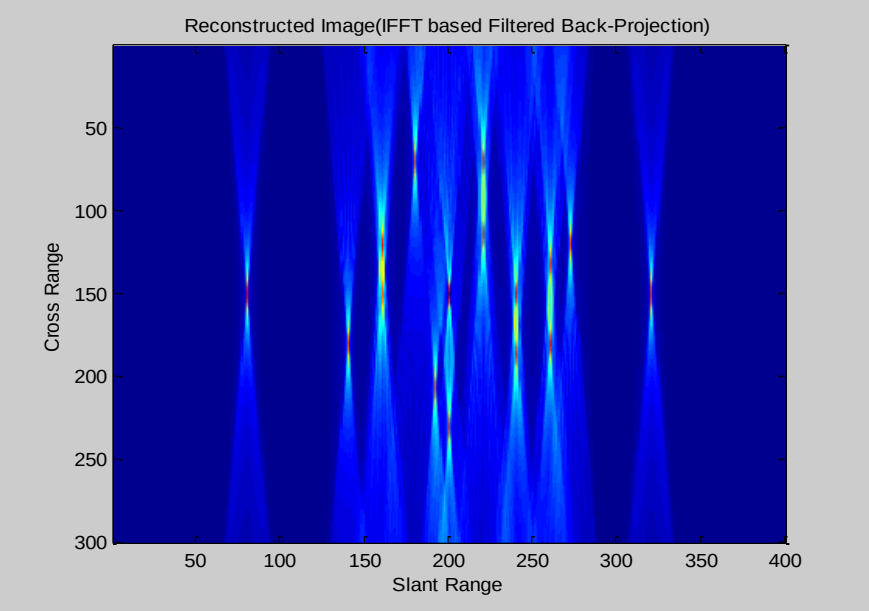

Figure 5-19: IFFT based Back-Projection ISAR Image $\Delta\theta = 10°$

Figure 5-19 is an example of small angle variation. Simulation parameters are given in Table 5.8. As it is observed that, cross-ranges of scatterers can not be resolved perfectly. After the 1D-IFFT we find an IFFT index that corresponds to the range bins of the scatterers for every angle variation. If the angle variation is small then sample index that is found is not a well-interpolated one. Especially the scatterers that have same y_i can not be resolved. Because $r_{in} = x_i \sin\theta_n + y_i \cos\theta_n \approx y_i$ for small θ and they are mapped onto the same IFFT output bin. So that it becomes difficult to get x_i (cross-range information). Figure shows that small angular changes cause the cross-range information to be lost. This result can be thougth as an example of straddle loss.

Figure 5-20 and Figure 5-21 show that increasing total angle variation improves the performance of IFFT based back-projection algorithm. When the aspect angle becomes larger, much more cross-range information can be extracted. Because the scatterers that have same range and different cross range, moves to resolvable frequency locations s_{in} at the IFFT output.

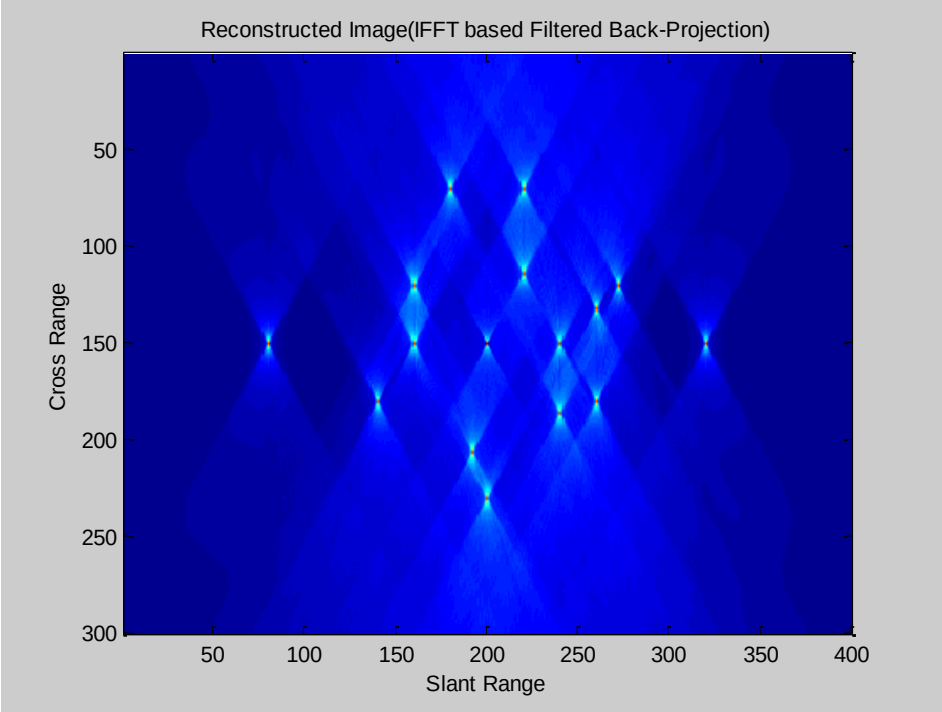

Figure 5-20: IFFT based Back-Projection ISAR Image $\Delta\theta = 60°$

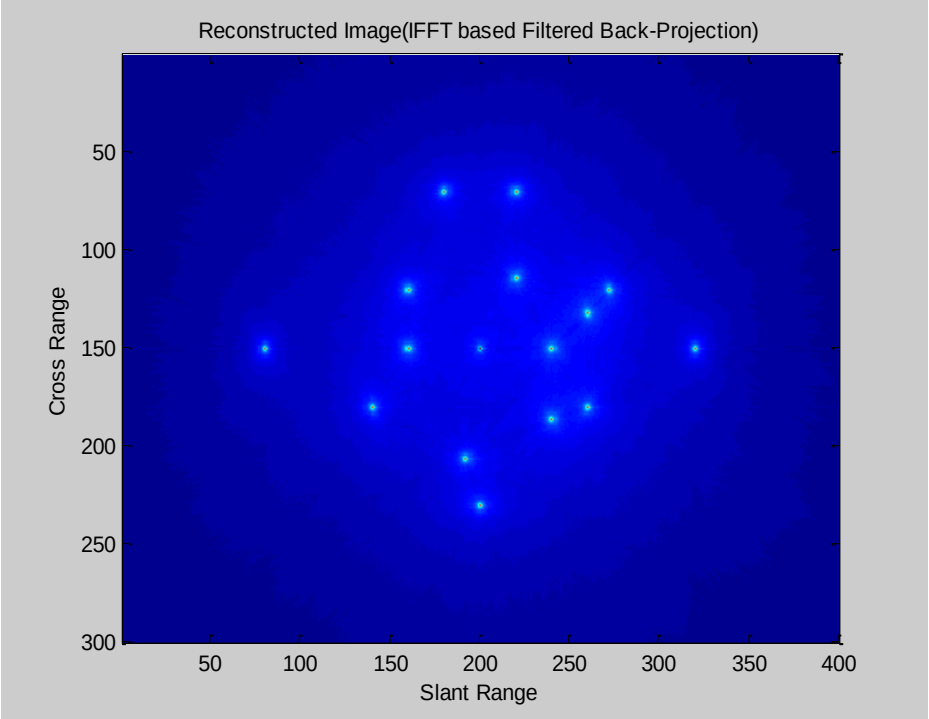

Figure 5-21: IFFT based Back-Projection ISAR Image $\Delta\theta = 180°$

5.4.4 DTFT Approach

This algorithm is the projection of all data samples onto one scatterer point that we want to know. By using this formula exactly we can find all reflectivies in our image plane. It takes too long time to take the result. Since it includes all FFT and interpolation operations gives more accurate images compared to the IFFT approach. Algorithm calculates the Discrete Time Frequency Transform (DTFT) at the frequency sample that is directly related to scatterer range at the θ_n and integrate them to find the reflectivity $g(x_i, y_i)$

$$g(x_i, y_i) = \sum_{n=1}^{N} \sum_{m=1}^{M} S(f_m, \theta_n) |f_m| exp\left(-j4\pi f_m (x_i \sin\theta_n + y_i \cos\theta_n)/_c \right) \tag{5.41}$$

To implement Equation (5.41) one can follow a similar procedure as simulator design. Algorithm steps are given by:

Step 1: Construct a 2D matrix for i th point of grid as if it is an input data matrix which involves only i th point with unit reflectivity.

Step 2: Apply elementwise multiplication between the input data matrix and the matrix found in step 1.

Step 3: Get the summation of each element in final matrix to find the back-projection of input matrix onto i th point in grid.

If the scanning points in grid have desired locations, two matrices we multiplicate match since the exponential information of that point is involved in the input matrix. So that the points that we want to find give peaks in the output spectrum.

5.4.4.1 Simulations

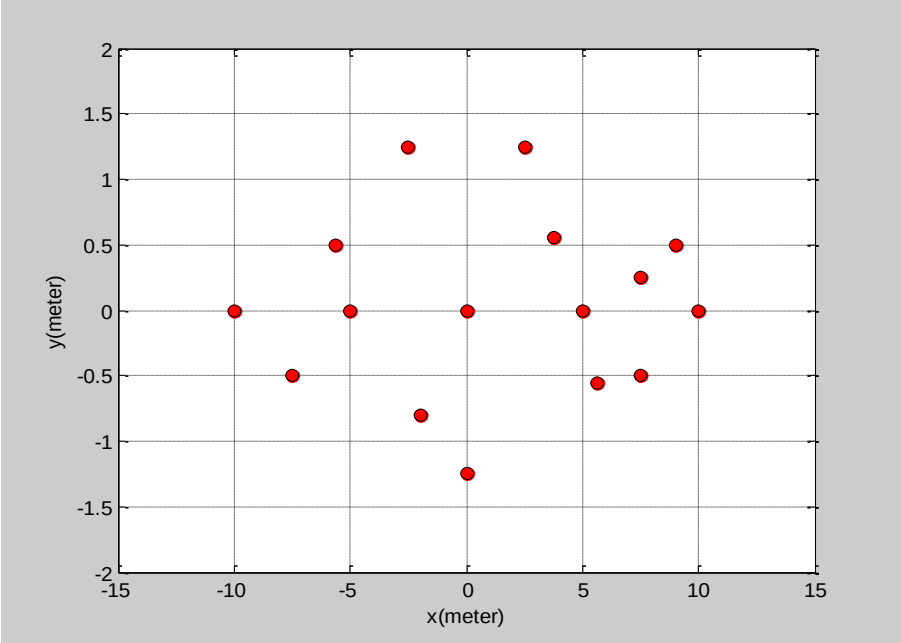

Figure 5-22: Target Model for DFT Based BP

Two simulations are carried out with the parameters given in Table 5.9. Target model which is used in these simulations is shown in Figure 5-22.

Table 5.9: DFT Based BP ISAR Simulation Parameters

Symbol	Name	Value	
		Simulation1	**Simulation2**
N	Number of Bursts	256	512
M	Number of Frequency Samples	256	256
f_c	Carrier Frequency	10 GHz	10 GHz
B	Signal Bandwidth	400 MHz	400 MHz
Δf	Frequency Step Size	1.563 MHz	1.563 MHz

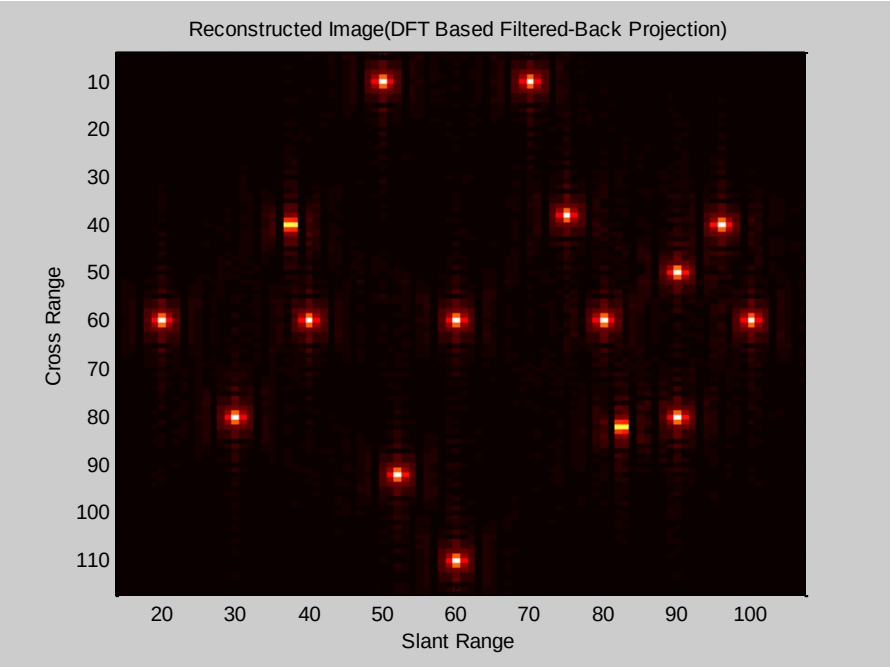

Figure 5-23: DFT based Back-Projection ISAR Image $\Delta\theta = 20°$

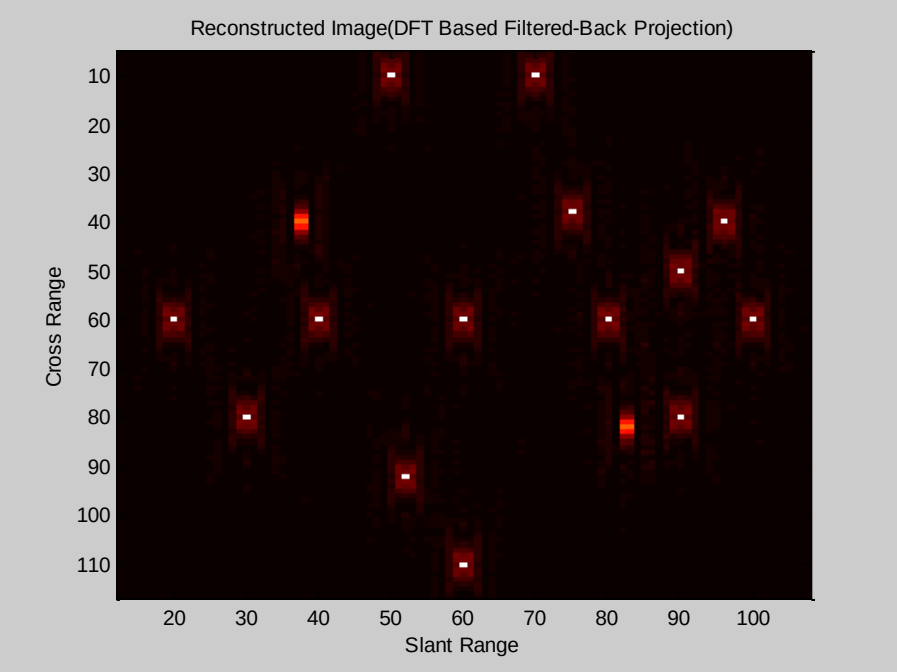

Figure 5-24: DFT based Back-Projection ISAR Image $\Delta\theta = 40°$

Figure 5-23 and Figure 5-24 are the examples of reconstruction of ISAR image from its projections for small data set. In the second simulation, since observation angle is chosen as larger, image formation can be done by using more angle projections. Increasing the number of angle samples improves ISAR image quality. On the other hand, DFT based reconstructed images with high computational load obviously seem to be cleaner than FFT based ones, since interpolation errors are minimized.

5.5 Joint Time-Frequency Techniques

ISAR image processing is one of the most popular application areas of joint-time frequency analysis. Since rotating targets have time-varying Doppler shifts, time-frequency analysing methods are useful to reconstruct the ISAR images.

ISAR system requires a large signal bandwidth and long image frame to get a high resolution image. However, time-varying frequency behavior of received signal and multiple scatterring mechanism of target can degrade the image quality. The classical aproach uses FFT processing to obtain Doppler frequency of scatterers. But Fourier transform can detect only stationary Doppler changes during the observation time. Many algorithms have been developed to overcome image blurring problem. Most of them tries to compensate target's complex motion.

Joint-time frequency techniques give a high resolution radar image without applying motion-compensation algorithms [2]. The purpose of this section, is to show the application of JTFA to ISAR cross-range image. Joint-time frequency techniques will remove the restrictions of conventional methods and estimate Doppler information by tracking time frames.

In our applications the most important parameter for time-fequency analysis is the time varying rotational Doppler frequency. Different cross-range locations of scatterers creates multiple time-varying Doppler frequencies. ISAR time-frequency techniques tries to overcome multiple time-varying Doppler frequency problem.

STFT as a linear transform and WVD as a bilinear transform will be investigated with the applications.

5.5.1 Time-Frequency Based Image Formation

As it is known that Fourier based range-Doppler imaging techniques generate one image from a $M \times N$ data set [30]. It means that there are M range profiles which has N time histories. Time-frequency based techniques take time-frequency transform of each slow-time series and generates $N \times N$ data corresponding to one range bin. Collecting these 2D data set for M range bins, $N \times M \times N$ 3D time-range-Doppler data is created. Time-frequency operation can be expressed as [30]:

$$Q(r_m, f_n, t_n) = TF\{G\{r_m(n)\}\} \tag{5.42}$$

At a time instant t_n we can extract one range-Doppler image frame from total data set. $Q(r_m, f_n, t_n = t_i)$ Analysing 2D range-Doppler images at all time instants shows the time history. So that temporal change properties from one time to another can be seen. Each individual time-sampled frame provides a clear image with high resolution [30].

Basically, when Fourier transform is replaced with time-frequency transform, data set extends to a 3D cube. Motion compensation procedure is not considered. Summation of images at all time instants gives the same result as conventional Fourier based approach.

$$I(r_m, f_n) = \sum_{t_n=t_0}^{t_{N-1}} Q(r_m, f_n, t_n) \tag{5.43}$$

To see the time dependent Doppler changes it is not necessary to look at all time samples. Since the Doppler changes between succesive time instants is not significant, choosing specific time instants in time history may be enough. Figure 5-25 shows the steps of time-frequency based image formation algorithm.

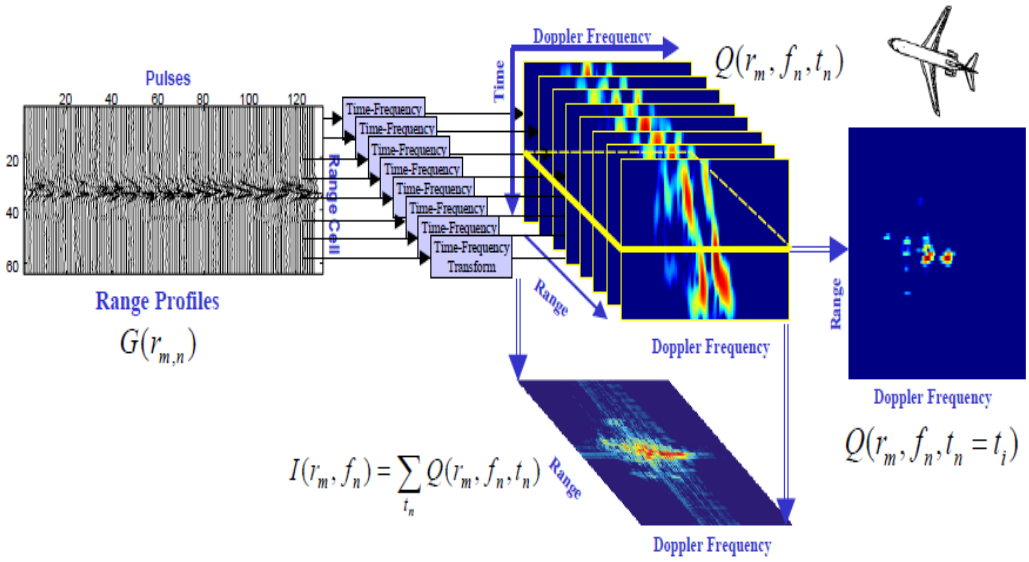

Figure 5-25: Time-Frequency Based Image Formation Algorithm Steps [30]

5.5.2 Short-Time Fourier Transform

Conventional Fourier transform projects the input signal onto sinusoidal basis functions**.** Since these basis functions are not concentrated in time domain, Fourier transform does not resolve time dependent frequency changes.

General way of analysing time-frequency properties of signal simultaneously is to project the signal onto time-frequency concentrated basis functions. Frequency modulated Gaussian functions are one of the examples. In other words comparing the signal with these types of functions gives the signal's local time-frequency characteristics.

Clasical Fourier transform is a general expression and can not establish a point-to-point relationship between time-frequency domains. To overcome this problem, it is an easy way to apply an inner product which is named as short-time frequency transform, ($STFT$), given by

$$STFT(t,w) = \int s(\tau)\,\gamma_{t,w}{}^{*}(\tau)d\tau = \int s(\tau)\gamma^{*}(\tau - t)e^{-jw\tau}d\tau \qquad (5.44)$$

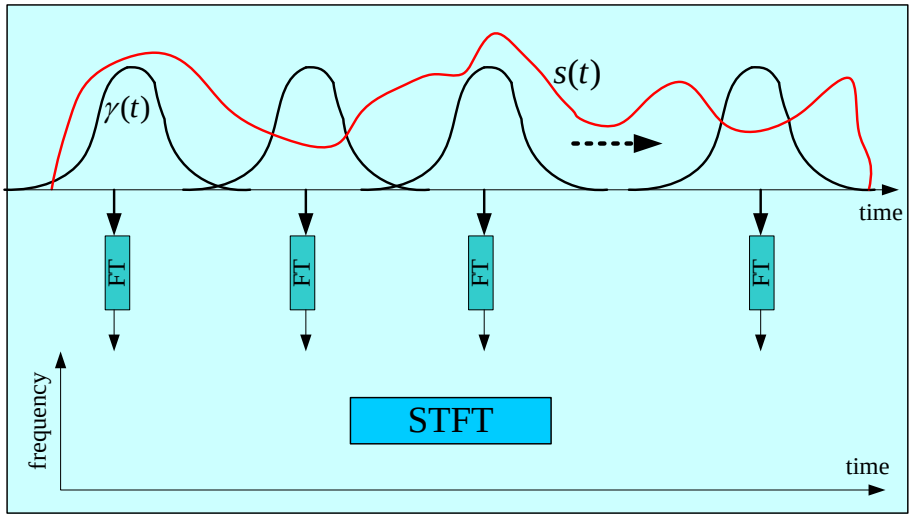

Figure 5-26: Sliding Windows and Short Time Fourier Transforms [2]

Where $\gamma(t)$ is the window function and since there is a short-time windowing operation formula is also called as windowed Fourier transform. STFT is visualized in Figure 5-26.

Local time images can be constructed by using STFT as in the following steps:

Step 1: Choose a window length and construct a time window function.

Step 2: Shift the window function by a time delay and find the multiplication of input signal with time shifted window function.

Step 3: Take the Fourier transform of resulting signal and see the local frequency behavior corresponding to that time delay.

To convert the continuos time signal into discrete time domain time sampling should be done. The practical applications use the discrete expression of short–time frequency transform:

$$STFT[k,n] = \sum_{i=0}^{L-1} s[i]\gamma[i-k]W^{-ni}{}_{L} \tag{5.45}$$

where

$$STFT[k,n] = STFT(t,w)|_{t=k\Delta t,\ \ w=2\pi n/(L\Delta t)} \tag{5.46}$$

The square of the STFT is called as STFT spectrogram and it represents signal's energy distribution in time-frequency plane [2].

5.5.2.1 Simulations

In the simulations, target model shown in Figure 5-5 is used. Simulation parameters are given in Table 5.10 and the output image frames 1, 4 and 8 are presented in Figure 5-27, Figure 5-28 and Figure 5-29 respectively.

Table 5.10: STFT ISAR Simulation Parameters

Symbol	Name	Value
N	Number of Bursts	800
M	Number of Frequency Samples	256
f_c	Carrier Frequency	10 GHz
T	Pulse Repetition Interval	1 ms
B	Signal Bandwidth	400 MHz
Δf	Frequency Step Size	1.56 MHz
ω	Angular Velocity	0.3277 rad/s
L	Window Length	100
$\Delta\theta = \omega NT$	Total angle variation	15°

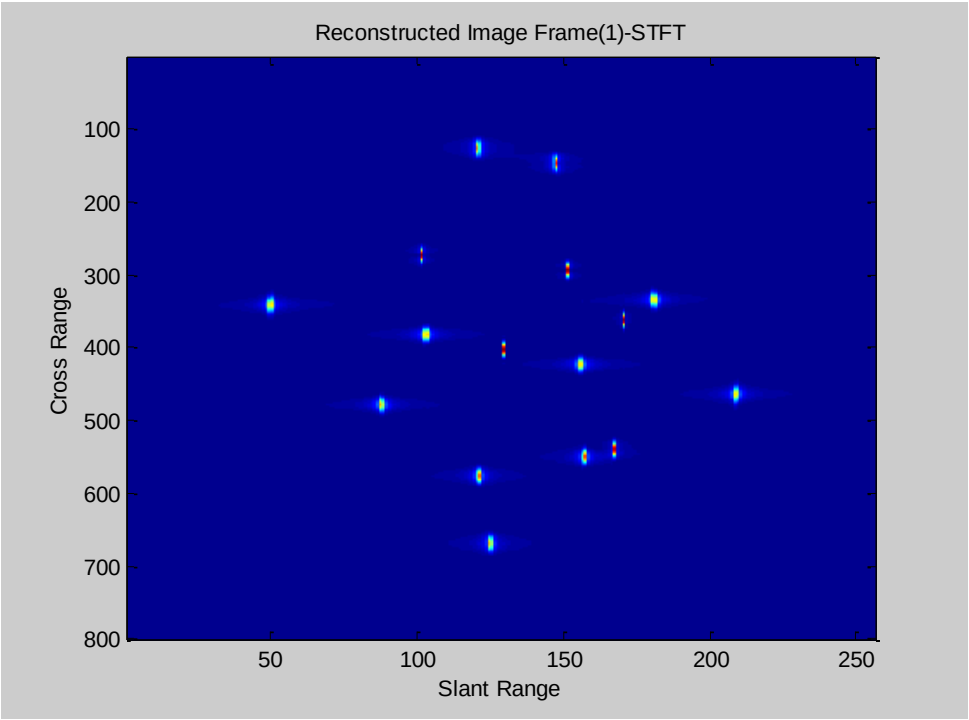

Figure 5-27: STFT ISAR Image Frame 1

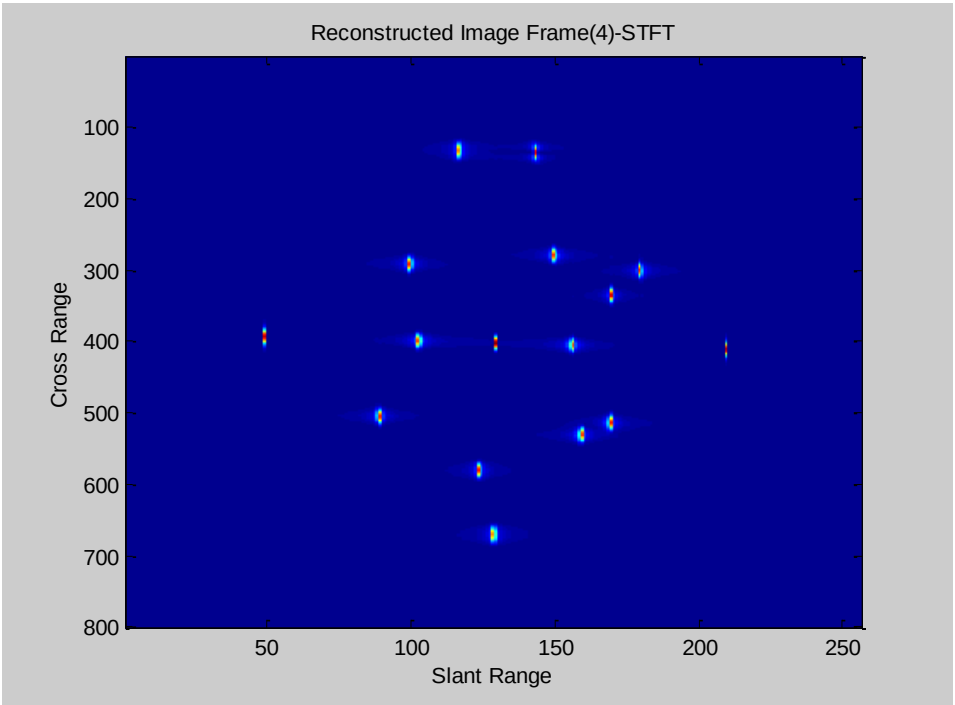

Figure 5-28: STFT ISAR Image Frame 4

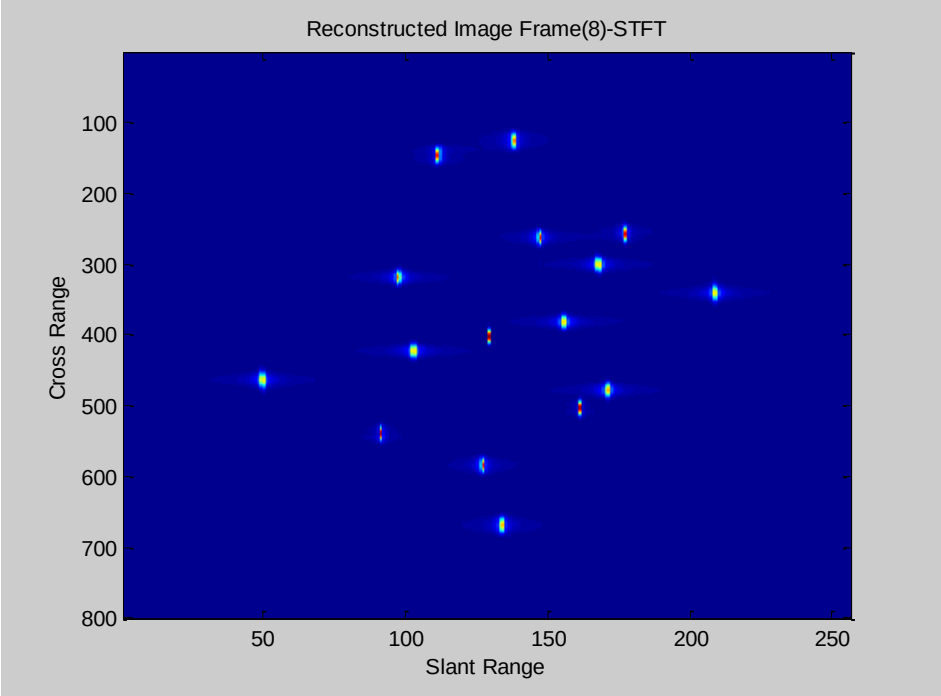

Figure 5-29: STFT ISAR Image Frame 8

5.5.3 Wigner-Wille Distribution

This approach is based on the use of time dependent autocorrelation function for calculating the power spectrum. Standart autocorrelation is only a function of time lag τ. The Wigner-Ville uses a time varying autocorrelation function. To choose a suitable autocorrelation function, properties of time-dependent spectrum should be considered. For example, at a specific frequency, summation of instantenous time spectrum should yield the total power spectrum, i.e.,

$$\int P(t,w)dt = |S(w)|^2 \tag{5.47}$$

Similarly, energy at a time instant should be equal to the integration along frequency axis [2].

$$\frac{1}{2\pi}\int P(t,w)dw = |s(t)|^2 \tag{5.48}$$

Then we can define time-dependent autocorrelation function as

$$R(t,\tau) = s(t+\tau/2)s^*(t-\tau/2) \tag{5.49}$$

Time-dependent power spectrum can be expressed as the Fourier transform of time dependent autocorrelation function.

$$P(t,w) = \int R(t,\tau)\, e^{-jw\tau}d\tau \tag{5.50}$$

Then Wigner-Ville Distribution can be expressed as

$$WVD_s(t,w) = \int s(t+\tau/2)s^*(t-\tau/2)e^{-jw\tau}d\tau \tag{5.51}$$

or equivalently it can be written as

$$WVD_s(t,w) = \int S(w+\theta/2)S^*(w-\theta/2)\, e^{j\theta t}d\theta \tag{5.52}$$

There are many reasons for choosing this method to reconstruct ISAR images. Wigner-Ville distribution provides high frequency and time resolution. Especially, cross range chirp signals can be identified easily by using this transform [31]. From Equation (5.48)-(5.52) it is observed that WVD satisfies time-frequency marginals. Time derivative of phase can be found to detect the instantenous frequencies of signals.

Compared to STFT, WVD doesn't use any window functions. Basically, WVD is obtained by comparing information of the signal with its own information at other times and frequencies.WVD possesses several interesting properties which we will not get into the details. They are named as, Time-Shift Invariant, Frequency Modulation Invariant, Time Marginal Condition, Frequency Marginal Condition [2]. Maybe the most important property of WVD can be selected as Instantaneous Frequency Property [2]. In the chapter 3, this frequency estimation ability of WVD

is used to estimate the rotational velocity of the scatterers. Let $s(t) = a(t)e^{j\emptyset(t)}$ be an arbitrary phase modulated signal. Then, derivative of the signal's phase is

$$\emptyset'(t) = \frac{\frac{1}{2\pi}\int \omega WVD_s(t,\omega)d\,\omega}{\frac{1}{2\pi}\int WVD_s(t,\omega)d\,\omega} = \frac{\frac{1}{2\pi}\int \omega WVD_s(t,\omega)d\,\omega}{|a(t)|^2} = \langle\omega\rangle_t \qquad (5.53)$$

From Equation (5.53) it can be concluded that frequency at any time instant can be obtained by taking average of frequencies over time axis of WVD plane. Instantenous frequency information of WVD is useful to detect unknown components of cross-range signals of ISAR.

Although the WVD has many advantages, its main problem is called as cross-term interference which is the result of multiple signals. Simply, cross-term interference can be shown in the case of two signals. Assuming that $s(t) = s_1(t) + s_2(t)$, then the WVD can be expressed as

$$WVD_s(t,w) = WVD_{s_1}(t,w) + WVD_{s_2}(t,w) + 2Re\{WVD_{s_1s_2}(t,w)\} \qquad (5.54)$$

where

$$WVD_{s_1s_2}(t,w) = \int s_1(t+\tau/2)s_2{}^*(t-\tau/2)e^{-jw\tau}d\tau \qquad (5.55)$$

is called as cross-WVD. As a result, if the signal contains multiple subsignals, its WVD contains cross terms that occur halfway between the pairs of auto terms [14]. Even if WVD has good frequency-time resolution, unwanted oscilatory cross terms can disturb time-frequency analysis. For the ISAR application of this thesis, cross-term interference is seen when one range bin includes multiple cross-range scatterers. Since WVD is not a linear operator, sum of mutiple scatterer returns in one range bin creates interference peaks on the resulting images. Amplitude of the cross terms can be higher than the original signal terms and this is an unwanted situation. From the simulations of WVD based ISAR images, cross-term

interference can be easily seen between the points that have same slant-range locations.

In the applications, discrete versions of WVD formulations are constructed first. In order to find a discrete WVD, sampling rate of the signal has to be doubled. As we know that, to apply an interpolation filter, first we insert zeros between each sample and then we apply low-pass filter to complete smoothing operation between points. After interpolation operation, limits of the discrete signal have to be choosen also. Because continous time formulation requires an infinite summation and that is not the real case.

Let's define a rectangular window function $w(n)$ with a length of $4L + 1$.

$$w(n) = \begin{cases} 1 & |n| < 2L \\ 0 & otherwise \end{cases} \tag{5.56}$$

And discrete formulation of WVD becomes

$$WVD_s[m,\theta) = 2\sum_{n=-\infty}^{+\infty} w[n]y[m+n]y^*[m-n]\mathrm{e}^{-\mathrm{j}2\theta\mathrm{n}} \tag{5.57}$$

Where $\theta = w\Delta t/2$ denotes normalized frequency. The previous steps of this formulation can be found at [2].

Since the window function limits the summation equation is written as [2]

$$WVD_s[m,\theta) = 2\sum_{n=-(2L-1)}^{2L-1} y[m+n]y^*[m-n]\mathrm{e}^{-\mathrm{j}2\theta\mathrm{n}} \tag{5.58}$$

By using the symetric property of $y[m+n]y^*[m-n]$ it can be redefined as

$$\begin{aligned} &= 2\sum_{n=-(2L-1)}^{0} y[m+n]y^*[m-n]\mathrm{e}^{-\mathrm{j}2\theta\mathrm{n}} \\ &\quad + 2\sum_{n=0}^{2L-1} y[m+n]y^*[m-n]\mathrm{e}^{-\mathrm{j}2\theta\mathrm{n}} - 2y[m]y^*[m] \\ &= 4Re\left\{\sum_{n=0}^{2L-1} y[m+n]y^*[m-n]\mathrm{e}^{-\mathrm{j}2\theta\mathrm{n}}\right\} - 2y[m]y^*[m] \end{aligned} \tag{5.59}$$

If the frequency θ is replaced with its digital expression, then the discrete WVD formula can be constructed as

$$DWVD_s[m,k] = 4Re\left\{\sum_{n=0}^{2L-1} y[m+n]y^*[m-n]\mathrm{e}^{-\mathrm{j}2\pi\mathrm{kn/L}}\right\} - 2y[m]y^*[m] \tag{5.60}$$

Equation (5.60) represents $2L$-point FFT. But since half of the inputs are zero, there is no need to do $2L$-point FFT operation. Assuming that

$y[m+n]y^*[m-n] = 0$ for $|n| > L$, equation can be expressed as a L-point FFT

$$DWVD_s[m,k] = 4Re\left\{\sum_{n=0}^{L-1} y[m+n]y^*[m-n]\mathrm{e}^{-\mathrm{j}2\pi\mathrm{kn/L}}\right\} - 2y[m]y^*[m] \tag{5.61}$$

Generally, Equation (5.61) is chosen in the estimation procedure of discrete Wigner-Ville Distribution (DWVD), because it is computationally efficient way to take L-point FFT instead of $4L$ or $2L$.

After numerically implementing DWVD, ISAR cross-range data columns can be processed to get target image. Dividing WVD algorithm into steps,

Step 1: Find the range profiles by using IFFT (stepped frequency) or range compression (LFM) methods such as match filtering.

Step 2: Choose the image time instant that is related to WVD plane time location. Apply step 3, 4, 5, 6, 7 to each column of resulting matrix.

Step 3: Interpolate the signal with 2 and find a sequence with length 2L.

Step 4: Find the time-dependent autocorrelation term $y[m+n]y^*[m-n]$ where m represents image time instant. (4L-point)

Step 5: Since the term in step 4 includes symetric terms, extract the one half of symetric terms. (2L-point)

Step 6: Since the term in step 5 includes zero terms extract the one half of all terms. (L-point)

Step 7: Final operation is taking L-point FFT of the term in step 6.

5.5.3.1 Simulations

In the Simulation 1, target model shown in Figure 5-5 is used. Simulation parameters are given in Table 5.11 and the corresponding image is presented in Figure 5-30.

Table 5.11: WVD ISAR Simulation-1 Parameters

Symbol	Name	Value
N	Number of Bursts	800
M	Number of Frequency Samples	512
f_c	Carrier Frequency	10 GHz
T	Pulse Repetition Interval	1 ms
B	Signal Bandwidth	400 MHz
Δf	Frequency Step Size	783 KHz
ω	Angular Velocity	0.2184 rad/s
$\Delta\theta = \omega NT$	Total angle variation	10°

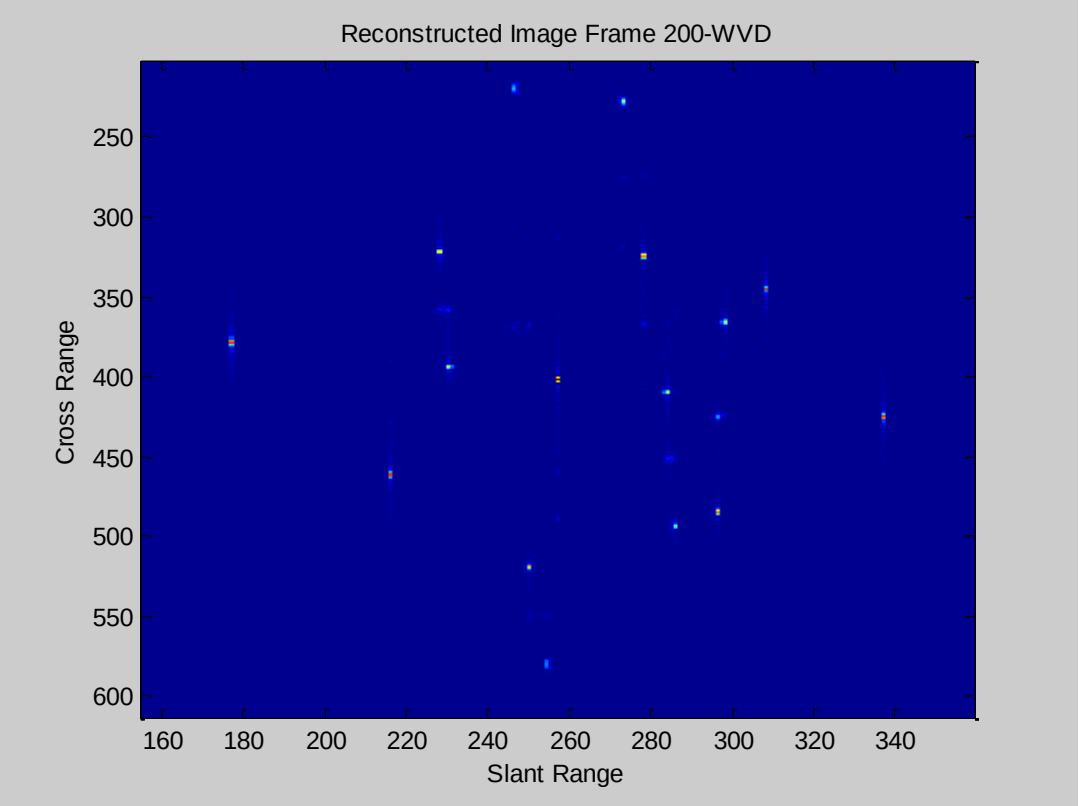

Figure 5-30: WVD ISAR Image with Cross-Terms (Scatterers in Same Range Bins)

Figure 5-30 shows that scatterers in the same range bin create unwanted cross-terms. The parameters of next simulation are given in Table 5.12 and the corresponding image is presented in Figure 5-31. In this simulation, the scatterers are moved to different range locations and the cleaner image can be reconstructed as shown in Figure 5-31.

Table 5.12: WVD ISAR Simulation-2 Parameters

Symbol	Name	Value
N	Number of Slow Time Samples	800
M	Number of Fast Time Samples	800
f_c	Carrier Frequency	10 GHz
τ	Pulse Width	1 us
f_s	Sampling Frequency	400 MHz
B	Signal Bandwidth	400 MHz
ω	Angular Velocity	0.2184 rad/s
$\Delta\theta$	Total angle variation	10°

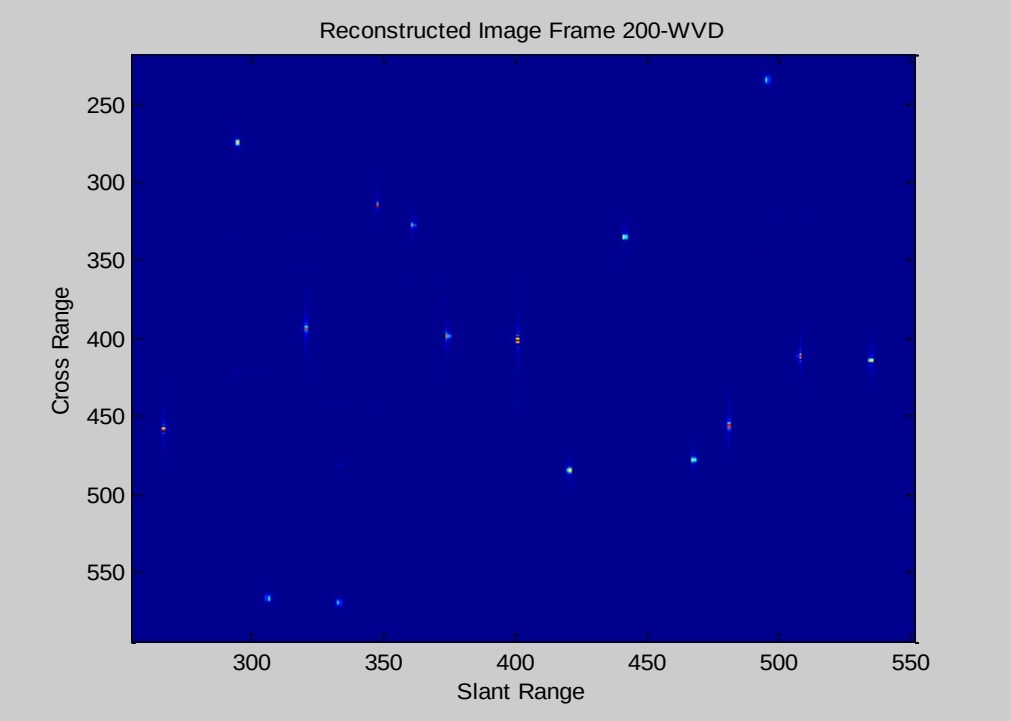

Figure 5-31: WVD ISAR Image Without Cross Terms (Scatterers in Different Range Bins)

5.5.4 Smoothed Wigner-Wille Distribution

This technique is based on the smoothing operation of Wigner-Ville distribution with the purpose of reducing cross-term interference. A feasible method of reduce the cross terms is to use windows in both dimensions of time-frequency plane.

A multicomponent signal can be represented as

$$x(t) = \sum_{i=1}^{p} x_i(t) \tag{5.62}$$

where p is the number of signal components. Then WVD of this signal becomes

$$WVD(t,f) = \sum_{i=1}^{p} WVD_{xi}(t,f) + \sum_{i,j=1,i\neq j}^{p} WVD_{xi,xj}(t,f) \tag{5.63}$$

First term of this expression is linear combination of auto terms. Second term is cross terms, which will interfere the auto-terms of WVD [15]. The signal terms of WVD are generally smooth components, whereas the interfering terms are strongly oscilated [2]. A general way of lowering the oscilatory components in 2D signal is to apply a 2D lowpass filter $H(t,f)$. This operation can also be thougth as a seperable smoothing in frequency and time dimensions.

- **Pseudo-Wigner-Ville Distribution**

As mentioned before, pseudo-wigner ville distribution is the windowed version of WVD.

$$PWVD_x(t,f) = \int_{-\infty}^{+\infty} h(\tau)x^*\left(t-\frac{\tau}{2}\right)x(t+\frac{\tau}{2})\,e^{-j2\pi f\tau} \tag{5.64}$$

Where $h(t)$ is a regular window (e.g. hamming windows). This windowing operation is equivalent to a frequency smoothing of Wigner-Ville distribution since

$$PWVD_x(t,f) = \int_{-\infty}^{+\infty} H(f-\varepsilon)WVD_x(t,u)\,d\varepsilon \tag{5.65}$$

where *H*(*f*) is the Fourier transform of windowing function *h*(*t*). Because of the oscilatory behaviors of cross-terms, they will be attenuated in the pseudo-wigner ville distribution compared to the WVD.

- **Seperable Smoothing**

It is the application of an independent time and frequency smoothing to lower the cross term interference. A window function is added for time dimension of WVD also. ($g(t)$) Resulting equation of two-step smoothing operation is called *smoothed-pseudo Wigner-Ville distribution.* In other words, it is 1D time domain convolution of pseudo-Wigner Ville distribution with window function.

$$SPWVD_x(t,f) = \int g(t-u)PWVD_x(u,f)\,du \tag{5.66}$$

$$SPWVD_x(t,f) = \int_{-\infty}^{+\infty}\int_{-\infty}^{+\infty} g(t-u)h(\tau)x^*\left(u-\frac{\tau}{2}\right)x(u+\frac{\tau}{2})\,e^{-j2\pi f\tau}dud\tau \tag{5.67}$$

It can be seen that if we choose time window function as an impulse function i.e. $g(t) = \delta(t)$, we obtain $PWVD_x(t,f)$ which applies only frequency smoothing. Discretizing this formula will be defined as

$$SPWVD_x(n,m) = \sum_k g(k)PWVD_x(n-k,m) \tag{5.68}$$

$$SPWVD_x(n,m) = \sum_k g(k)\sum_l h(l)x(n-k-l)x^*(n-k+l)e^{j4\pi lm/L} \tag{5.69}$$

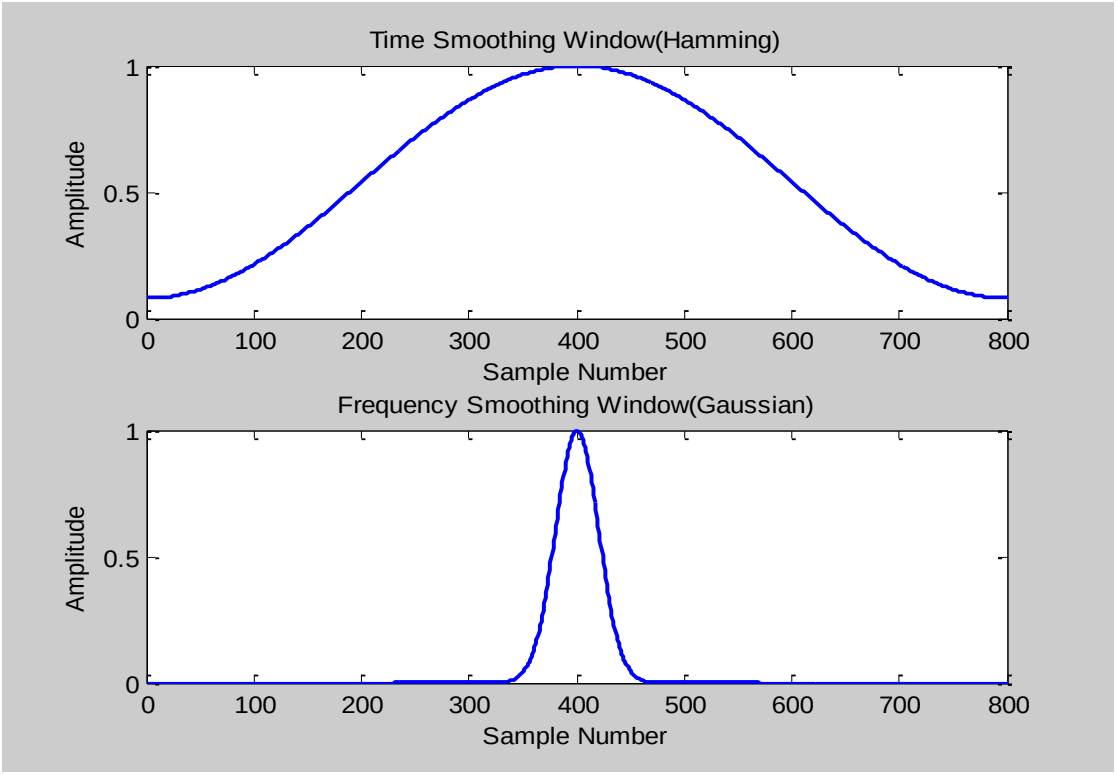

Figure 5-32: Smoothing Window Examples for Time and Frequency Dimensions

Figure 5-32 shows two choices for time and frequency seperable smoothing window. After finding time-dependent autocorrelation function, the FFT of time windowed version of this signal is taken. After constructing 2D-WVD plane each row corresponding to one frequency component is convolved with the frequency smoothing window. So that oscilatory terms can be removed from the ISAR image.

- **2D Low-Pass Filtering**

In the previous parts of Section 5.5.4, smoothing operations are done independently in time and frequency dimensions. Actually, oscilated terms in 2D plane can be removed by using 2D low-pass filters. This method is a general application of smoothing process and involves previous step-by-step methods. Although low-pass filter can substantially suppress the cross-terms, smoothing operation will reduce the resolution as a trade off [2].

2D Convolution of WVD and $H(t,f)$ can be written as

$$SWVD_x(t,f) = \iint WVD_x(x,y)H(t-x,f-y)dxdy \tag{5.70}$$

Lets choose a low-pass filter in the form of

$$H(t,f) = g(t)L(f) \tag{5.71}$$

where $L(f)$ is the Fourier transform of frequency smoothing window $h(t)$ and $g(t)$ is the time smoothing function. Then resulting expression will be equivalent to SPWVD which is actually a special way of 2D low-pass filtering.

These three methods can be applied to WVD of cross-range columns of ISAR simulator data after finding range profiles.

Step 1: Find range profiles by using IFFT or pulse compression techniques such as match filtering.

Step 2: Find the columns of $s^*\left(t-\frac{\tau}{2}\right)s\left(t+\frac{\tau}{2}\right)h(\tau)$ for all time instants t where $h(\tau)$ is a function such as hamming window.

Step 3: Take the FFT of each column.

Step 4: Step 3 will create a 2D matrix dimensions of which are time and frequency. Convolve each row of this matrix with Gaussian window. Note that amount of smoothing can be adjusted by changing the variance of Gaussian window.

5.5.4.1 Simulations

In the simulations, target model shown in Figure 5-33 is used.

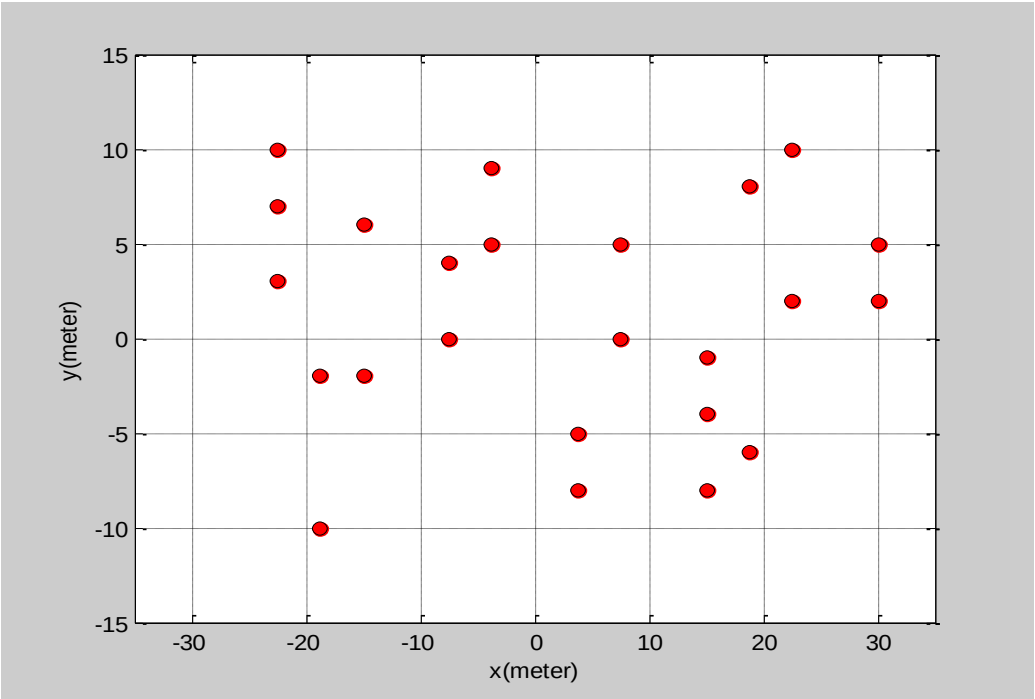

Figure 5-33: Target Model for SWVD Simulation

Simulation parameters are given in Table 5.13 and the corresponding output images of WVD and SWVD techniques are presented in Figure 5-34 and Figure 5-35.

Table 5.13: SWVD ISAR Simulation Parameters

Symbol	Name	Value
N	Number of Slow Time Samples	800
M	Number of Fast Time Samples	800
f_c	Carrier Frequency	10 GHz
τ	Pulse Width	1 us
f_s	Sampling Frequency	400 MHz
B	Signal Bandwidth	400 MHz
ω	Angular Velocity	0.437 rad/s
$\Delta\theta$	Total angle variation	10°

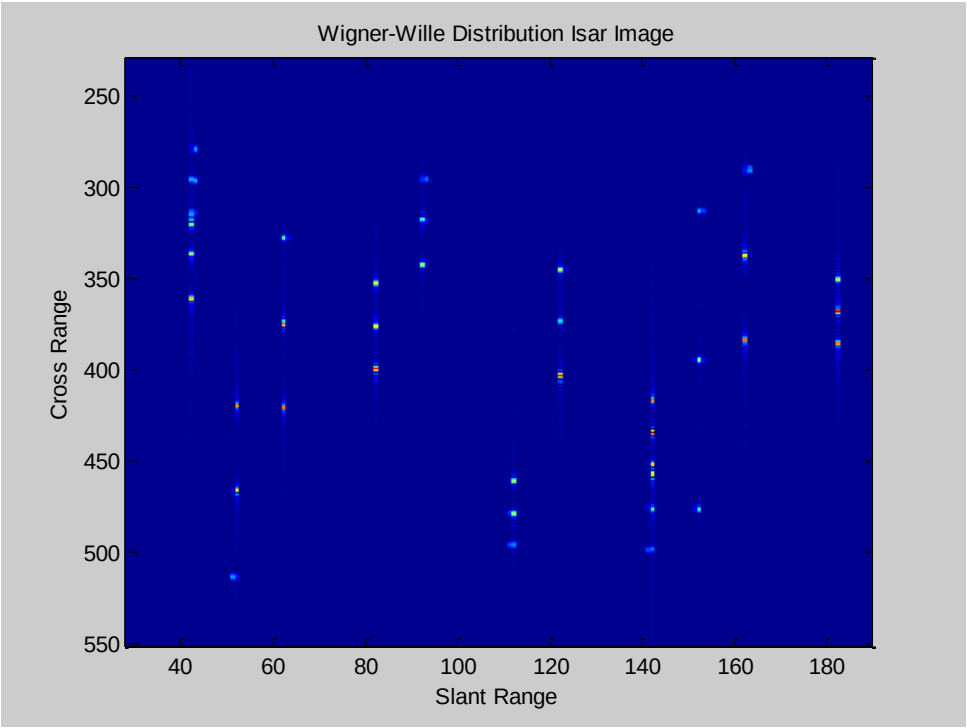

Figure 5-34: Cross-Term Interferences at the Output of WVD Technique

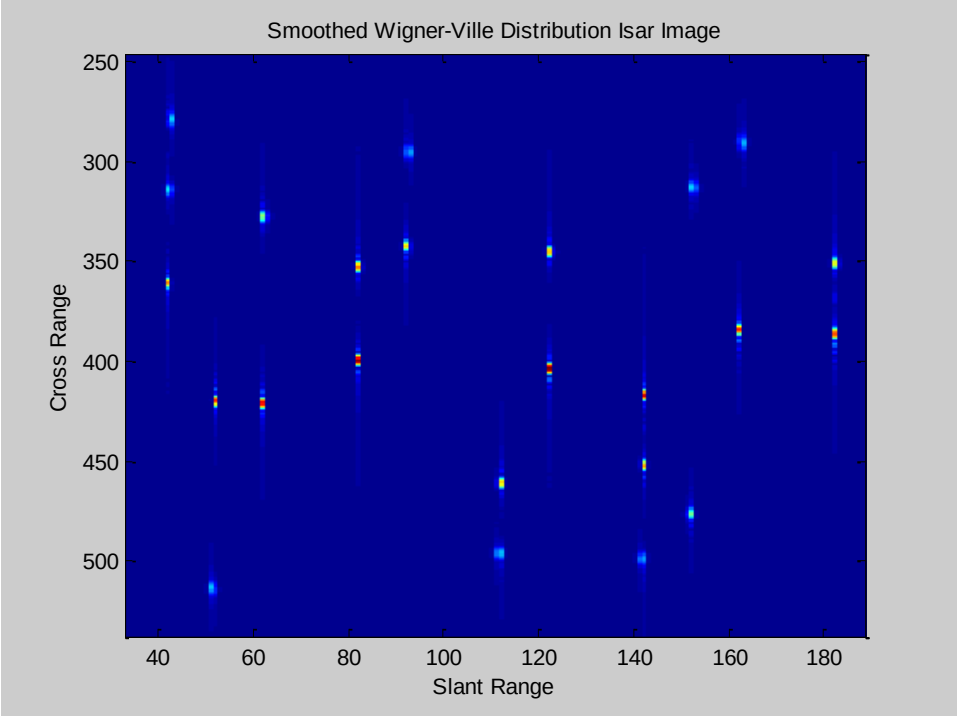

Figure 5-35: Cross Term Suppression of Smoothed WVD Technique

5.5.5 Cohen's Class Member, Choi-Williams Distribution

Cohen proposed a simple method to derive different time-frequency distributions which is called as Cohen's class. This method convolves different functions with time-dependent auto-correlation function and creates desired time-frequency distributions. These spesific functions are also called as kernel functions of distribution series. For a correct time-frequency distribution interpretation, it must at least satisfy non-negativity and correct marginal properties for time and frequency [31]. Choi-Williams distribution is a member of Cohen's class.

An easy way of understanding Cohen's class is from the ambiguity function domain. Ambiguity function is a similar expression with WVD. Taking Fourier transform with respect to t instead of τ gives the symmetric ambiguity function formulation [2].

$$AF_s(\vartheta,\tau) = \int s(t+\tau/2)\, s^*(t-\tau/2) e^{-j2\pi\vartheta t} dt \tag{5.72}$$

Then by taking inverse Fourier transform of ambiguity function $AF_s(\vartheta,\tau)$ we can easily obtain time-dependent auto-correlation function that we mentioned before.

$$s\left(t+\frac{\tau}{2}\right) s^*\left(t-\frac{\tau}{2}\right) = \frac{1}{2\pi}\int AF_s(\vartheta,\tau) e^{j\vartheta t} d\vartheta \tag{5.73}$$

Replacing this expression with the one in wigner-ville distribution yields

$$WVD_s(t,\omega) = \frac{1}{2\pi}\iint AF_s(\vartheta,\tau) e^{-j[\omega\tau-\vartheta t]} d\vartheta d\tau \tag{5.74}$$

It can be seen that WVD can be written as double Fourier transformation of symettric ambiguity function. If we obtain WVD of a signal we can easily pass into ambiguity domain. The only work to do is to take Fourier transform over τ and inverse Fourier transform over ϑ. Ambiguity domain is very useful to see the cross-terms of time-frequency representation. Cross-terms of WVD are located in the middle of auto terms and they have high oscilations. Ambiguity domain collects the auto terms around the origin and cross-terms are away from the origin. The farther

away ambiguity function is from the origin of ambiguity domain, the higher oscilations occurs in WVD domain, so that it can be possible to see and remove these terms from the ambiguity domain. In other words applying a special 2D window to ambiguity function lowers the cross-terms.

In the applications, we use Choi-Williams distribution which is a special type of 2D windowing in the ambiguity domain. To understand the relationships one may define new time-dependent auto-correlation function [2]

$$R(t,\tau) = \frac{1}{2\pi}\int AF_s(\vartheta,\tau)\Phi(\vartheta,\tau)e^{j\vartheta t}d\vartheta \tag{5.75}$$

where $\Phi(\vartheta,\tau)$ is called as kernel function. Since the multiplication in Fourier domain refers to convolution in time domain, the expression can be rewritten as [2]

$$\begin{aligned} R(t,\tau) &= [s\left(t+\frac{\tau}{2}\right)s^*\left(t-\frac{\tau}{2}\right)]\otimes \emptyset(t,\tau) \\ &= \int s\left(u+\frac{\tau}{2}\right)s^*\left(u-\frac{\tau}{2}\right)\emptyset(t-u,\tau)du \end{aligned} \tag{5.76}$$

where $\emptyset(t,\tau)$ is the inverse Fourier transform of $\Phi(\vartheta,\tau)$. This equation means that new auto-correlation function is time-domain filtered version of the function that is placed in Wigner-Ville distribution.

Finally, general expression of Cohen's Class can be written as

$$C(t,w) = \frac{1}{2\pi}\iint AF_s(\vartheta,\tau)\Phi(\vartheta,\tau)e^{-j[w\tau-\vartheta t]}d\vartheta d\tau \tag{5.77}$$

or

$$C(t,w) = \frac{1}{2\pi}\iint s\left(u+\frac{\tau}{2}\right)s^*\left(u-\frac{\tau}{2}\right)\emptyset(t-u,\tau)due^{-jw\tau}d\tau \tag{5.78}$$

Choi-Williams distribution uses an exponential kernel function $\Phi(\vartheta,\tau)$ to suppress the cross-terms. This function has a suitable shape to remove the terms away from the origin.

$$\Phi(\vartheta,\tau) = e^{-\alpha(\vartheta\tau)^2} \tag{5.79}$$

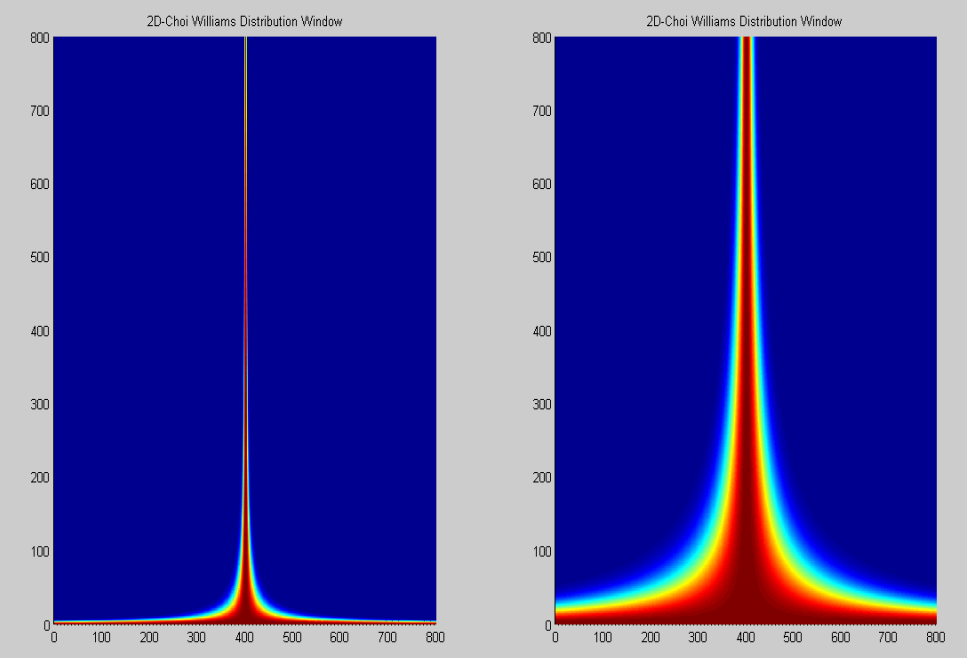

Figure 5-36: 2D-CWD Windows in the Ambiguity Domain Changing With α

The parameter α controls the suppresion amount of cross-terms. Increasing α improves the suppresion ability whereas the larger α disturbs more auto-terms as a trade off. Figure 5-36 shows large and small values of α. Inverse Fourier transform of kernel function is

$$\emptyset(t,\tau) = \frac{1}{\sqrt{4\pi\alpha\tau^2}} e^{-\frac{1}{4\alpha\tau^2}t^2} \tag{5.80}$$

Then Choi-Williams distribution expression can be written by using convolution property

$$C(t,\omega) = \iint \frac{1}{\sqrt{4\pi\alpha\tau^2}} e^{-\frac{1}{4\alpha\tau^2}(t-u)^2} s\left(u+\frac{\tau}{2}\right) s^*\left(u-\frac{\tau}{2}\right) e^{-j\omega\tau} du d\tau \tag{5.81}$$

5.5.5.1 Simulations

In the simulations, target model shown in Figure 5-33 is used. Simulation parameters are given in Table 5.14 and the simulation results are presented in Figure 5-37 and Figure 5-38.

Table 5.14: CWD ISAR Simulation Parameters

Symbol	Name	Value
N	Number of Slow Time Samples	800
M	Number of Fast Time Samples	800
f_c	Carrier Frequency	10 GHz
τ	Pulse Width	1 us
f_s	Sampling Frequency	400 MHz
B	Signal Bandwidth	400 MHz
ω	Angular Velocity	0.2184 rad/s
$\Delta\theta$	Total angle variation	10°

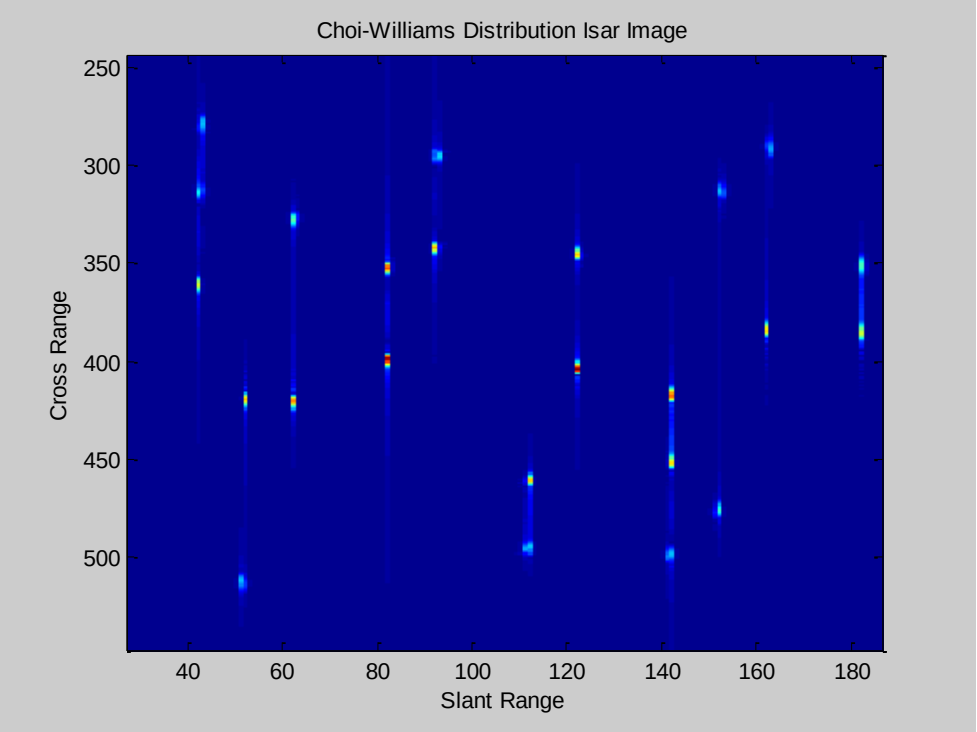

Figure 5-37: Cross-Term Suppression of Choi-Williams Distribution Algorithm

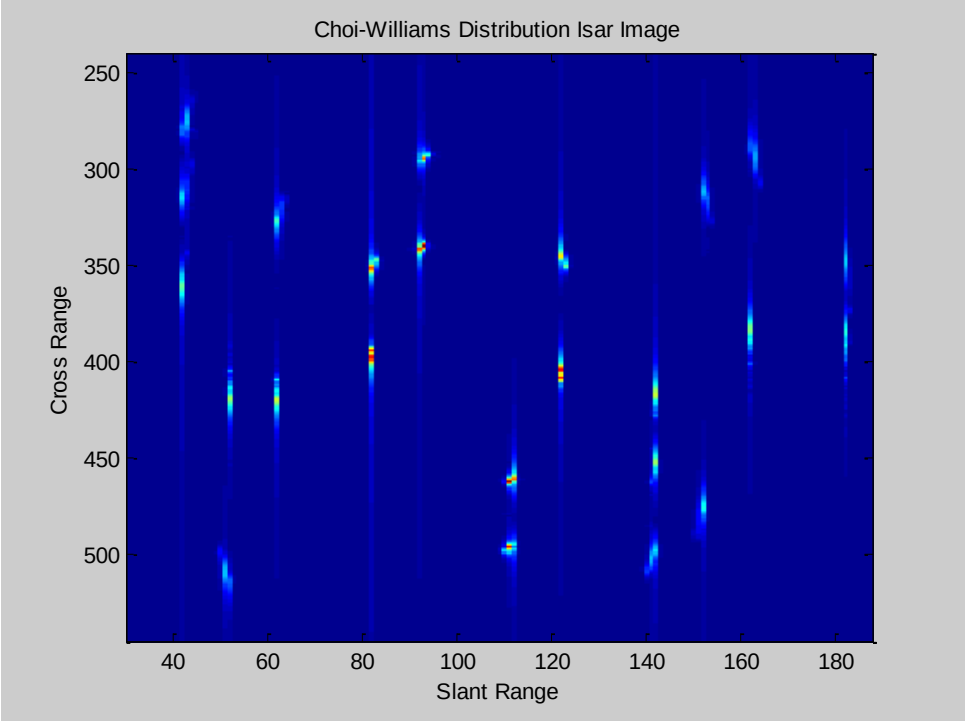

Figure 5-38: Auto-Term Distortion of CWD Because of Increasing α.

Figure 5-37 and Figure 5-38 provide information to visualize the configurable cross-term suppression by using Choi-Williams Distribution. These figures are generated for the same input as Figure 5-34. It can be seen that cross-terms in the WVD image are removed sufficiently. The parameter α can be adjusted to balance the cross-term suppression against auto-term distortion. In real life, parameter α should be choosen as configurable to see the effects on the reconstructed image.

5.6 Comparison of ISAR Reconstruction Methods

In this section, SNR and resolution performances of different ISAR image reconstruction techniques are compared for the input which is generated by ISAR simulator.

5.6.1 SNR Based Comparison

Evaluating the SNR performances of algorithms simulation runs twice for each algorithm. First run gives the output image without noise. Second run with a specific SNR gives the noisy image formation. Output error is calculated by taking the difference of these two images and finding mean square power of all indices in matris. By dividing output peak signal power with this value output SNR is obtained as the performance evaluation criteria. Error function can be written as

$$Noise\ Power = \frac{1}{MN}\sum_{m=1}^{M}\sum_{n=1}^{N}|I_2(m,n) - I_1(m,n)|^2 \tag{5.82}$$

where I_2 is noisy run output matris and I_1 output matris without noise and finally SNR is obtained as

$$SNR_{out}(dB) = 10\log\left(\frac{Peak\ power}{Noise\ Power}\right) \tag{5.83}$$

Varying the input SNR by adjusting the noise variance that is added to input, several output samples are taken for each algorithm.

5.6.1.1 RD, PR and BP Algorithms

FFT based algorithms increase the input SNR by applying coherent integration. Range-Doppler algorithm directly reconstructs the target image using 2D-FFT. Large angle variation in RD simulation spread the scatterer signal terms over the final image. Since rectangular assumption of RD frequency-angle domain doesn't work well, 2D-FFT method can not give accurate estimates of scatterer locations. Polar formatting algorithm applies interpolation in range and angle dimensions to correct the frequency sample locations into a rectangular shape. Applying 2D-FFT to the interpolated data increase the SNR performance of ISAR image reconstruction. PR technique has the same purpose with BP that it also tries to project the input data onto scatterer location. Back-Projection algorithm projects all input data samples of matris to one scatterer and integrate all of them. Back-Projection removes the interpolation errors and gives a larger SNR at the output of integration. Figure 5-39 compares the SNR performances of these 3 algorithms with the total viewing angle $\Delta\theta = 10°$. Here we didn't include the 2D-MUSIC algorithm since it does't estimate the amplitudes of scatterers.

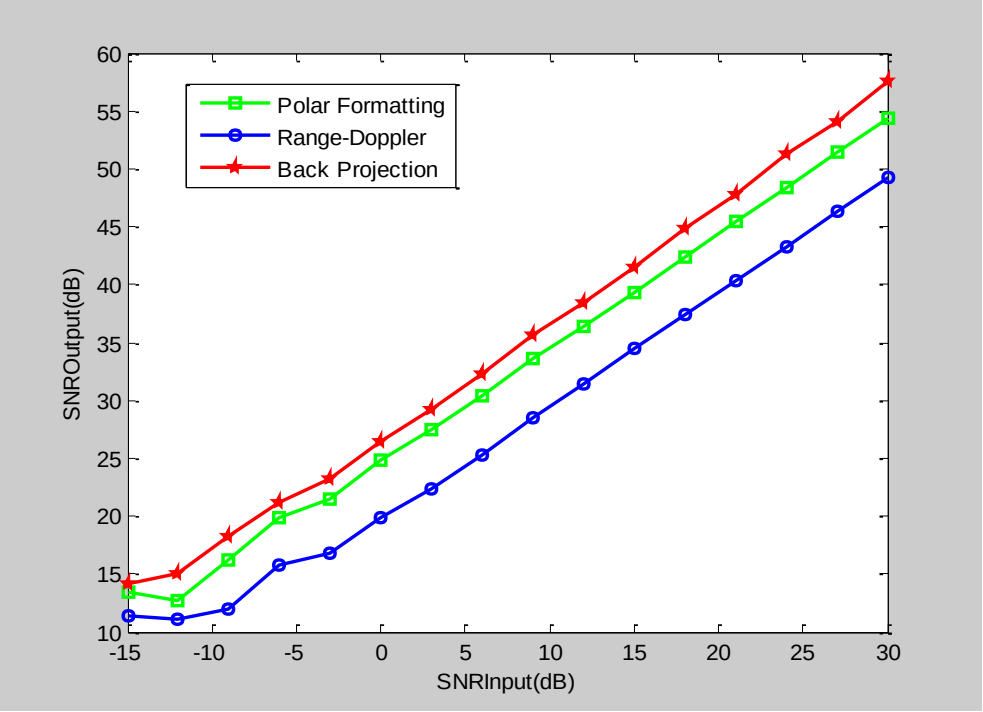

Figure 5-39: Output SNRs of PR, BP and RD Algorithms

As mentioned before PR and BP algorithms remove the spreading effects in RD image due to rotational motion. If the rotational velocity is estimated correctly, then BP or PR target imaging can achieve very high resolution. Here are the examples of images of the same target with known velocity. Target model which is used in these simulations is shown in Figure 5-40. Noise sensivity of these algorithms can be observed in Figure 5-41, Figure 5-42 and Figure 5-43 corresponding to different input SNRs.

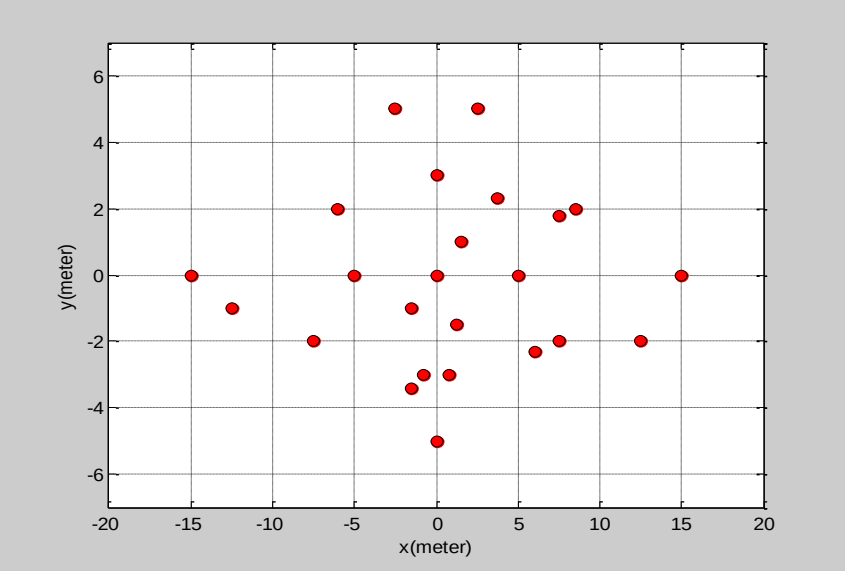

Figure 5-40: Target Model for Comparison of RD, BP and PR Algorithms

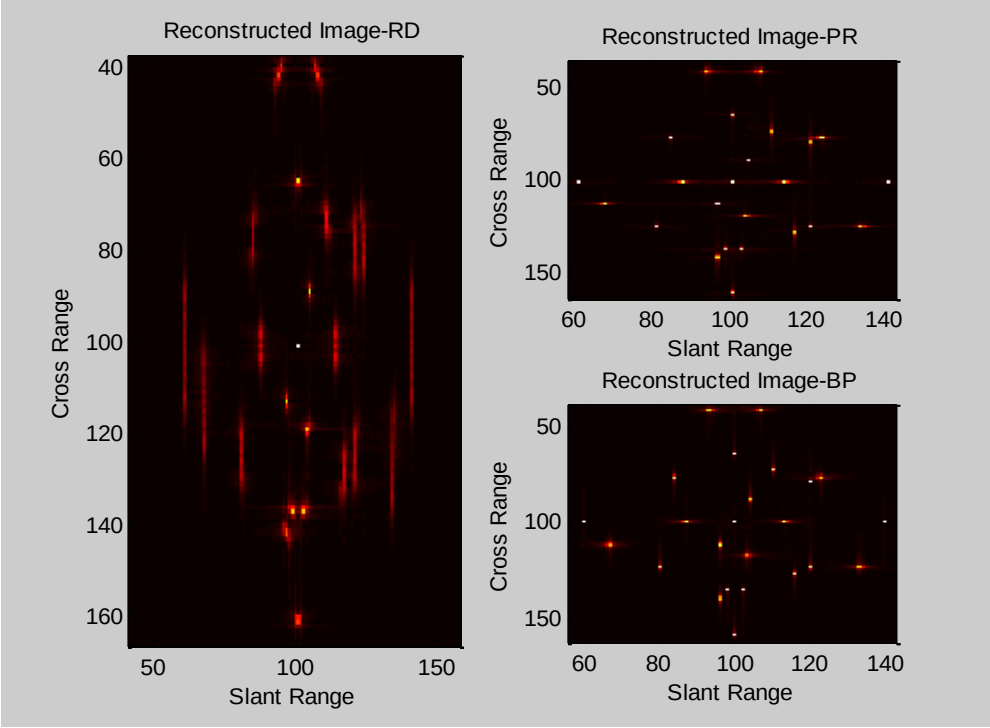

Figure 5-41: Reconstructed RD, BP, PR Images with SNR: 30dB

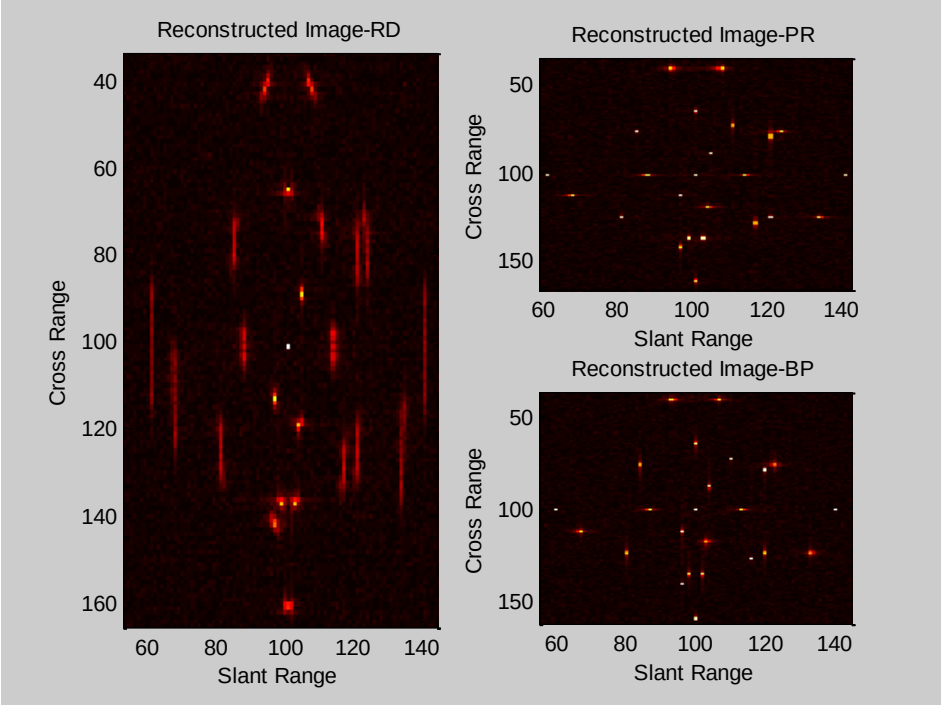

Figure 5-42: Reconstructed RD, BP, PR Images with SNR 10dB

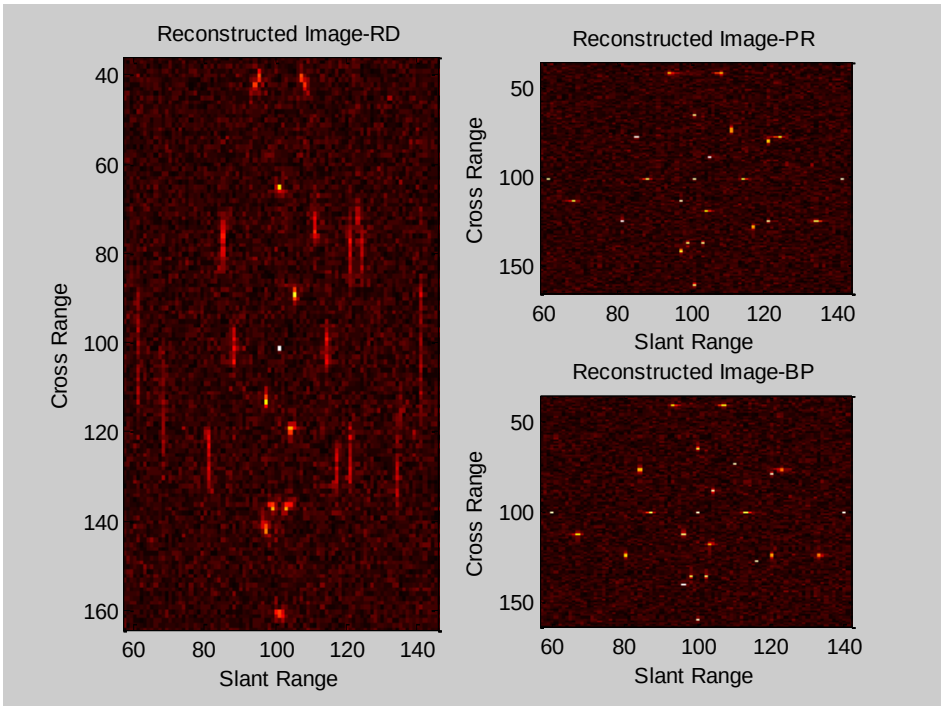

Figure 5-43: Reconstructed RD, BP, PR Images with SNR: 0dB

5.6.1.2 Time-Frequency Techniques

Time-frequency based image formation techniques offer many advantages over FFT method if it is used for the targets which have complicated motions [28]. TFDs can describe the instantenous frequency behavior of target signals. In this part, the output SNRs of the time frequency based ISAR imaging methods will be compared. TFDs examined are Short-Time Fourier Transform, WVD, SWVD and CWD.

Figure 5-44 compares the time-frequency based image qualities under the noisy environment.

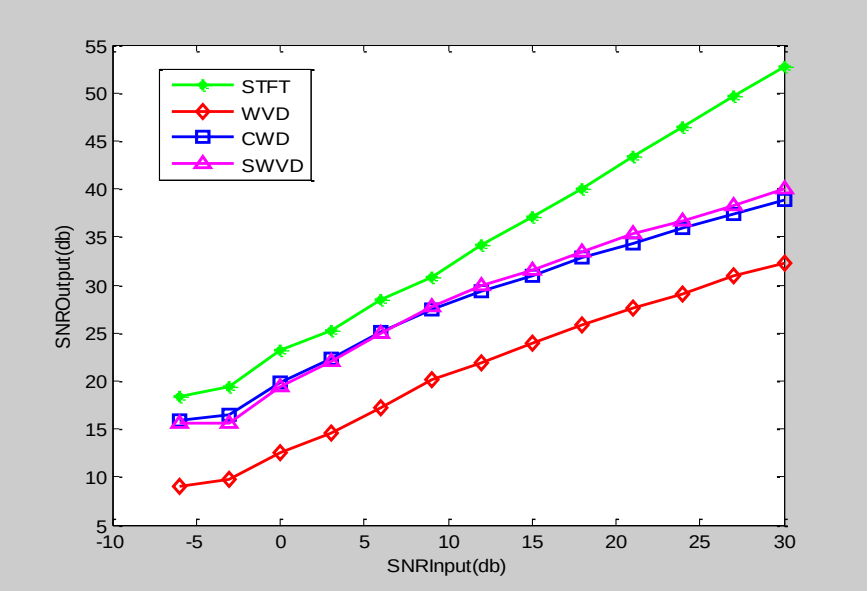

Figure 5-44: Output SNRs of Time-Frequency Based Algorithms

It can be concluded that the cleanest image formation can be done by using short-time Fourier transform. The WVD has strong interference terms which means that unwanted peaks in the output can be seen. SPWVD can suppress the cross-term interferences by using smoothing windows. Also CWD has similar performance with SPWVD since it removes cross-terms in a similar manner.

To simulate time-frequency techniques target model shown in Figure 5-5 is used.

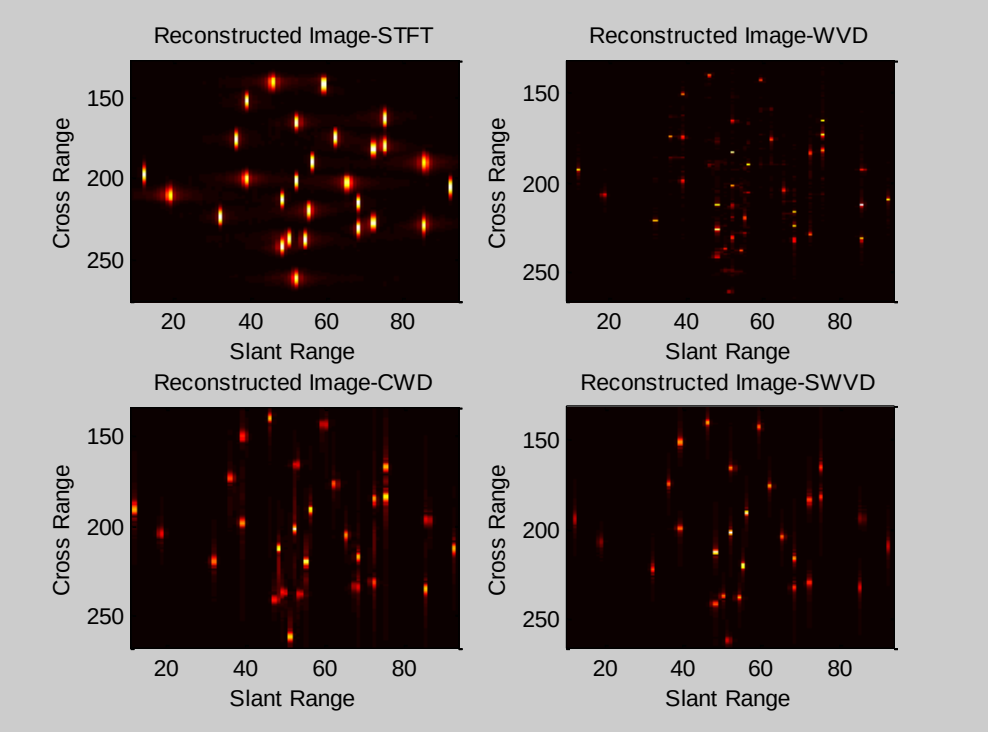

Figure 5-45: Reconstructed Time-Frequency Images with SNR: 30dB

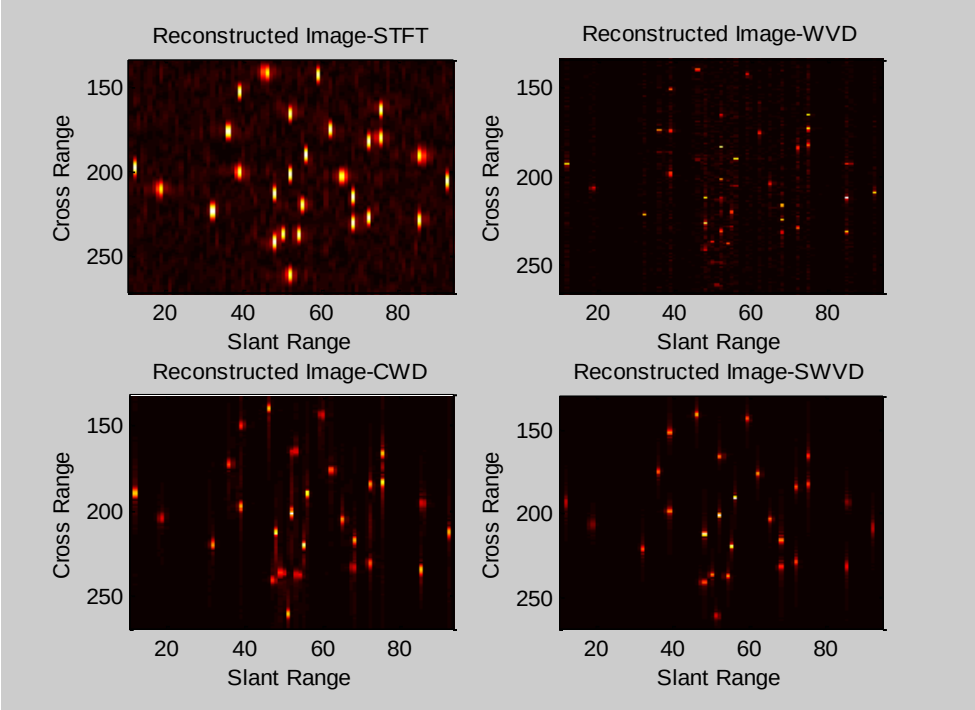

Figure 5-46: Reconstructed Time-Frequency Images with SNR: 10dB

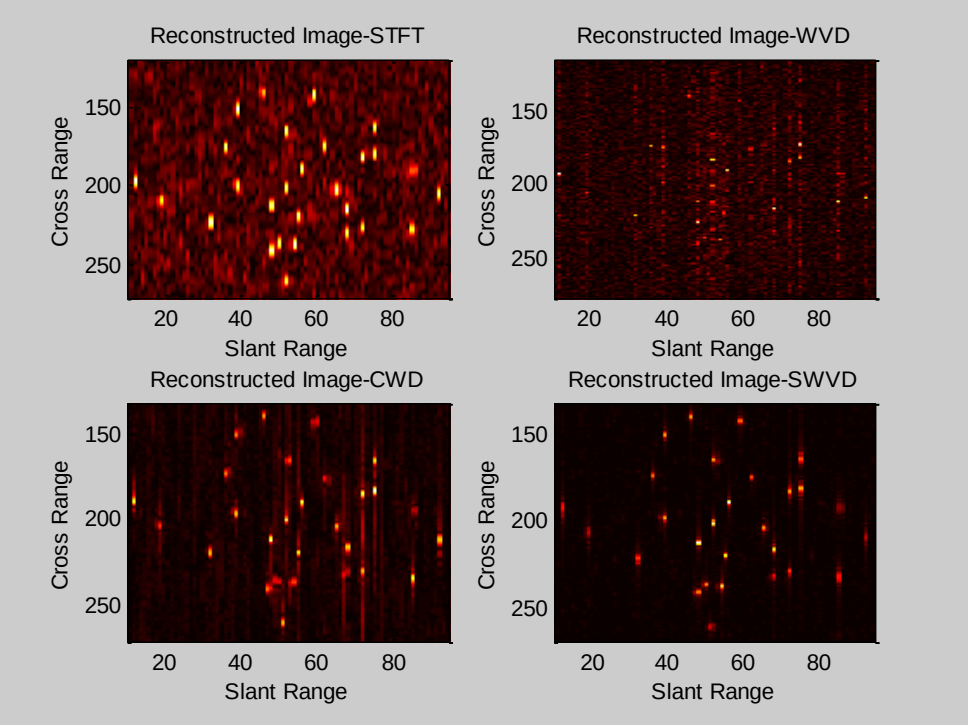

Figure 5-47: Reconstructed Time-Frequency Images with SNR: 0dB

Figure 5-45, Figure 5-46 and Figure 5-47 are time-frequency based reconstructed images with different SNRs. It is observed that WVD has cross-terms between the same scatterers in the same range cells. These unwanted terms degrade the performance under the noisy conditions. Although STFT based image seems to be much noisy, peaks of the signal doesn't disappear easily since it has no cross-terms. CWD performance depends on the parameter α (Section 5.5.5). This parameter is choosen as 10e-5 for these simulations. It removes the unwanted-terms but also original terms can be destroyed by this way. CWD weak signals cause the output SNR to decrease. SWVD uses seperable smoothing in time-frequency plane and suppresses the interference terms of WVD as can be seen from the figures above. SWVD time and frequency smoothing windows should be choosen optimally to improve the image quality.

5.6.2 Resolution Based Comparison

Output cross-range resolution performance of ISAR can be compared by plotting the cross-range output response of target scatterers for one range bin. Also from the output images cross range performance can be compared easily for all algorithms.

5.6.2.1 RD, PR and BP Algorithms

In this simulation, three scatterers whose cross-ranges are $-2.11, 2.11$ and 3.38 meters are located in same range bin.

For the objects that have small angle rotation it is unnecessary to apply interpolation. Because RD algorithm performance really approaches to the other ones. Then in this case, applying PR or BP only would waste computational load. Here is the result of the target with a total rotation of $\Delta\theta = 2.5°$. Figure 5-48 shows the similarities between the resolutions of these algorithms. However, small observation time limits the cross-range resolution. PR and BP should be used to have higher resolution results.

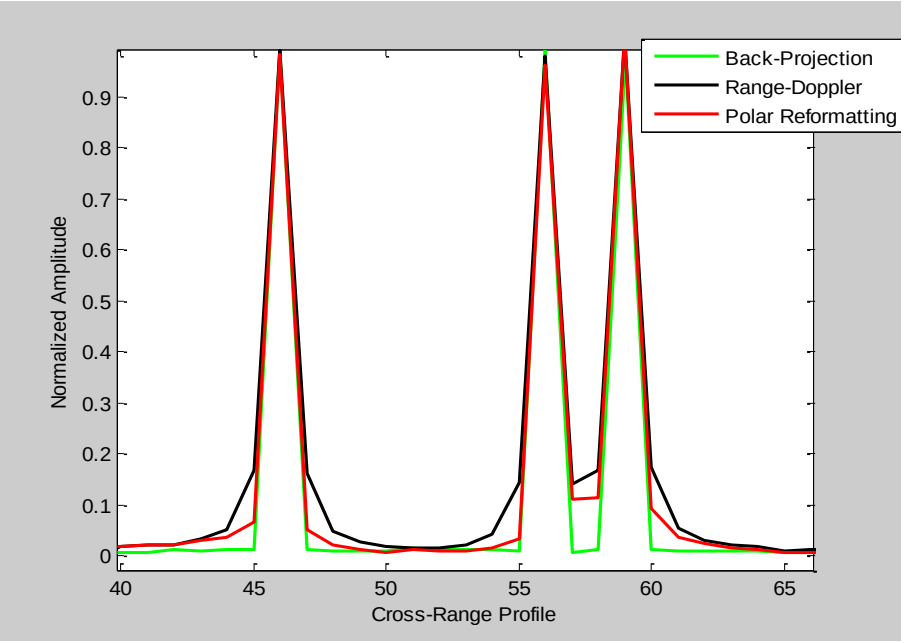

Figure 5-48: Cross-Range Response of Three Scatterers in Same Range Bin

Conventional 2D-FFT method can not give superresolution cross-range profiles. For the same range bin plotting the cross-range output is a method to compare the cross-range resolutions of these algorithms. The wide angle behaviours of these algorithms are compared in Figure 5-49.

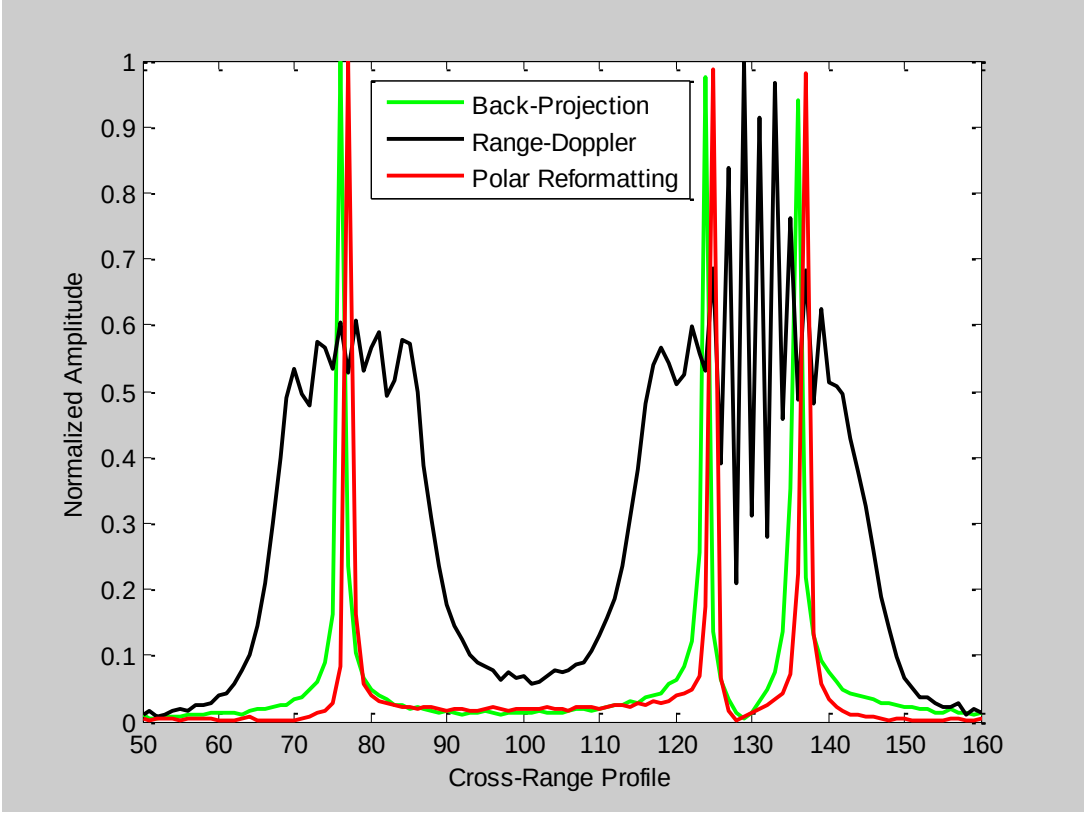

Figure 5-49: Cross-Range Response of Three Scatterers in Same Range Bin

In this simulation target rotates over a total angle $\Delta\theta = 10°$ that causes RD response to spread over the cross-range axis. As it is seen that BP and PR has similar resolutions and they improve the ISAR resolution performance sufficiently. Main lobes of PR and BP signals in Figure 5-48 and Figure 5-49 can be thougth as the criteria of resolution comparison. Obviously the second figure achieves higher resolution than the first one with the cost of computational work.

5.6.2.2 2D-MUSIC versus 2D-FFT

FFT based images don't have as accurate peaks as MUSIC based images. MUSIC algorithm can more highly resolve range and cross-range profiles of target. But in the case of low SNR, MUSIC algorithm can cause redundant peaks. Spectral estimation-based ISAR images are characterized by satisfactorily high resolution, even for quite small data sets [7]. Whereas 2D-FFT performance strongly depends on the number of frequencies (bandwidth) and look angle.

For the comparison of conventional 2D-FFT with this spectral estimation method visually, we can look at the reconstructed images for the same data and same SNR. Target model used in this simulation is shown in Figure 5-50. Figure 5-51, Figure 5-52 and Figure 5-53 are reconstructed images for different input SNRs.

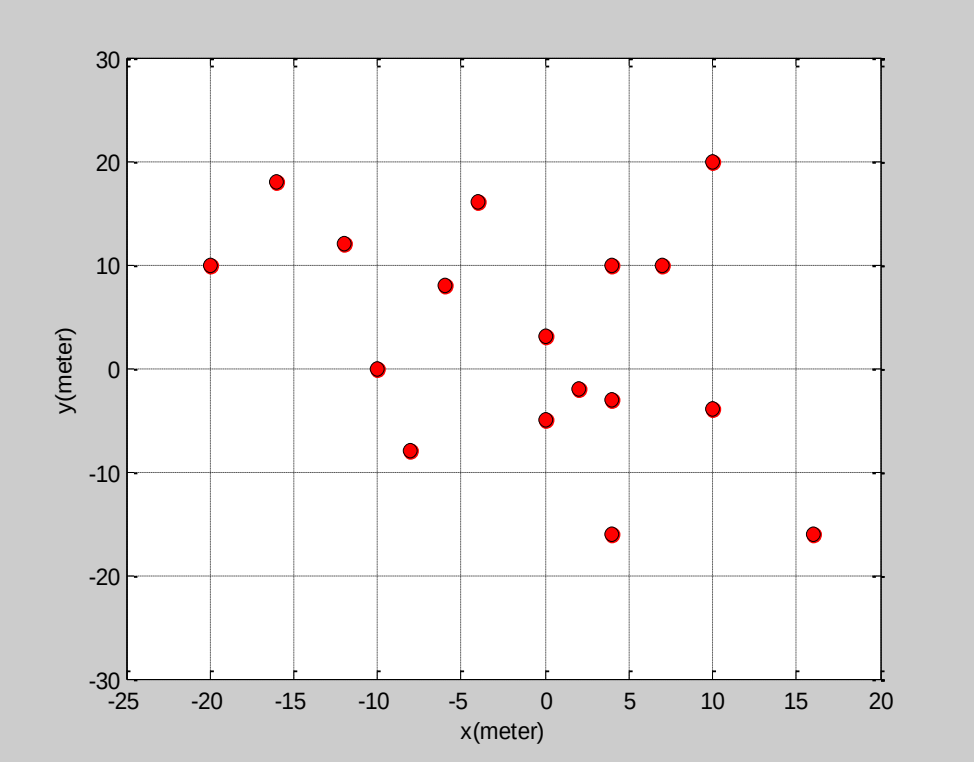

Figure 5-50: Target Model for RD and 2D-MUSIC Comparison

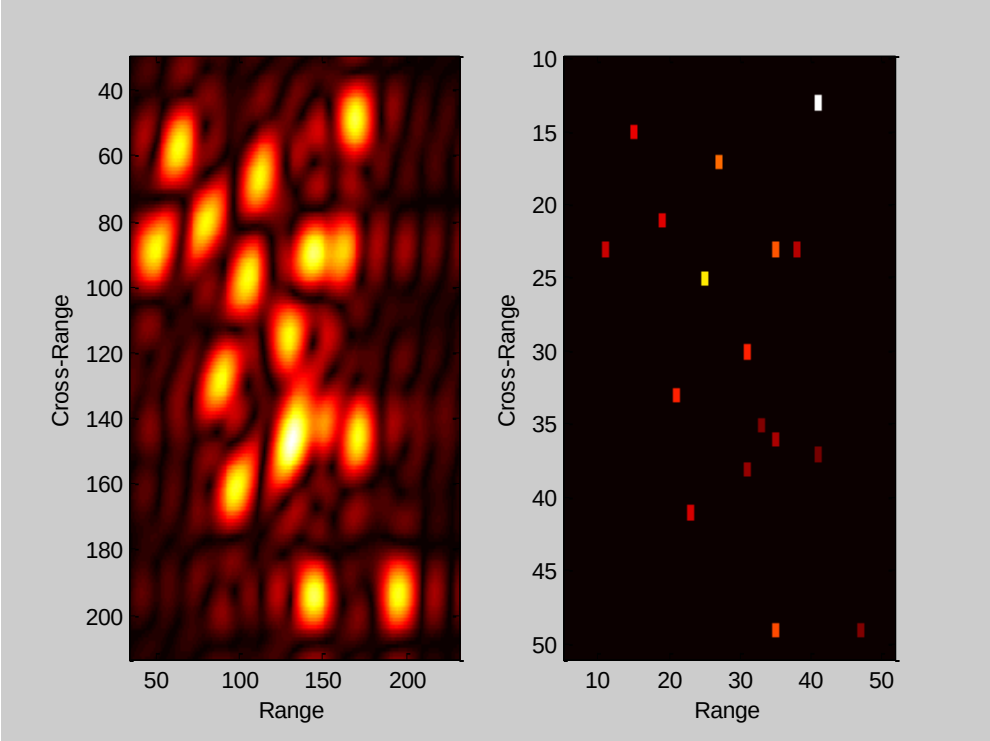

Figure 5-51: Reconstructed FFT and MUSIC Images with SNR: 30 dB

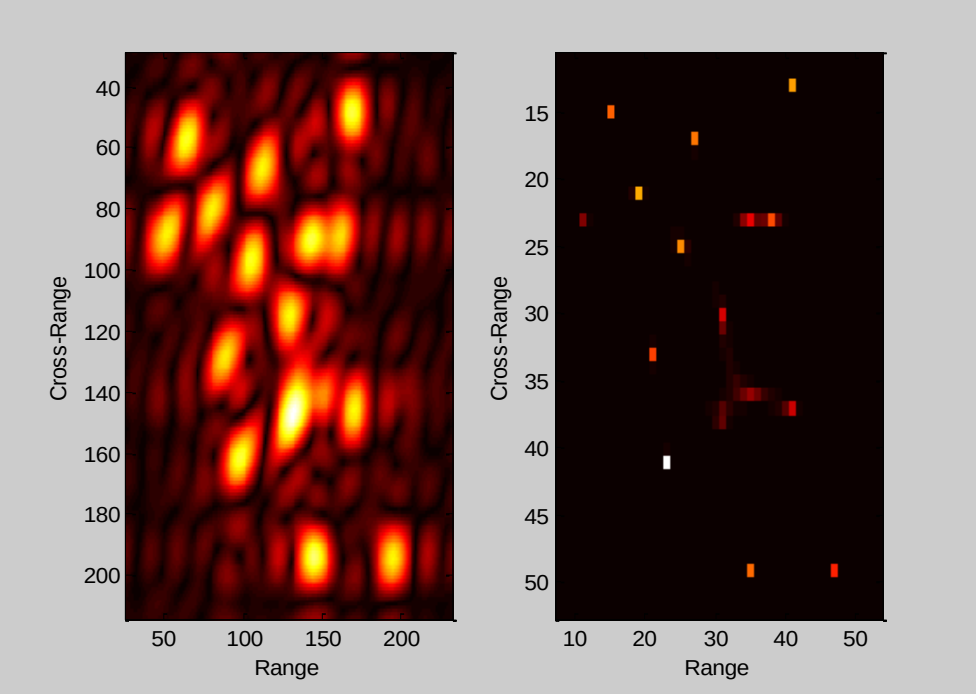

Figure 5-52: Reconstructed FFT and MUSIC Images with SNR: 15dB

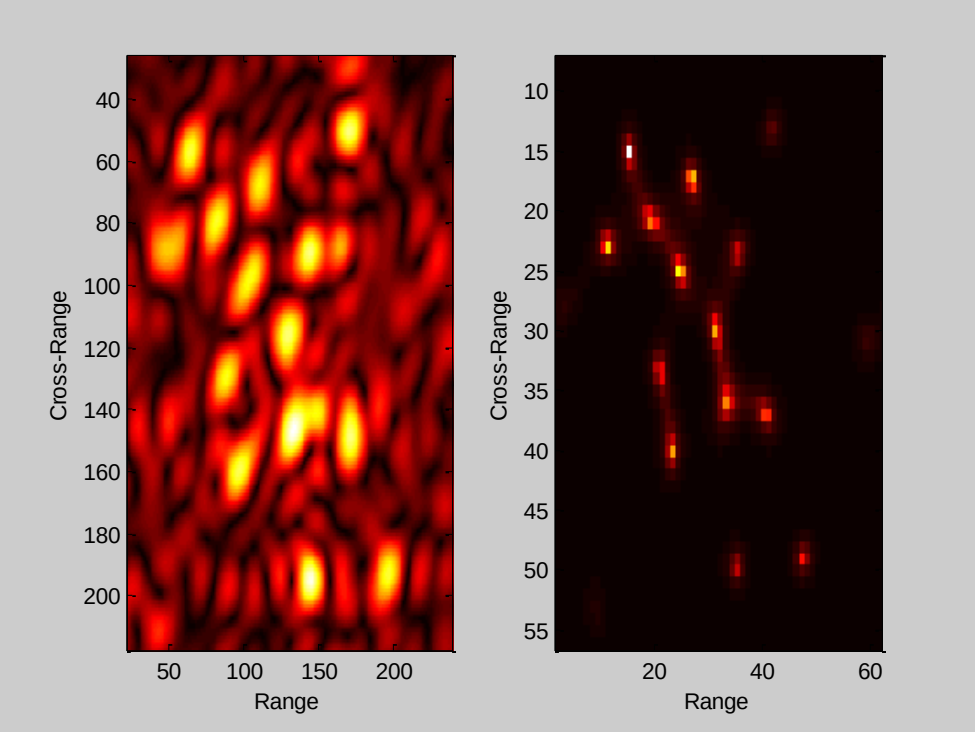

Figure 5-53: Reconstructed FFT and MUSIC Images with SNR: 3 dB

Figure 5-51, Figure 5-52 and Figure 5-53 intuitionally show the resolution improvement in 2D-MUSIC cases. Additionaly plotting one range profile is useful to compare the resolution performances of FFT and MUSIC based algorithms. In this simulation, four scatterers whose cross-ranges are $-5, -2,$ 3 and 6 meters are located in same range bin. Figure 5-54 shows the resolution success of 2D-MUSIC algorithm against classical 2D-FFT image formation. Target model consists of four scatterers in same range bin whose cross-ranges are 2D-MUSIC has narrower peak main lobes and can resolve adjacent scatterers that FFT can not.

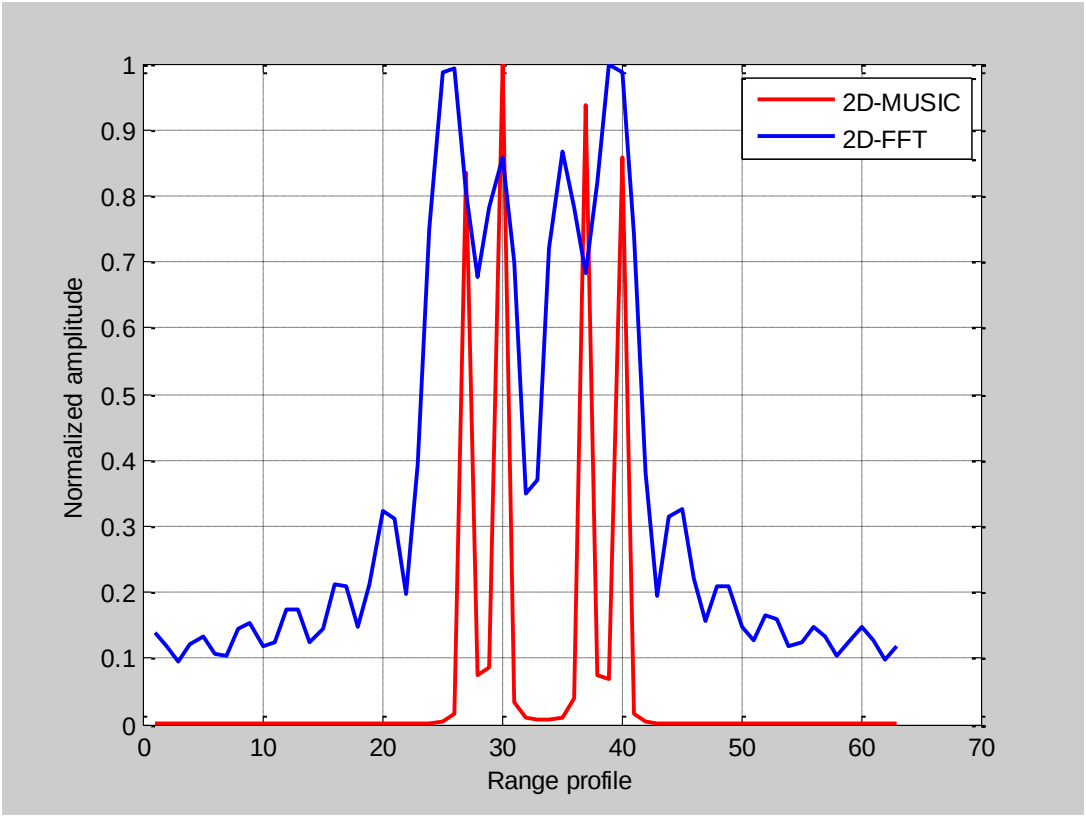

Figure 5-54: One Range Profile Including Four Scatterers

5.6.2.3 Time-Frequency Techniques

In this simulation, two scatterers are located on the same range bin and their cross ranges are 5 and 10 meters.

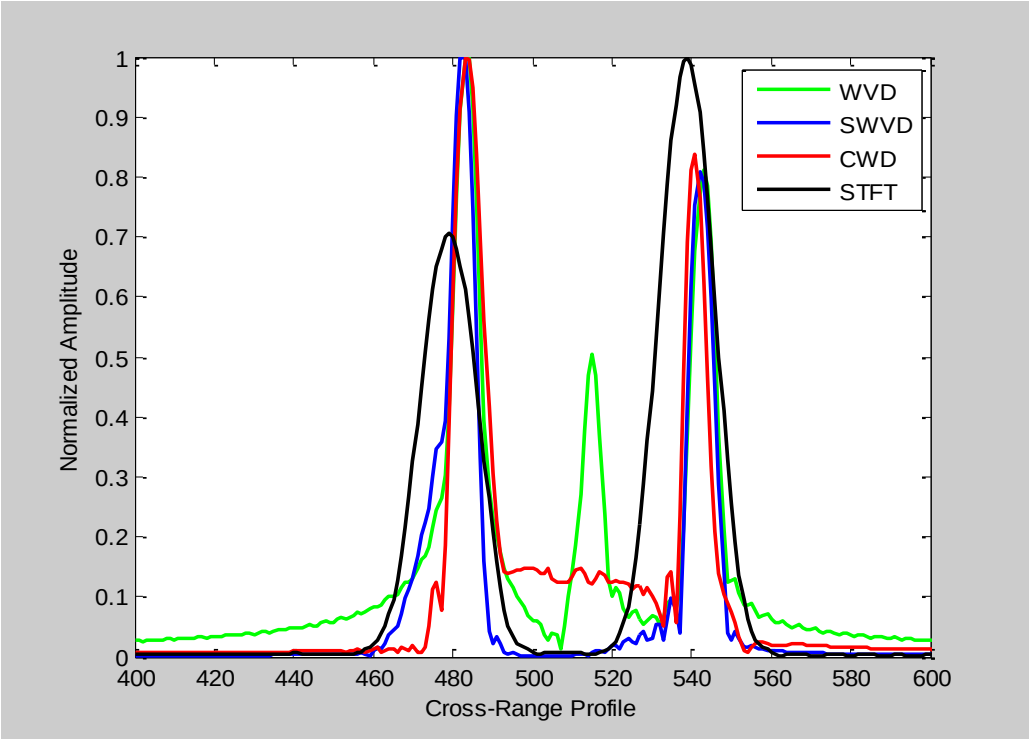

Figure 5-55: Cross-Range Response of 2 Scatterers in Same Range Bin

ISAR imaging algorithms consider cross-range responses of target scatterers. In this simulation, after applying range finding methods such as match filtering or IFFT cross-range response of targets for the same range bin is obtained and plotted for all time-frequency techniques.

The cross-term in the middle of the figure is because of the WVD nature. As we can see from the figure, STFT approach gives a clean cross-range response with wide main lobe which means lower resolution. Resolutions of WVD, SWVD and CWD seem to be similar. The purposes of CWD and SWVD approaches are based on

removing unwanted terms in WVD. Figure 5-55 shows the smooth results of SWVD and CWD.

5.6.3 Computational Load Based Comparison

For comparing the computational load, all algorithms are run in MATLAB with a 512×512 input data and the simulation times are given in Table 5.15.

Table 5.15: Comparison of Computational Loads of ISAR Algorithms

Algorithm	**Simulation Time (second)**
2D-MUSIC	19845
DTFT Based BP	15485
SWVD	375
CWD	242
IFFT Based BP	163
PR	9
WVD	0.5
STFT	0.1
RD	0.08

CHAPTER 6

CONCLUSIONS

In this thesis main concern is to compare different ISAR image reconstruction algorithms in terms of their performances. Basically ISAR image formation can be done by retrieving Doppler information of target scatterers from the input data. After constructing the ISAR signal model by designing the data simulator, results of algorithms are analysed. In addition, estimation of rotational velocity of targets is discussed and different solutions to this problem are given. The first image formation algorithm set investigated in this thesis consists of Range-Doppler, Polar Reformatting and Back-Projection algorithms. These algorithms assume that rotational rate of the target is known. Second algorithm set involves Joint Time-Frequency techniques which are STFT, WVD, SWVD and CWD. Assumption of rotational velocity is not required for these algorithms.

Range-Doppler algorithm gives good results in the case of small target rotations. It is an easy algorithm for practical applications. However resolution is limited since it depends on total angular change. Increasing the observation angle causes blurring effects in the final image because of the poor performance of 2D-FFT on input domain which is not rectangular.

In this case, Polar Reformatting algorithm is given to get accurate results for wide angles. It interpolates the polar domain data onto a rectangular domain by using uniform and nonuniform resampling properties. This algorithm requires the knowledge of rotational changes between views to correct the data. Then it becomes a challenging issue to estimate the rotational velocity of target and this situation

increases the difficulty of implementation. Also Polar Reformatting needs fast processors for the implementation of $sinc$ interpolations.

Similarly, Filtered-Back Projection algorithm gives very accurate results if it has the rotational rate information. This algorithm can use IFFT approach instead of DTFT to decrease the computational load. But this approach creates large interpolation errors especially for small angular changes. DTFT based back-projection directly projects the whole input data onto all scatterers to find the accurate peak locations. Since DTFT can handle noninteger frequency samples opposite to IFFT, interpolation errors are eliminated and similar results with PR is taken. Although it gives high resolution results for large aspect angles, it should be noticed that BP requires high computational load.

2D-MUSIC algorithm works on the rectangular data like 2D-FFT. This spectral estimation method can create superresolution images without increasing the observation angle. Beside that 2D-MUSIC algorithm is only applicable for input data with small dimension since it includes matrix manipulations such as autocorrelation estimation on whole data. In other words it limits the maximum acceptable rotations of target for the image reconstruction. Unless the input SNR is large enough 2D-MUSIC can create extraneous peaks at the output figure. Comparing it with 2D-FFT for the same rectangular data shows the resolution improvement easily. However, 2D-MUSIC only estimates the locations of scatterers. Reflectivities of scatterers need to be obtained by using some other algorithms as well.

Time-frequency techniques give high resolution images by estimating the instantenous Doppler changes of scatterers. It is possible to see the reconstructed images at different time samples by using time-frequency transforms. STFT is an easy way to reconstruct the images but it has limited time-frequency resolutions. WVD increases the resolution but reconstructed image seems to be dirty because of the cross-term interference. Smoothed WVD and CWD remove the interference terms to clean the image and preserve the high resolution. One of the most

important advantages of time-frequency techniques is that they don’t need to compensate any types of motion. Nature of time-frequency algorithms provides us to observe time varying target images. They can give us time dependent frequency behavior of cross-range signals. Beside that implementation of time-frequency transform for each cross-range column can take too much time.

Time-frequency analysis is a topic that should be analysed very deeply for ISAR. New adaptive joint-time frequency algorithms can be applied as a future work ([16], [17]). Time Frequency Distribution Series can be used to represent the WVD and remove the unwanted terms. From the literature matching pursuit algorithm can be implemented also [18]. Wavelet based ISAR imaging algorithms can be investigated. Spectral estimation methods for ISAR signals such as AR, CAPON can be compared to decide the availabilities of them. Estimation of unknown motion parameters of ISAR target can be a challenging topic to search. Auto focusing which denotes the motion compensation of ISAR targets is an important subject for ISAR investigations also. Entropy based techniques can be analyzed for auto focusing. Iterative methods to estimate the cross-range signal parameters can be searched. As a future work 3D-ISAR modeling can be adapted for real applications.

REFERENCES

[1]. W.G.Carrara, R.S.Goodman, R.M.Majewski, Spotligth Synthetic Aperture Radar: Signal Processing Algorithms, Artech House, 1995.

[2]. S.Qian, D.Chen, Joint-Time Frequency Analysis: Methods and Applications, Prentice Hall PTR, 1996.

[3]. Marco Martorella, Introduction to Inverse Synthetic Aperture Radar, Radar 2010 Tutorial Notes.

[4]. Wang, J. and Kasilingam, D. "Global range alignment for ISAR. IEEE Transactions on Aerospace and Electronic Systems", 39, 1 (Jan. 2003), 351—357.

[5]. Martorella, M., Berizzi, F., and Haywood, "B. Contrast maximization based technique for 2-D ISAR autofocusing". IEEE Proceedings–Radar, Sonar & Navigation, 152, 4, (Aug. 2005), 253-262.

[6]. Xiang Gu, Yunhua Zhang, "Effectiveness and Uniqueness Conditions for 2-D MUSIC Algorithm Used in ISAR Imaging" Synthetic aperture radar, APSAR. 2009, 2nd Asian-Pacific conference on digital object identifier.

[7]. A. Karakasiliotis and P. Frangos "Comparison of Several Spectral Estimation Methods for Application to ISAR Imaging", Proceedings of RTO SET 080 Panel Symposium, Oslo, Norway, pp. 1058–1067, 11-13 Oct. 2004.

[8]. Lieu, Z.S., Wu, R., and Li, J. "Complex ISAR imaging of maneuvering targets via the Capon estimator" IEEE Transactions on Signal Processing, **47**, 5 (May. 1999), 1262—1271.

[9]. Munoz-Ferreras, J. M. and Perez-Martinez, F. "Non-uniform rotation rate estimation for ISAR in case of slant range migration induced by angular motion." IET–Radar, Sonar & Navigation, 1, 4 (Aug. 2007), 251—260.

[10]. Werness, S., et al. Moving target imaging algorithm for SAR data. IEEE Transactions on Aerospace and Electronic Systems, 26, 1 (Jan. 1996), 57—67.

[11]. M. Xing R.Wu, Y.Li, Z.Bao "New ISAR imaging algorithm based on modified Wigner-Ville distribution", IET–Radar, Sonar & Navigation, 2009, Vol. 3, No. 1, pp. 70-80.

[12]. S. Barbarossa, "Analysis of multicomponent LFM signals by a combined Wigner-Hough transform", IEEE Transactions on Signal Processing, vol. 43, no. 6, pp. 1511–1515, 1995.

[13]. Gordan Cornelia, Morgog Lucian, Reiz Romulus, "Detection and Estimation of Linear FM Signals", IEEE (2005), 705-708.

[14]. V.C.Chen, H.Ling, Time-Frequency Transforms For Radar Imaging And Signal Analysis, Artech House, 2002.

[15]. Wang ran, jiang yi-cheng, "ISAR ship imaging based on reassigned smoothed pseudowigner-ville distribution", IEEE (2010).

[16]. Wang, Y., Ling, H., and Chen, V. C. "ISAR motion compensation via adaptive joint time-frequency technique", IEEE Transactions on Aerospace and and Electronic Systems, 34, 2 (Apr. 1998), 670—677.

[17]. Trintinalia, L. C. and Ling, H. "Joint time-frequency ISAR using adaptive processing", IEEE Transactions on Antennas and Propagation, 45, 2 (Feb. 1997), 221—227.

[18]. G. Li, H. Zhang, X. Wang, and X.-G. Xia, "ISAR 2-D imaging of uniformly rotating targets via matching pursuit", IEEE Transactions on Aerospace and Electronic Systems, vol. 48, no. 2, pp. 1838-1846, Apr. 2012.

[19]. D.R.Wehner, High-Resolution Radar. Artech House, 1995.

[20]. V.C.Chen and W. J.Miceli, “Simulation of ISAR imaging of moving targets”, IEE Proc.-Radar, Sonar Navig., Vol. 148, No. 3, June 2001.

[21]. Richards, M. A., Ph.D., Fundamentals of Radar Signal Processing, McGraw-Hill, 2005.

[22]. LONG Teng & REN LiXiang, “HPRF pulse Doppler stepped frequency radar”, Sci China Ser F-Inf Sci , May 2009, vol. 52, no. 5, 883-893.

[23]. Caner Özdemir, Inverse Synthetic Aperture Radar with Matlab Algorithms, Wiley Series in Microwave and Optical Engineering (Volume 1)

[24]. Y. Hua, E. Baqai, Y. Zhu, and D. Heilbronn, “Imaging of point scatterers from step-frequency ISAR data”, IEEE Transactions Aerospace Electron Systems 29 (1992), 195–205.

[25]. Francesco Prodi, “ISAR cross-range scaling using a correlation based functional”, IEEE(2008).

[26]. Mensa, Dean L. Radar Cross Section Imaging, Artech House, 1991.

[27]. David C.Munson, “A Tomographic Formulation of Spotlight-Mode Synthetic Aperture Radar,” Proceedings of the IEEE vol. 71, no.8, August 1983.

[28]. T. Thayaparan, G. Lampropoulos, “Quantitative SNR Analysis and Comparison of Different Time-Frequency Distributions for HRR Images”.

[29]. J. W. Odendaal, E. Barnard, and C. W. I. Pistorius, “Two-Dimensional Superresolution Radar Imaging Using the MUSIC Algorithm”, IEEE Transactions on Antennas and Propagatıon, vol. 42, no. 10, october 1994.

[30]. Victor C. Chen, “Time-Frequency Based Radar Image Formation,” Radar Division, Naval Research Laboratory, Washington DC, USA, 2004 IEEE.

[31]. Lokenath Debnath, “Recent developments in the wigner-ville distribution and time-frequency signal analysis,” PINSA, 68, A, No.1, January 2002, pp. 35-56.